



University of Kentucky
UKnowledge

University of Kentucky Doctoral Dissertations

Graduate School

2008

STUDIES OF LOW-LYING STATES IN ^{94}Zr EXCITED WITH THE INELASTIC NEUTRON SCATTERING REACTION

Esmat Elhami

University of Kentucky, esmate42@hotmail.com

[Right click to open a feedback form in a new tab to let us know how this document benefits you.](#)

Recommended Citation

Elhami, Esmat, "STUDIES OF LOW-LYING STATES IN ^{94}Zr EXCITED WITH THE INELASTIC NEUTRON SCATTERING REACTION" (2008). *University of Kentucky Doctoral Dissertations*. 624.
https://uknowledge.uky.edu/gradschool_diss/624

This Dissertation is brought to you for free and open access by the Graduate School at UKnowledge. It has been accepted for inclusion in University of Kentucky Doctoral Dissertations by an authorized administrator of UKnowledge. For more information, please contact UKnowledge@lsv.uky.edu.

ABSTRACT OF DISSERTATION

Esmat Elhami

The Graduate School
University of Kentucky

2008

STUDIES OF LOW-LYING STATES IN ^{94}Zr EXCITED WITH THE INELASTIC
NEUTRON SCATTERING REACTION

ABSTRACT OF DISSERTATION

A dissertation submitted in partial fulfillment of the
requirements for the degree of Doctor of Philosophy
in the College of Arts and Sciences
at the University of Kentucky

By

Esmat Elhami

Lexington, Kentucky

Director: Steven W. Yates, Professor of Chemistry and Physics & Astronomy

Lexington, Kentucky

2008

Copyright © Esmat Elhami 2008

ABSTRACT OF DISSERTATION

STUDIES OF LOW-LYING STATES IN ^{94}Zr EXCITED WITH THE INELASTIC NEUTRON SCATTERING REACTION

The aim of nuclear structure studies is to observe and describe the structures and associated symmetries in nuclei, which in turn help us in understanding the nature of nucleon-nucleon interactions in a nucleus as a many-body quantum system. The protons and neutrons as constituents of a nucleus and their interactions are responsible for nuclear properties. The evolution of nuclear structure as a function of valence nucleon number, i.e., the number of nucleons beyond a magic number, can be inferred from the experimental level scheme and transition rates. In particular, the studies of low-lying, low-spin excited states in stable nuclei provide valuable information on the interplay of valence neutrons and protons in nuclear structure. The decay scheme and knowledge of transition strengths in the low-lying states become a benchmark for testing theoretical model predictions and understanding the underlying microscopic foundations of nuclear structure. Along with the experimental techniques, theoretical models have been developed to explain and describe the observed nuclear properties, e.g., shell model, Fermi-gas model, optical and liquid-drop models, and several “collective” models.

$^{94}_{40}\text{Zr}_{50}$ nucleus with 2 protons and 4 neutrons above the shell closures of the $^{88}_{38}\text{Sr}_{50}$ core nucleus is considered as a nearly spherical nucleus. Such nuclei present a vibrational structure; surface vibration of the nucleus about a spherical shape. In addition to the symmetric excitations, in which proton and neutron oscillations are in phase, there are another class of excitations in which the wave function is not fully symmetric with respect to the exchange of protons and neutrons. These states are so called mixed-symmetry (MS) states. Such excitations have been observed in the $N = 52$ neighboring isotones. In this study, the low-lying structure of $^{94}_{40}\text{Zr}$ has been studied with the $(n, n'\gamma)$ reaction at the University of Kentucky and Triangle Universities Nuclear Laboratories (TUNL) facilities, to identify symmetric and MS excitations in this nucleus.

A decay scheme has been established based on excitation function and $\gamma\gamma$ coincidence measurements. Branching ratios, multipole mixing ratios, and spin assignments have been determined from angular distribution measurements at $E_n = 2.3, 2.8,$ and 3.5 MeV. Lifetimes of levels up to 3.4 MeV were measured by the Doppler-shift attenuation method (DSAM), and for many transitions reduced transition probabilities were determined. The experimental results were used for the identification of collective symmetric and mixed-symmetric (MS) multiphonon excitations. The 2_2^+ state at 1671.4 keV has been identified as the lowest MS state in ^{94}Zr ; $B(M1; 2_{ms}^+ \rightarrow 2_1^+) = 0.31(3) \mu_N^2$. This state has an anomalous

decay behavior, i.e., $B(E2; 2_{ms}^+ \rightarrow 0_1^+) = 7.8(7)$ W.u., which is unusually large compared to the $B(E2; 2_1^+ \rightarrow 0_1^+) = 4.9(3)$ W.u. More anomalies were identified in the states above the 2_{ms}^+ state. For example, the 4_2^+ state at 2330 keV decays strongly to the 2_1^+ state, $B(E2; 4_2^+ \rightarrow 2_1^+) = 20_{-2}^{+3}$ W.u., compared to the 4_1^+ state at 1469 keV, $B(E2; 4_1^+ \rightarrow 2_1^+) = 0.878(23)$ W.u. The experimental results revealed additional interesting and unusual properties of the low-lying states in ^{94}Zr . Shell model calculations were performed with the Oxbash code, using the $V_{low k}$ interaction. Also, the IBM-2 predictions in the vibrational limit were compared with the experimental results. The results from neither of these nuclear models were in good agreement with the observed transition strengths, e.g., the $B(E2; 2_{ms}^+ \rightarrow 0_1^+)$ value. These observations may indicate that the contributions of valence nucleons in the low-lying excited states of ^{94}Zr differ from what has been prescribed by the shell model and the IBM-2 model. The effects of the $Z = 40$ and $N = 56$ subshell closures should be also considered. In a simple interpretation, the excited states are classified in two distinct categories, i.e., those populating the 2_2^+ state and those decaying to the 2_1^+ state. This approach suggests that in ^{94}Zr the low-lying states may be related to two-configurations coexistence.

KEYWORDS: ^{94}Zr , Nuclear Structure, Inelastic Neutron Scattering, γ -ray Spectroscopy, Doppler-shift Attenuation Method (DSAM), Reduced Transition Probabilities.

Esmat Elhami

July 15, 2008

STUDIES OF LOW-LYING STATES IN ^{94}Zr EXCITED WITH THE INELASTIC
NEUTRON SCATTERING REACTION

By

Esmat Elhami

Steven W. Yates

Director of Dissertation

Joe W. Brill

Director of Graduate Studies

July 15, 2008

(Date)

DISSERTATION

Esmat Elhami

The Graduate School
University of Kentucky

2008

STUDIES OF LOW-LYING STATES IN ^{94}Zr EXCITED WITH THE INELASTIC
NEUTRON SCATTERING REACTION

DISSERTATION

A dissertation submitted in partial fulfillment of the
requirements for the degree of Doctor of Philosophy
in the College of Arts and Sciences
at the University of Kentucky

By

Esmat Elhami

Lexington, Kentucky

Director: Steven W. Yates, Professor of Chemistry and Physics & Astronomy

Lexington, Kentucky

2008

Copyright © Esmat Elhami 2008

Dedicated to:

My father, whose dedication to educate his children will continue to inspire us all,

My mother, for her extraordinary love, support and patience,

My sisters and brothers, for their encouragement and love,

My uncle, Mohammad, and aunt, Nancy, for their great support, love, and inspiration

ACKNOWLEDGMENTS

Claude Bernard, the Father of Physiology said, “Art is I; science is we”. This project and my studies would not have been completed if I would not have had the help from many people. I take this opportunity to thank these individuals.

I would like to express my sincere gratitude to my advisor, Prof. Steve Yates, for providing me the opportunity to work on such an interesting and exciting project. His inspiring and delicate guidance, advice, and expertise have been beyond the conduct of my dissertation project. For that, I thank you. Your unique approach in giving guidelines and precision have taught me how to be a researcher, a scientist, a mentor and overall a reliable, confident individual. It has been an honor to be your student.

I have enjoyed and benefited from the fruitful discussions with Dr. Marcus McEllistrem, my doctoral advisory committee member. His in-depth knowledge of almost every subject in physics, his patience with our endless questions, and other detailed information on experimental methodology have greatly contributed to this study, as well as my understanding as a physics student. Thank you.

I am thankful to Dr. Ali Meigooni for his valuable guidance and contributions, as my committee member and a mentor. I am also grateful to him, his wife, Mrs. Sharifeh Azam Dini, and their sons for their friendship, encouragement and support during my studies in Lexington.

I would like to thank Dr. Mike Cavagnero, whose guidance and advice from the early days in my studies have helped me to work harder, not to lose hope, and reach out for my goals “one step at the time” as he once told me. Also, I would like to thank Dr. Wolfgang Korsch, as a member of my PhD committee for his enthusiasm, support and corrections of this dissertation.

I am grateful to the Department of Physics and Astronomy for providing funding through

teaching/research assistantships. The great help of the current and previous administration and office staff in ensuring my enrollment are greatly appreciated. I would like to acknowledge Gene Baber, the University of Kentucky accelerator engineer, whose great help and expertise made the performance of the experiments possible.

It is my honor to acknowledge and thank my colleagues at the University of Kentucky who took part in the experiments by taking odd-hour shifts and for the fruitful discussions and guidance. I thank Dr. Nico Orce for his encouragement and valuable contributions throughout this project on shell model calculations (chapter 4), and his great help in the first publication of our results are appreciated. I have benefited from Dr. Marcus Scheck's great ideas, his insight and good understanding of nuclear structure physics. I would like to thank Dr. Sharmistha Mukhopadhyay and Dr. Sadia Choudry for their friendship. I enjoyed and learned a lot from our interesting and stimulating discussions on physics, our projects, and sometimes about non-physics subjects. Sharing their experiences and thoughts with me has helped me undoubtedly. The hard task of correcting the first draft of this dissertation has been done by Erin Peters. Her help, friendship, and sharing thoughts are greatly appreciated. Some of the newer computer codes for data analysis were written by Ben Crider, whose help is greatly appreciated.

I would also like to thank our collaborators at the Triangle Universities Nuclear Laboratories (TUNL) at Duke University - C. Angell, M. Boswell, F. Fallin, C. Howell, A. Hutcheson, H.J. Karwowski, J. H. Kelly, Y. Parpottas, A.P. Tonchev, and W. Tornow - for conducting the $\gamma\gamma$ coincidence measurements. In particular, I would like to thank Dr. Anton Tonchev and Dr. John Kelly for providing the `SpecTcl` software package and the original tcl scripts for data analysis. The conversion of the gamma-gamma coincidence matrices to Tv format were performed with modifications applied to the `SpecTcl` code. I am grateful to Dr. Dirk Weisshaar, from Michigan State University/NSCL, for his great help

in providing some of these computer codes.

I would like to thank my friends, Dr. Xuinu Lin, Vinobalan Durairaj, and Shalinee Chikara for their great support and help when I was in the Noval Material research group. Many other friends and classmates are acknowledged for their help, especially, Vijayalakshmi Varadarajan (Viji) for her words of encouragement, Gretchen Phelps for her liveliness and sense of humor, which would cheer me up most of the time, and Dr. Dekka for his help with the formatting of this dissertation. The support of many more friends and families in Lexington and Indiana are greatly appreciated.

I would also like to acknowledge my dear friends from Iran, Mrs. Fateme Afshari, Mrs. Zohre Afrakhte and Dr. Alieh Haghdad. We went to the same elementary and high schools and grew up together. Their friendship, support, and encouragement which have been with me always and during my studies in the States, are greatly appreciated. Thank you and I wish you the best always.

My special thanks goes to my mother, whose unconditional love and care has been always in support of my ambitions. In particular, I would like to acknowledge her efforts in making a trip to the United States, by herself for the first time without knowing the language and customs. Her strength, courage, and faith do not leave any excuse for me to do less. You are my Hero.

Even though, my father is no longer among us, his spirit and love for learning, exploring, and education have always encouraged me and have kept me focused. I miss him terribly. I wish I could have celebrated my accomplishments with him.

I am grateful to my sisters and brothers and their families, including my nieces and nephews, and my grandmother (Jade) for their unconditional love and support. My sisters, Maryam, Zahra, and Fateme, and my niece, Shima, have inspired me into becoming an independent woman. Their love and support for my mother, especially Maryam has made

my being away from home possible. My brother, Ali, with his genuine attitude in learning and his curiosity in science, inspired me in my early school days, and my brother, Mohammad, whose advice and encouragement about coming to the States to study, will be always appreciated. Thank you all and I am honored to be your little sister.

I would like to express my love and gratitude to my cousins: Dr. Heidi Behforouz, whose strength and caring heart had showed me the true nature of a genuine soul, Kayvon and his fiancé, Chelsea, for their kindness and interest in my progress and accomplishments, and Dr. Michael (Afshin) and Maryjane Behforouz, whose love, support, and encouragement have filled me with life and joy. Their sweet girls, Kayla and Stella, whose laughter and sweetness in our countless chasing, playing, and art-crafting, have created valuable memories; I love you! I am truly grateful to get to know Mrs. Kathleen Cook, my cousins' grandmother, whose love, encouragement, and valuable teachings have enriched my life tremendously.

At last, not the least, I am truly in debt and thankful to my uncle and aunt, Drs. Mohammad and Nancy Behforouz, whose great support and enthusiasm made it possible to pursue and continue my graduate studies in the United States. Because of their extraordinary passion for education and care for people, many Iranian young men and women have come to the States and have excelled in their lives. It has been an honor for me to be the first member of my family to come to the States, and also live with them for the first two years. They have taught me more than I could put in words. Neither I, nor my family, could thank them enough for their caring hearts and unconditional generosity and support. I hope I can pay my debt by helping others to make their dreams come true.

Thank you all for your support and teaching me to believe in the power of will!

TABLE OF CONTENTS

Acknowledgments	iii
List of Tables	x
List of Figures	xi
List of Files	xiii
CHAPTER 1: INTRODUCTION	1
1.1 Nuclear Structure and Theoretical Models	1
1.2 Shell Model	1
1.3 Collective Models	3
1.3.1 Geometric Model of Bohr-Mottelson	5
1.3.2 The Interacting Boson Models	6
1.4 ^{94}Zr and Collectivity	10
CHAPTER 2: EXPERIMENTAL PROCEDURES	13
2.1 Inelastic Neutron Scattering, the $(n,n'\gamma)$ Reaction	13
2.1.1 Neutron Production and Gamma-Ray Detection	14
2.1.2 The Experimental Methods	14
2.2 The Experimental Setup at the University of Kentucky	15
2.2.1 Neutron Detection for Normalization Purposes	18
2.2.2 Data Acquisition and Electronics Setup	19
2.2.3 Excitation Function Measurements	20
2.2.4 Angular Distribution Measurements	23
2.3 The Experimental Setup at TUNL	24
2.3.1 γ - γ Coincidence Measurements	24
2.3.2 Electronics and Data Acquisition System	26
CHAPTER 3: DATA ANALYSIS	30
3.1 Spectrum Calibrations	30
3.2 Spectrum Fitting Programs	30
3.3 Excitation Functions	32
3.4 Angular Distributions	33
3.5 Lifetime Measurements	36
3.6 Reduced Transition Probabilities	39
3.7 $\gamma\gamma$ Coincidences	41
3.7.1 Building a Matrix, using a SpecTcl .tcl script	43
3.7.2 Creating Projection and Gated Spectra	46

3.8	Coincidence measurements at the UK facility, A Comparison	46
3.8.1	Coincidence Time Requirements	48
3.8.2	The UK Coincidence Data Analysis	49
3.8.3	The Comparison Results	50
CHAPTER 4: RESULTS AND DISCUSSION		54
4.1	Experimental Results	54
4.1.1	Level Scheme, $E_x < 3.0$ MeV	54
4.1.2	Level Scheme, $E_x > 3.0$ MeV	60
4.2	Discussion	72
4.2.1	Quadrupole-phonon Excitations	73
4.2.2	$2_1^+ \otimes 3_1^-$ Quintuplet	73
4.2.3	Anomalous Decay Behavior of Low-lying States in ^{94}Zr	74
4.2.4	A Simple Classification of the Excited States in ^{94}Zr	74
4.3	A Simple Interpretation	75
4.3.1	Valence Nucleons	76
4.3.2	Comparison to ^{94}Mo	77
4.3.3	The 2_1^+ and 2_2^+ States; Two-Configuration Coexistence	78
4.4	Model Calculations	79
4.4.1	Shell Model Calculations	79
4.4.2	IBM-2 Results	84
CHAPTER 5: CONCLUSION AND FUTURE DIRECTIONS		86
Appendices		88
APPENDIX A: MAGNETIC DIPOLE MOMENT AND $M1$ TRANSITIONS		88
A.1	$M1$ Operator	88
APPENDIX B: BACKGROUND AND ZR GAMMA RAYS		90
APPENDIX C: EFFECTIVE CHARGES IN THE SHELL MODEL		96
APPENDIX D: GAMBIT CORRECTIONS		97
D.1	Neutron Scattering	97
D.2	Photoabsorption	98
APPENDIX E: SPIN ASSIGNMENTS FROM EXCITATION FUNCTIONS		100
E.1	Gambit and Photoabsorption Corrections	100
E.2	Inelastic Neutron Scattering Corrections	103
E.3	Theoretical Cross Sections	103

E.4 Spin Assignments	104
APPENDIX F: DETAILS OF TUNL γ - γ COINCIDENCE DATA ANALYSIS	107
F.1 SpecTcl Software Modifications	107
F.2 SpecTcl	108
F.3 Coincidence Data Analysis Using Tv	109
F.4 Spectra Construction .tcl Script, spectcl_uk.tcl	109
F.5 Hardware Setup .tcl Script, hardware94Zr.tcl	125
APPENDIX G: UK COINCIDENCE DATA ANALYSIS	129
G.1 Creating Time and Energy Spectra	129
G.2 Building a Matrix	130
G.3 Creating X and Y Projections Using the Code slice	131
G.4 Creating Background Spectra	132
G.5 Creating a Matrix in a Compressed Format for Analysis in xmesc	133
G.6 Creating Gated Spectra in xmesc	134
Bibliography	135
VITA	140

LIST OF TABLES

1.1	The characteristics of the one-phonon MS and symmetric states in the neighboring N= 52 and 54 isotones	11
2.1	Contaminants of other Zr isotopes in the scattering sample of ^{94}Zr	13
2.2	The geometric characteristics of the experimental setups for measurements at the UK facility	23
2.3	The list of the angles measured in the angular distribution measurements	23
2.4	The composition of the Havar foil	26
3.1	Multipolarity of the lowest order in transitions	40
4.1	Experimental information on the ^{94}Zr level scheme	64
4.2	Unplaced γ rays in ^{94}Zr	68
4.3	$B(M1)$ and $B(E2)$ values calculated for γ -ray transitions in ^{94}Zr	68
4.4	$B(E1)$ values calculated for γ -ray transitions in ^{94}Zr	72
4.5	The single-particle energies (s.p.e) used for ^{94}Zr shell model calculations	80
4.6	Experimental data and shell model calculation results	83
B.1	All the observed γ rays in the excitation function spectra	90
C.1	Shell model calculation results for some of the $B(E2)$ values for different effective charges	96

LIST OF FIGURES

1.1	Nuclear landscape	2
1.2	A schematic diagram of collectivity in the nuclear landscape	2
1.3	Nuclear shell structure	4
1.4	Decay schemes in the harmonic vibrational limit and experimental examples	6
1.5	The theoretical and the experimental decay scheme of $^{162}_{66}\text{Dy}$	7
1.6	Symmetry triangle of the IBM	9
1.7	Decay scheme for MS states in a nearly spherical nucleus	10
1.8	Evolution of the nuclear structure of the Zr isotopes	11
2.1	Schematic of the experimental setup for singles-mode measurements at the University of Kentucky facility	16
2.2	Picture of the $(n, n'\gamma)$ singles measurement setup	17
2.3	Schematic of a TOF spectrum	17
2.4	Forward monitor spectrum obtained in a $^{94}\text{Zr}(n, n'\gamma)$ angular distribution measurement	18
2.5	γ -ray spectrum obtained in $^{94}\text{Zr}(n, n'\gamma)$ excitation function measurement . .	19
2.6	The UK singles-mode measurement electronics	20
2.7	The long counter and forward monitor electronics	21
2.8	Energy sections of a singles-mode γ -ray spectrum of ^{94}Zr	22
2.9	Example of two cascades in a nucleus	24
2.10	A schematic of a clover detector used in coincidence measurements	25
2.11	Schematic of the $\gamma\gamma$ coincidence setup at the TUNL facility	27
2.12	Photograph of the experimental setup used in ^{94}Zr coincidence measurements at the TUNL facility	27
2.13	Schematic of the electronics setup for coincidence measurements at TUNL .	28
3.1	The nonlinearity curve for ^{94}Zr excitation function data	31
3.2	Efficiency curve for the HPGe detector used in $^{94}\text{Zr}(n, n'\gamma)$ excitation function measurements at UK	31
3.3	Examples of prompt γ -ray spectra from the ^{94}Zr excitation function measurements at different incident E_n	34
3.4	Examples of angular distribution plots	35
3.5	Example of angular distribution output plots	37
3.6	Example of Doppler shifts in the γ -ray spectra	38
3.7	Plot of E_γ vs. $\cos \theta$ for the 752-keV γ -ray transition and the calculated theoretical $F(\tau)$ vs. τ	39
3.8	Schematic of coincidence analysis	42
3.9	The total projection of the matrix ALL in the X direction	47

3.10	Spectrum gated on the 918-keV γ ray in ^{94}Zr	47
3.11	KEGS, the experimental setup for coincidence measurements at UK	48
3.12	Example of a time spectrum from ^{106}Pd coincidence data at UK	49
3.13	Example of a time spectrum from ^{94}Zr coincidence data at TUNL	50
3.14	Total projection of the coincidence data for ^{106}Pd	51
3.15	Coincidence spectrum gated on the 512-keV γ ray in ^{106}Pd	51
4.1	Angular distribution for 752-keV γ -ray transition	56
4.2	Transitions from the 2^+ states	75
4.3	Transitions from the 4^+ and 3^+ states	76
4.4	Valence proton and neutron orbitals in ^{94}Zr	77
4.5	Demonstration of the weak coupling scheme for ^{94}Zr	78
4.6	Valence proton orbitals in $N = 54$ isotones, $^{93}_{39}\text{Y}$, $^{94}_{40}\text{Zr}$, and $^{95}_{41}\text{Nb}$	80
4.7	The experimental and shell model calculation results	81
4.8	The least-squares fit for the plot of $[NB(E2; 2_1^+ \rightarrow 0_1^+)/N2_{\pi}^{1/2}]$ against N_{ν}/N_{π}	84
B.1	^{94}Zr Level Scheme	95
E.1	Photoabsorption plot for ^{94}Zr	103
E.2	Excitation function CINDY plot	106
F.1	SpecTcl environment	110

LIST OF FILES

Name : dissEsmatElhami

Type : .pdf

Size : 4.71 MB

CHAPTER 1: INTRODUCTION

1.1 Nuclear Structure and Theoretical Models

The aim of nuclear structure studies is to observe and describe the structures and associated symmetries in nuclei, which in turn help us in understanding the nature of nucleon-nucleon interactions in a nucleus as a many-body quantum system. The protons and neutrons as constituents of a nucleus and their interactions are responsible for nuclear properties. The strong nuclear force between the nucleons, which overcomes the electromagnetic force between the protons, is responsible for the formation of a stable nucleus. Consequently, there is a limit on the numbers of protons (Z) and neutrons (N) which form heavy stable nuclei around $N \approx 1.6 Z$, the line of stability, in the chart of nuclei, as shown in Figure 1.1. As an example of nuclear properties, the separation energy of a nucleon, S_ρ ($\rho =$ neutron or proton), suddenly changes at certain Z or N , namely, 2, 8, 20, 28, 50, 82 and 126 (for neutrons only), which are known as magic numbers. This phenomenon is evidence of a shell structure in nuclei [1].

The evolution of nuclear structure as a function of valence nucleon number, i.e., the number of nucleons beyond a magic number, can be inferred from the experimental level scheme and transition rates. A variety of experimental techniques have been employed to study the systematic evolution in nuclear structure as a function of the number of nucleons; e.g., studies of isotopes (nuclei with the same Z) or isotones (nuclei with the same N). The nuclei with nucleon numbers close to a major shell can be described as spherical and also often show collective vibrational structure, whereas by adding several more nucleons, the nuclear structure evolves to the rotational limit. These regions of collectivity in the nuclear landscape are shown in Figure 1.2 and will be discussed briefly in Section 1.3.1.

In particular, the studies of low-lying, low-spin excited states in stable nuclei provide valuable information on the interplay of valence neutrons and protons in nuclear structure. The decay scheme and knowledge of transition strengths in the low-lying states become a benchmark for testing theoretical model predictions and understanding the underlying microscopic foundations of nuclear structure. Along with the experimental techniques, theoretical models have been developed to explain and describe the observed nuclear properties, e.g., shell model, Fermi-gas model, optical and liquid-drop models [2], and several “collective” models. Some of these models are briefly discussed.

1.2 Shell Model

The phenomenon of shell structure in nuclei was interpreted in analogy to the model of the atom by the microscopic shell model [1, 2, 4, 5], which was developed in 1949 by Wigner, Goeppert-Mayer and Jensen. Analogous to the electrons moving in the central

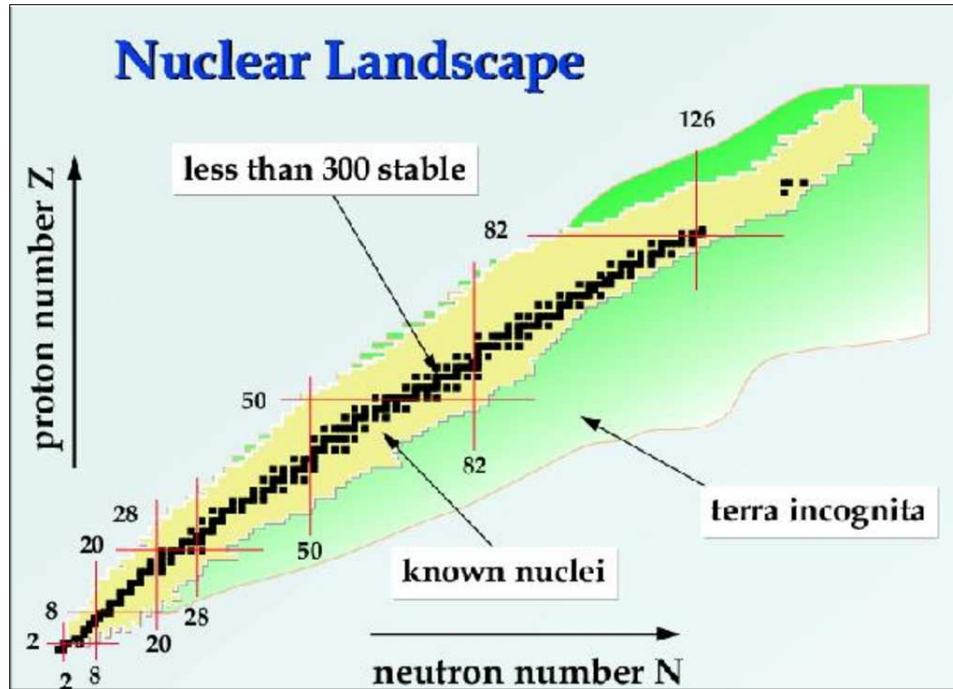


Figure 1.1: Nuclear landscape, depicting the line of stability, $Z=N$, and regions yet to be explored, terra incognita. The magic numbers are marked as well, taken from Ref. [3].

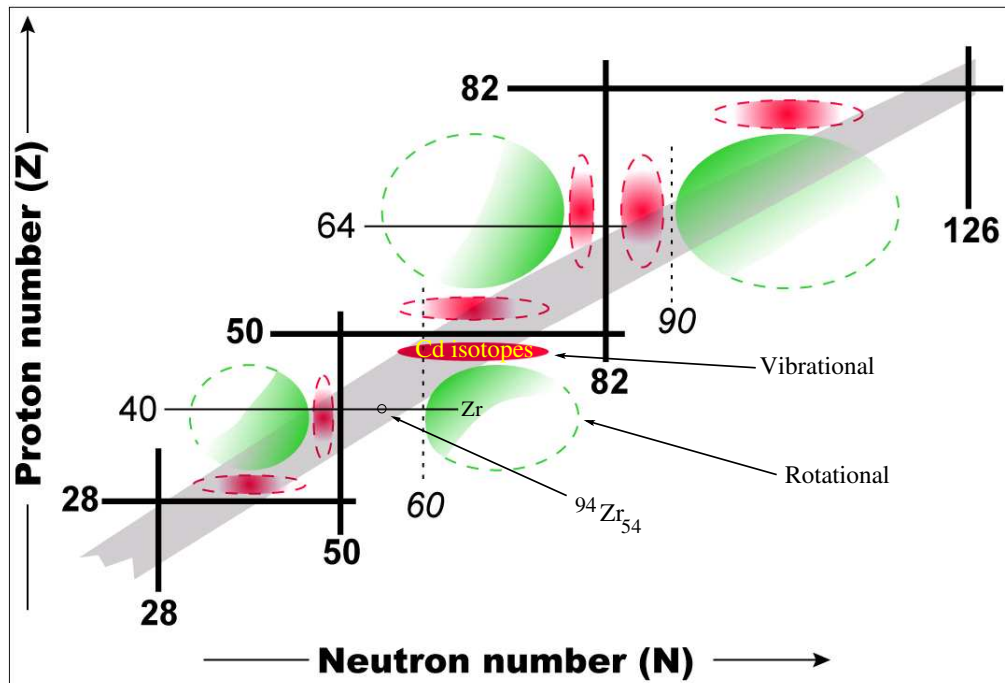


Figure 1.2: A schematic diagram of collectivity in the nuclear landscape. The vibrational and rotational regions are shown. Note the Cd isotopes ($Z=48$) as exemplary vibrational nuclei.

potential of the nucleus in quantized orbits, in the shell model of a nucleus quantized orbitals are assumed to be occupied by the nucleons, as shown in Figure 1.3. In the shell model Hamiltonian, potentials such as the harmonic oscillator or Woods-Saxon (a modified square-well potential) could only explain the magic numbers of 2, 8 and 20. The Woods-Saxon potential is given by the expression

$$V(r) = \frac{-V_0}{1 + \exp^{(r-R)/a}} \quad (1.1)$$

where $R \simeq 1.25A^{1/3}$ fm denotes the nuclear radius and $a \simeq 0.65$ fm is the nuclear surface thickness. However, an additional consideration of a spin-orbit interaction, $\mathbf{l} \cdot \mathbf{s}$ (analogous to the atomic model), was successful in predicting the rest of the magic numbers (28, 50, 82, 126) and the energy levels of each corresponding (nl_j) level.

When the number of valence nucleons in a nucleus is far beyond that of a closed shell, the p-n interaction strength leads to deviations from the shell model spherical potential. Therefore, the nuclear shape is no longer spherical, and the nucleus develops a permanent deformed shape. The deformation can be detected in observables, e.g., the electrostatic quadrupole moment, Q . A prolate shape (like a rugby ball) has $Q > 0$, while an oblate (like a frisbee) has $Q < 0$. This deformed shell model, or Nilsson model, incorporates a deformed harmonic oscillator potential and is used to describe the single-particle motion in the field of the deformed shape. The Hamiltonian for a single particle [6] in a nucleus with symmetry axis z can be expressed by:

$$H = T + V = \frac{\mathbf{p}^2}{2m} + \frac{1}{2}m[\omega_x^2(x^2 + y^2) + \omega_z^2z^2] + C\mathbf{l} \cdot \mathbf{s} + D\mathbf{l}^2 \quad (1.2)$$

where ω_i ($i = x, y, z$) are the one-dimensional oscillator frequencies in the respective directions. Spin-orbit, $\mathbf{l} \cdot \mathbf{s}$, and angular momentum, \mathbf{l}^2 , terms are also included. The nuclear deformation leads to deviations of the nucleon orbital energies from those in a spherical nucleus.

1.3 Collective Models

The shell model and its extensions have had success in explaining many nuclear properties, such as magnetic moments and ground-state spins in odd-mass nuclei, but it failed to explain the properties of the lowest-lying states in even- Z , even- N nuclei, which are usually at excitation energies lower than 2 MeV. This, and an increase in transition rates, cannot be explained by pure shell model single-particle states, because the pairing force is neglected in its Hamiltonian; the energy required to break a pair of nucleons is ~ 2 MeV. Most shell model calculations consider only the valence nucleons as single particles which are contributing to nuclear properties and structure, but several or many nucleons need to be involved to create a collective structure, as is often observed for the 2_1^+ excited state

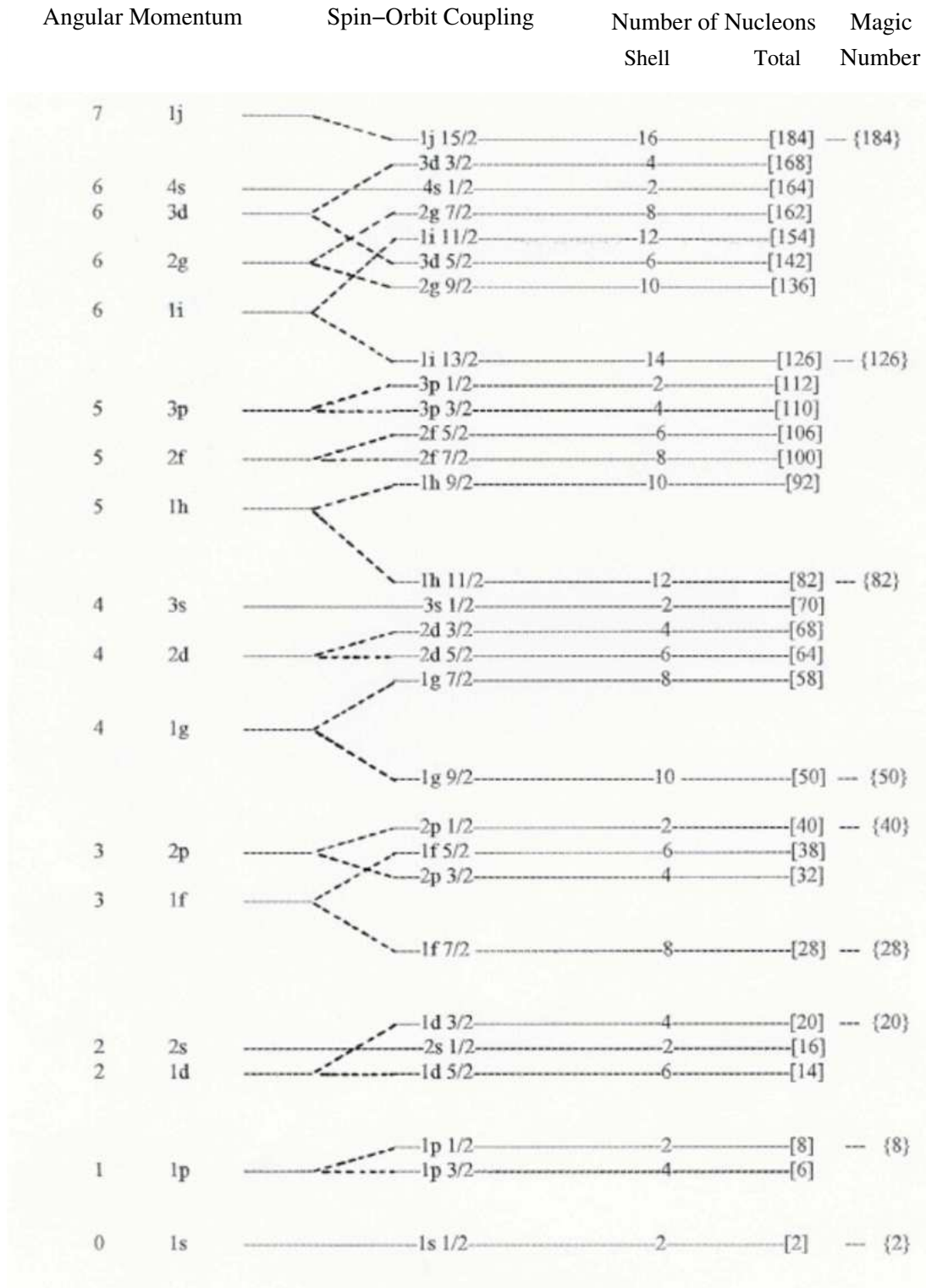


Figure 1.3: Nuclear shell structure, taken from Ref. [1]. The effect of $l \cdot s$ in reproducing the magic numbers is evident.

in even-even nuclei. Coherent excitations of the nucleons in a nucleus are responsible for collective excitations, such as vibrations and rotations. Such excitations are described by collective models, which are briefly described in this section.

1.3.1 Geometric Model of Bohr-Mottelson

The geometric model, developed by Rainwater and more thoroughly by Bohr and Mottelson in the early 1950s [7], provided the first description of collective excitations in spherical and deformed nuclei. The low-lying collective excitations in spherical nuclei are of vibrational character. Rotational excitations are impossible for a strictly spherical symmetry. Therefore, the geometric collective model simplifies to its vibrational limit. The resulting vibrations correspond to dynamic oscillations of the nuclear surface about a spherical shape and can be described as:

$$R = R_0 \left[1 + \sum_{\lambda} \sum_{\mu} \alpha_{\lambda\mu} Y_{\lambda\mu}(\theta, \phi) \right] \quad (1.3)$$

where $Y_{\lambda\mu}$ are the spherical harmonics of order λ , with $\alpha_{\lambda\mu}$ amplitude, R_0 is the nucleus radius. The quantized vibrational excitations are called phonons and coupling of phonons gives rise to multiphonon excitations, as shown in Figure 1.4. A quadrupole vibration ($\lambda = 2$) is the lowest order of distortion in a spherical nucleus. Octupole, $\lambda = 3$, and hexadecapole, $\lambda = 4$, are higher orders of vibrational excitations. The excitation energy of the multiphonons can be described as $E = N_{ph} \hbar\omega$, where N_{ph} refers to the phonon number.

For example, the Hamiltonian for the quadrupole distortion can be expressed by [6]:

$$H = T + V = \frac{1}{2} B \sum_{\mu} \left| \frac{d\alpha_{2\mu}}{dt} \right|^2 + \frac{1}{2} C \sum_{\mu} |\alpha_{2\mu}|^2 \quad (1.4)$$

where B and C , in analogy to an oscillator, correspond to the mass and restoring force parameters, respectively. By differentiating H , with respect to time, (H is a constant of motion and $\frac{dH}{dt} = 0$) we obtain:

$$B \frac{d^2 \alpha_{2\mu}}{dt^2} + C \alpha_{2\mu} = 0 \quad (1.5)$$

which gives a solution for the strength of oscillation, $\alpha_{2\mu}$, with a frequency $\omega = \sqrt{\frac{C}{B}}$, and a vibrational energy of $\hbar\omega$.

In the quadrupole harmonic vibrational limit, for example, in an even-even nucleus, the first excited state, 2_1^+ , is called the one-phonon quadrupole (**Q**) state, at an excitation energy of $E = \hbar\omega$ ($N_{ph} = 1$). Thus, the two-phonon triplet, $0^+, 2^+, 4^+$ states, which are formed from [**Q** \otimes **Q**] coupling will be degenerate at an energy twice that of $E_{2_1^+}$. In reality, these states are not degenerate and exhibit anharmonicities, as shown in Fig 1.4. The transition strengths also have specific characteristics. The electric quadrupole transition,

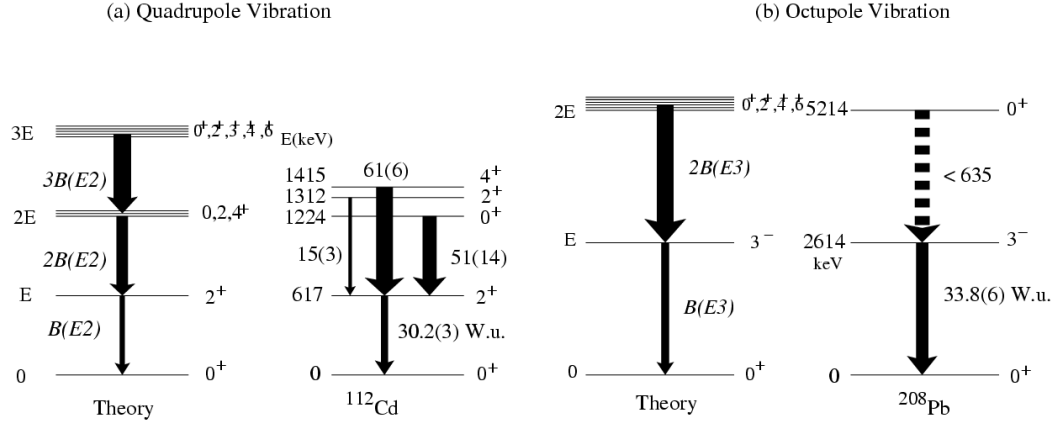


Figure 1.4: Decay schemes in the harmonic vibrational limits and experimental examples: (a) $^{112}_{48}\text{Cd}$ for quadrupole, (b) $^{208}_{82}\text{Pb}$ for octupole excitations. The width of the $E2$ and $E3$ arrows are proportional to their strengths. Also, the degeneracies in the harmonic limit are shown. The experimental data are from Ref. [8].

$E2$, is allowed only with a selection rule of $\Delta N_{ph} = 1$, and its magnitude, $B(E2)$, is proportional to the phonon-number, i.e., $B(E2; N_{ph} = 2 \rightarrow N_{ph} = 1) = 2B(E2; N_{ph} = 1 \rightarrow N_{ph} = 0 \text{ (g.s)})$. Quadrupole vibrations have been observed in many nuclei; $^{112}_{48}\text{Cd}$ is one of the textbook examples presenting such excitations. There are fewer nuclei, such as $^{208}_{82}\text{Pb}$, presenting the octupole excitations, with a 3^- state as the first excited state. The strong stretched ground-state octupole transitions, $(E3; 3^-_1 \rightarrow 0^+_1)$, in these nuclei are usually indicative of such collective behavior.

Also, as an experimental signature of collective excitations, the ratio of $\frac{E(4^+_1)}{E(2^+_1)}$ in even-even nuclei provides some information about the nuclear structure. This ratio is 2 for a vibrational nucleus (spherical shape), 2.5 for a gamma-soft rotor (an axially asymmetric deformed nucleus), and 3.33 for an axially symmetric deformed nucleus [7].

In a rotational nucleus, the energy of the excited states, as a function of spin of the state, J , and the moment of inertia, I , is expressed by $E \approx \hbar^2 J(J+1)/2I$. The decay scheme of such a nucleus is shown in Figure 1.5. In this case, the $E2$ strengths do not follow a description as simple as in the vibrational nuclei, but firm predictions exist.

1.3.2 The Interacting Boson Models

1. IBM-1

A different approach to describe the low-lying collective excited states in nuclei is the algebraic approach introduced by Arima and Iachello [9,10] in 1974. This model, called the interacting boson model (IBM), is based on group theoretical methods. The Hamiltonian incorporates dynamical symmetries to describe the nuclear structure, such as the level sequences and electromagnetic transition rates. In the simplest approach, the sd -IBM-1,

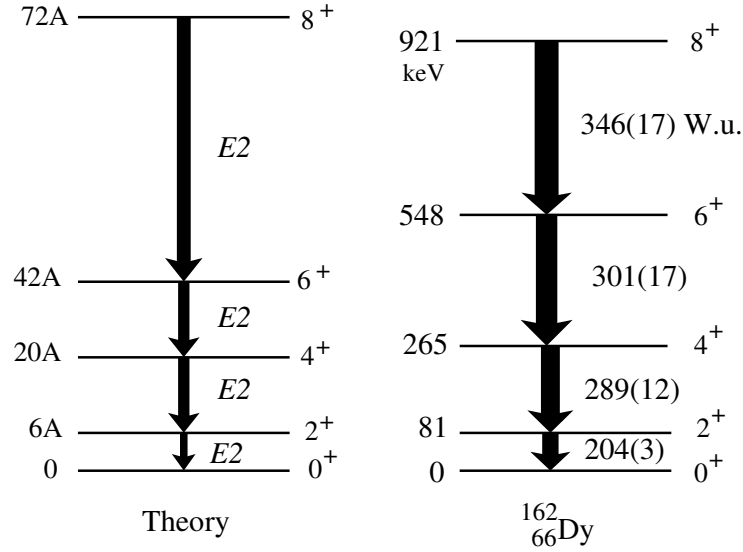


Figure 1.5: The theoretical and the experimental decay schemes of $^{162}_{66}\text{Dy}$, an example of a rotational nucleus. The parameter A is defined as $\frac{\hbar^2}{2I}$, where I is the moment of inertia. A is 13.5 keV for $^{162}_{66}\text{Dy}$. The experimental data are from Ref. [8].

the Hamiltonian is developed for a system of N bosons. A boson is a pair of neutrons or protons coupled to $J = 0$ (s -bosons) or $J = 2$ (d -bosons). The s - and d -bosons form the generators of $U(6)$ symmetry (6 degrees of freedom for s and d magnetic substates). A general Hamiltonian is ascribed to have symmetries of the $U(6)$ group and is given by:

$$H = \sum_{i=1}^N \epsilon_i + \sum_{i<j}^N v_{ij} \quad (1.6)$$

where ϵ_i is the energy of a single boson and v_{ij} is the interaction potential between pairs of bosons. In the second quantization the boson creation operators are s^\dagger and d_μ^\dagger , and the boson annihilation operators are represented by s and $\tilde{d}_\mu = (-1)^\mu d_{-\mu}$, where the magnetic substates for d -boson operators are $\mu = 0, \pm 1, \pm 2$; s -bosons have only one magnetic substate. The total Hamiltonian, in multipole form, is described by Eqn. 1.7 [11].

$$\begin{aligned}
H &= \varepsilon'' \mathbf{n}_d + a_0 \mathbf{P}^\dagger \cdot \mathbf{P} + a_1 \mathbf{J} \cdot \mathbf{J} + a_2 \mathbf{Q}^X \cdot \mathbf{Q}^X + a_3 \mathbf{T}_3 \cdot \mathbf{T}_3 + a_4 \mathbf{T}_4 \cdot \mathbf{T}_4 \quad (1.7) \\
\mathbf{n}_d &= (\mathbf{d}^\dagger \tilde{\mathbf{d}}), \\
\mathbf{P}^\dagger &= \frac{1}{2} (\mathbf{d}^\dagger \cdot \mathbf{d}^\dagger - \mathbf{s}^\dagger \cdot \mathbf{s}^\dagger) \\
\mathbf{P} &= (\mathbf{P}^\dagger)^\dagger = \frac{1}{2} (\mathbf{d} \cdot \mathbf{d} - b f s \cdot s) \\
\mathbf{J} &= \sqrt{10} [\mathbf{d}^\dagger \tilde{\mathbf{d}}]^{(1)} \\
\mathbf{Q}^X &= [\mathbf{d}^\dagger \mathbf{s} + \mathbf{s}^\dagger \tilde{\mathbf{d}}]^{(2)} + \chi [\mathbf{d}^\dagger \tilde{\mathbf{d}}]^{(2)}, \\
\mathbf{T}_3 &= [\mathbf{d}^\dagger \tilde{\mathbf{d}}]^{(3)},
\end{aligned}$$

$$\mathbf{T}_4 = [\mathbf{d}^\dagger \tilde{\mathbf{d}}]^{(4)} \quad (1.8)$$

\mathbf{n}_d is the d -boson number operator. \mathbf{P} is the pairing operator. \mathbf{J} represents the d -bosons coupled to total angular momentum $J = 1$. \mathbf{Q} is the quadrupole operator, and also represents the $E2$ transition operator. \mathbf{T}_J are the operators of higher orders, when the d -bosons couple to angular momentum, e.g., J of 3 or 4.

By considering certain operators in the Hamiltonian as given in Eqn. 1.7 with their corresponding quantum numbers, the $U(6)$ symmetry results in three different subgroups which result in $O(3)$, as shown in Eqn. 1.9. The $O(3)$ is the rotation group, which provides for rotational invariance, necessary for any physical system [6, 11].

$$\text{I. } U(6) \supset U(5) \supset O(5) \supset O(3) \quad (1.9)$$

$$\text{II. } U(6) \supset SU(3) \supset O(3) \quad (1.10)$$

$$\text{III. } U(6) \supset O(6) \supset O(5) \supset O(3) \quad (1.11)$$

For example, vibrational nuclei are described by $U(5)$ symmetry and deformed rotors by $SU(3)$. One of the many successes of the IBM-1 model in describing the collective properties of nuclei is demonstrated in vibrational nuclei. Consideration of the electric quadrupole operators in the Hamiltonian of the $U(5)$ symmetry leads to derivations of isospin symmetric multiphonon excitations in the level scheme, as shown in ^{112}Cd level scheme in Figure 1.4. There are some nuclei described by $O(6)$ symmetry, called gamma-soft rotors, where in the Hamiltonian a nonaxially symmetric vibrational degree of freedom, gamma, can have variable values, resulting in different vibrational nuclear structures.

In the symmetry triangle developed by Casten [6], these symmetries reside on the vertices of the triangle, $U(5)$ and $SU(3)$ on the base and $O(6)$ on the third vertex, as shown in Figure 1.6. Within this triangle, a position for a nucleus can be assigned based on its structural symmetries. The nuclear structure, mainly the low-lying excited states, can be expressed through the choice of appropriate operators in the Hamiltonian. Based on this description, many nuclei fall in the transitional regions between the basic symmetries. For example ^{152}Sm is in the transitional region between $U(5)$ and $SU(3)$ symmetries, but closer to $SU(3)$ symmetry [12].

2. IBM-2 and Mixed-Symmetry (MS) States

In the IBM-2, which distinguishes between proton (π) and neutron (ν) degrees of freedom, a new class of states was predicted [13]. The wavefunctions of these states are not fully symmetric with respect to the exchange of protons and neutrons and, therefore, these states are called mixed-symmetry (MS) states. The first experimental observation of such states was that of a 1^+ state, the so-called scissors mode, in deformed nuclei, e.g., ^{156}Gd [14] at an energy of approximately 3 MeV. The name refers to the geometrical picture of the neutron body oscillating against the proton body like cutting scissors. For a nearly spherical nucleus

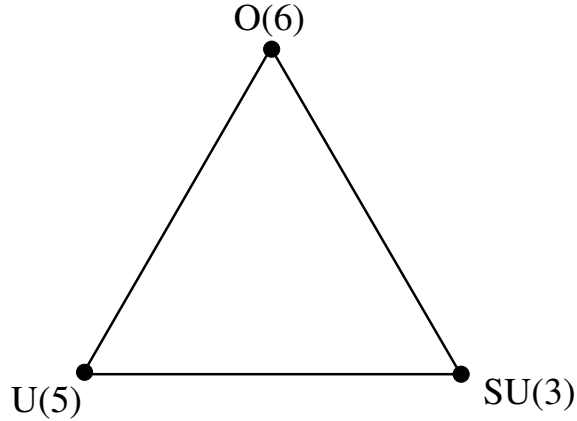


Figure 1.6: Symmetry triangle of the IBM, $U(5)$ represents the vibrational limit, $SU(3)$ for rotational and $O(6)$ for gamma-soft nuclei [6].

near a closed shell, a *vibrator*, it was predicted that the lowest-lying MS state has $J^\pi = 2^+$, at 2-MeV excitation energy, with $B(E2 \uparrow) \approx 3$ s.p.u. [13] and a strong magnetic dipole, $M1$, transition to the corresponding symmetric state with a $B(M1) \approx 1\mu_N^2$. Experimental evidence for these states is summarized and discussed in a recent review paper by Pietralla *et al.* [15], and the signatures of these states are illustrated in Figure 1.7. The $M1$ transition operator is described in Appendix A.

In a nearly spherical nucleus, the MS multiphonon excitations can arise from phonon couplings. These excitations, built on the one-phonon MS state, can be described approximately within the Q-phonon scheme [16, 17]. Separate quadrupole operators, $\mathbf{Q}_{\pi,\nu}$, are assigned to the proton and neutron pairs outside the nuclear core. The symmetric, \mathbf{Q}_s^\dagger , and non-fully symmetric, \mathbf{Q}_m^\dagger , creation operator can be expressed by:

$$\mathbf{Q}_s^\dagger = \mathbf{Q}_\pi^\dagger + \mathbf{Q}_\nu^\dagger \quad (1.12)$$

$$\mathbf{Q}_m^\dagger = a \mathbf{Q}_\pi^\dagger - b \mathbf{Q}_\nu^\dagger \quad (1.13)$$

where the $a = \frac{N}{2N_\pi}$ and $b = \frac{N}{2N_\nu}$ and $N = N_\pi + N_\nu$ is the total number of valence bosons. The operation of \mathbf{Q}_s^\dagger on the ground state creates the first symmetric excited state, i.e., 2_1^+ , whereas the operation of the \mathbf{Q}_m^\dagger operator on the ground state, leads to the creation of the first mixed-symmetric excited state, 2_{ms}^+ . The coupling of \mathbf{Q}_s^\dagger and \mathbf{Q}_m^\dagger creates the multiphonon states, e.g., $\mathbf{Q}_s^\dagger \mathbf{Q}_s^\dagger$ the 2-phonon symmetric and $\mathbf{Q}_s^\dagger \mathbf{Q}_m^\dagger$, the 2-phonon MS multiplet states. In other words, the 2_1^+ and 2_{ms}^+ states are treated as building blocks of vibrational structures in nearly spherical nuclei.

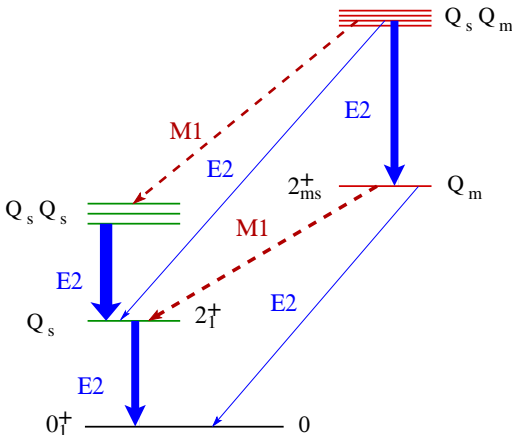


Figure 1.7: Decay scheme for MS states in a nearly spherical nucleus. The experimental signatures are depicted; the widths of the $E2$ and $M1$ arrows are proportional to the transition strengths.

1.4 ^{94}Zr and Collectivity

The nuclide $^{94}_{40}\text{Zr}_{54}$, with four neutrons above the $N = 50$ major closed-shell, belongs to the chain of Zr isotopes which demonstrate a shape transition as the number of valence neutrons increases. As shown in Figure 1.8, the nuclear structure of the even-A Zr isotopes evolves from the spherical $^{90}\text{Zr}_{50}$ to the strongly deformed nucleus ^{102}Zr [18, 19, 20, 21, 22], with a subshell closure at $N = 56$, evinced by ^{96}Zr [20]; there is evidence of shape coexistence in ^{100}Zr [21]. This nuclear structure evolution is verified by the $B(E2; 2_1^+ \rightarrow 0_1^+)$ values, as given in the National Nuclear Data Center (NNDC) database [8]. In comparison to other Zr isotopes, the level scheme of ^{94}Zr is very similar to that of ^{92}Zr , and it is expected that the low-lying excited states in ^{94}Zr would exhibit somewhat vibrational character.

The original motivation for studying the low-lying states in $^{94}_{40}\text{Zr}_{54}$ with inelastic neutron scattering was the experimental identification of multiphonon symmetric and MS excitations, such as those seen in ^{94}Mo [23, 24]. The nucleus $^{94}_{42}\text{Mo}_{52}$, with two protons above a subshell closure and two neutrons above a major closed shell, is considered a spherical nucleus, and these excitations could be described as mentioned above. These interesting findings initiated a series of experiments on neighboring isotones ($N = 52$), i.e., ^{92}Zr and ^{96}Ru , in which the one-phonon MS state and members of two-phonon MS states were observed [25, 26, 27]. Also, for the first time in an odd-A nucleus, ^{93}Nb , candidates for the one-phonon MS states have been proposed [28]. Interestingly, the $B(M1)$ value, the magnetic dipole transition strength, increases as the number of protons increases (40 in ^{92}Zr to 44 in ^{96}Ru), as listed in Table 1.1. For comparison, the reduced transition strengths, $B(E2)$ values, for $2_1^+ \rightarrow 0_1^+$ and $2_{ms}^+ \rightarrow 0_1^+$ are listed in the table as well. One could relate the data in Table 1.1 to the $E2$ and $M1$ transition strengths shown in Figure 1.7. The $B(E2)$ value

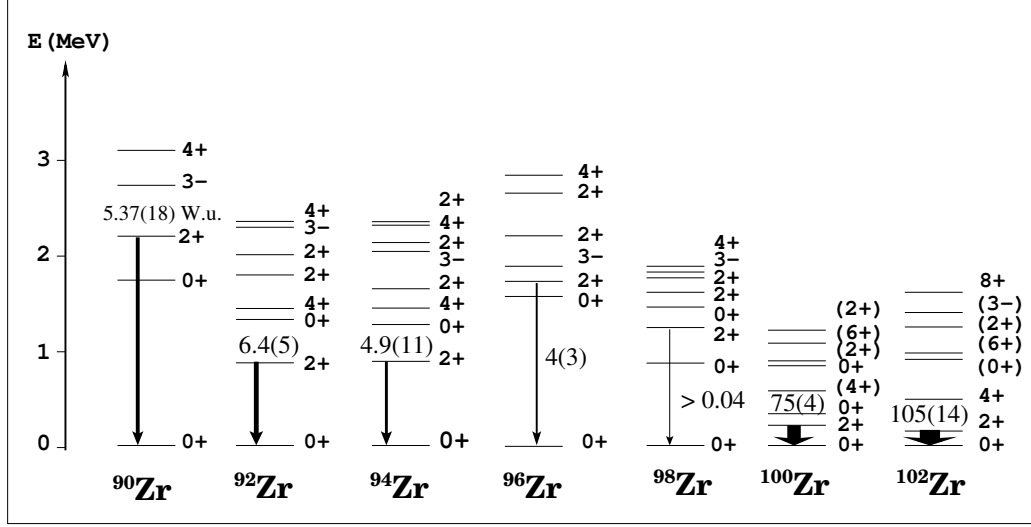


Figure 1.8: Evolution of the nuclear structure of the Zr isotopes from the level schemes and $B(E2)$ values. The ^{94}Zr level scheme is similar to that of ^{92}Zr .

is usually expressed in Weisskopf units, W.u., which is related to the nucleus mass number, A , by $B(E2)$ (W.u.) = $0.0594 \times A^{4/3} e^2 fm^4$. These units are discussed in Chapter 3.

Table 1.1: The characteristics of the one-phonon MS and symmetric states in the neighboring $N=52$ and 54 isotones.

Nucleus	E_l, J_i^π (keV)	$B(M1; 2_{ms}^+ \rightarrow 2_S^+)$ (μ_N^2)	$B(E2; 2_{ms}^+ \rightarrow 0_1^+)$ $B(E2; 2_1^+ \rightarrow 0_1^+)$ (W.u.)
$^{96}_{44}\text{Ru}_{52}$	2284.2(3), 2_3^+ 832.6(1), 2_1^+	0.78(23)	1.6(3) 18.1(5) [26]
$^{94}_{42}\text{Mo}_{52}$	2067.4(1), 2_3^+ 871.09(10), 2_1^+	0.56(5)	1.8(2) 16(1) [24]
$^{92}_{40}\text{Zr}_{52}$	1847.3(1), 2_2^+ 934.46(10), 2_1^+	0.37(4)	3.4(4) $6.4^{+0.6}_{-0.5}$ [25]
$^{96}_{42}\text{Mo}_{54}$	2095.73(5), 2_4^+ 778.22(5), 2_1^+	0.17(2)	$0.08^{+0.02}_{-0.01}$ 20.7(3) [33]

Valuable experimental data, along with theoretical calculations [29, 30, 31, 32], have contributed to the knowledge of the interplay of protons and neutrons in collective nuclear structures. In connection with the experiments mentioned on the $N=52$ isotones, an $(n, n'\gamma)$ study was performed on ^{96}Mo [33] at the University of Kentucky facility. One interesting result of this study was that the $B(M1)$ value was much smaller than in ^{94}Mo . The question of how MS states in these neighboring nuclei evolve was to be addressed by studying another $N=54$ isotone, ^{94}Zr .

Even though ^{94}Zr has been studied with many different probes (Ref. [34] and refer-

ences therein), information on transition strengths is scarce. The available experimental data on the low-lying states in ^{94}Zr are limited to lifetimes for the first three excited levels, 2_1^+ , 0_2^+ , 4_1^+ and multipole mixing ratios for a few transitions with no further information [34]. In an earlier $^{94}\text{Zr}(n,n'\gamma)$ measurement at the University of Kentucky, which was performed by Glasgow and coworkers in 1970s [35], no information on lifetimes were obtained. In recent years, the Doppler-shift attenuation method (DSAM) have been employed at the University of Kentucky facility to measure the lifetime of the levels in the low-lying states. The objective of this project was to study the low-lying states in ^{94}Zr excited by inelastic neutron scattering, which allows us to measure the lifetimes and therefore, the transition strengths to identify the one-phonon and possibly members of the two-phonon MS states, as well as other collective excitations. Also, with the help of modern technologies in γ -ray detection more information were obtained. This dissertation is organized into 5 chapters. The experimental methods are described in Chapter 2, with details on the experiments performed at the University of Kentucky, Section 2.2, and Triangle Universities Nuclear Laboratories (TUNL), Section 2.3, followed by the data analysis in Chapter 3. The experimental results are provided in Chapter 4, along with a discussion on the decay scheme. A detailed discussion of the low-lying states in ^{94}Zr is presented, which also includes the shell model and IBM-2 calculation results in Sections 4.4.1 and 4.4.2, respectively. Parts of our publications [36, 37] are included in Chapter 4. The conclusions of this study are summarized in Chapter 5.

CHAPTER 2: EXPERIMENTAL PROCEDURES

2.1 Inelastic Neutron Scattering, the $(n,n'\gamma)$ Reaction

The low-lying states in ^{94}Zr were studied with the inelastic neutron scattering (INS), $(n,n'\gamma)$ reaction. The INS method with γ -ray detection has proven to be a very useful tool in studies of the nuclear structure of stable nuclei, and has several advantages over other experimental probes [38], as demonstrated, for example, in Refs. [24, 25, 19, 39].

The neutrons, with no Coulomb barrier, can excite the low-lying levels very close to their excitation thresholds, hence eliminating the complications related to feeding by radiation from higher-lying levels. This property facilitates the study of a level in more detail and with less ambiguity.

The INS reaction at low incident neutron energies is generally of a statistical nature and non-selective, where all nuclear levels, typically up to spin $J \leq 6$, regardless of their structure are populated. The reaction occurs mainly through the compound-nucleus (CN) or statistical mechanism, similar to heavy-ion evaporation reactions [40]. A projectile neutron and the target nucleus form a compound system, which lasts for 10^{-20} to 10^{-18} seconds. The scattered neutron leaves the system after imparting some of its energy to the target nucleus, leaving it in an excited state. The de-excitation of the nucleus occurs by emission of γ rays or internal conversion electrons. The nuclear structure of the target nucleus can be studied by detection and characterization of either scattered neutrons or emitted γ rays. The availability of high-purity germanium (HPGe) detectors with about an order of magnitude better resolution than that obtained with neutron detectors, favors γ -ray spectroscopy. The nuclear structure of ^{94}Zr was studied by measuring the properties of the γ rays collected.

The $(n,n'\gamma)$ reaction is, however, limited to stable nuclei and, due to the low intensity of the neutron flux, large amounts of material, ≥ 0.1 mole, of highly enriched isotopic samples are required. The ZrO_2 sample, 40.5241 grams and enriched to 98.57% ^{94}Zr , in powder form and on loan from Oak Ridge National Laboratory, was used in these measurements. The other Zr isotopic contaminants are given in Table. 2.1, where the elimination of possible γ rays from these isotopes was considered in the spectral analysis in all of our experiments.

Table 2.1: Contaminants of other Zr isotopes in the scattering sample of ^{94}Zr .

Isotope	Percentage
^{90}Zr	0.71%
^{91}Zr	0.21%
^{92}Zr	0.39%
^{96}Zr	0.12%

2.1.1 Neutron Production and Gamma-Ray Detection

The monoenergetic neutrons used in the inelastic neutron scattering reactions were produced through two reactions:

$${}^3H(p, n){}^3He, \quad Q = -0.76 \text{ MeV} \quad (2.1.1)$$

$${}^2H(d, n){}^3He, \quad Q = 3.27 \text{ MeV}, \quad (2.1.2)$$

where in the nuclear structure $X(a, b)Y$ notation, X and Y are the target and residual nuclei, a and b the projectile and ejectile, respectively. The projectile beam of protons or deuterons was produced by an electrostatic accelerator. The γ rays emitted by the excited nucleus following the INS reaction can be detected with different experimental setups. In $(n, n'\gamma)$ singles-mode experiments, only one detector is used, whereas in $(n, n'\gamma\gamma)$ coincidence measurements several detectors are used in coincidence mode [38, 41].

2.1.2 The Experimental Methods

The experimental methods employed to study low-lying states in ${}^{94}\text{Zr}$ were:

- **Excitation functions**

The purpose of the excitation function measurements was the identification of the γ rays emitted from the de-exciting nucleus, their energy thresholds, and limitations on the spins of the levels from which these transitions arise.

- **Angular distributions**

The angular distribution measurements provided more detailed information about the characteristics of the γ -ray transitions, i.e., branching ratios and multipole mixing ratios of the transitions, spins and lifetimes of the levels. From these data the transition strengths can be calculated. Identification of MS or symmetric phonon states and their multiphonon excitations is possible by knowing the transition multipolarities and their strengths of decays from the low-lying states of the nucleus.

- **Coincidence measurements**

A decay scheme of the nucleus was constructed based on $\gamma\gamma$ coincidence and excitation function data.

The first two measurements, referred to as singles-mode measurements in the following sections, were carried out at the University of Kentucky. The $\gamma\gamma$ coincidence measurements were performed at Triangle Universities Nuclear Laboratory, TUNL, at Duke University. Details of these experiments are discussed in the following sections.

2.2 The Experimental Setup at the University of Kentucky

$^{94}\text{Zr}(n,n'\gamma)$ singles-mode measurements, excitation function and angular distribution measurements, were carried out at the University of Kentucky 7 MV electrostatic accelerator facility, which can deliver pulsed beams of protons, deuterons, ^3He , or ^4He at voltages up to 6.5 MV. A 1.875-MHz pulsed beam of protons with a 533-ns duration and 10 to 15 ns in width was generated by the accelerator. The pulsed beam was bunched further to 1-2 ns in width. A 90° analyzing magnet and sets of electrostatic and magnetic quadrupoles guided the pulsed beam of protons of $2\text{-}\mu\text{A}$ current through the vacuum beam line to a gas-filled cell in the neutron hall.

At this facility, the reactions given in Eqns. 2.1.1 and 2.1.2 can be used for studies with the INS method, providing a large range of nearly monoenergetic neutrons ($\Delta E \approx 60$ keV, at $E_n = 2.0$ MeV), from 0.5 MeV to 9.5 MeV. For measurements on ^{94}Zr , however, the reaction in Eqn. 2.1.1 was employed. The tritium gas cell is a tantalum-lined stainless steel cylinder of 1-cm outer diameter and 3-cm length filled with tritium gas, up to 1 atm of pressure. The gas cell is isolated from the vacuum beam line by a $3.5\ \mu\text{m}$ molybdenum foil. The neutrons produced strike the scattering sample at a short distance from the tip of the gas cell with a flux of approximately 4×10^6 neutrons/cm²/s at 5 cm from the gas cell. The sample-gas cell distance should provide a sufficient solid angle to have an optimized flux of neutrons on the scattering sample.

The scattering sample consisted of 20.0314 grams of $^{94}\text{ZrO}_2$ in a cylindrical polyethylene vessel, 2.6 cm in diameter and 3.9 cm in height. The vessel was sealed completely and a nylon thread was used to suspend the sample in a balanced position in front of the tritium gas cell. The position of the scattering sample in front of the gas cell was adjusted by the help of a special viewer (Kern-Swiss eyepiece) at 0° with respect to the beam line, located at approximately 4 meters from the end of the beam line. Today, this viewer is replaced by a fixed laser level. The center of the sample was aligned with the center of the gas cell end, to guarantee uniform exposure to the incident neutrons.

The emitted γ rays from the de-exciting nucleus were detected by an n-type coaxial HPGe detector, with 55% efficiency relative to a 3-inch \times 3-inch cylindrical NaI(Tl) scintillator. The detector had a FWHM of 1.8 keV at 1.33 MeV, a γ -ray emitted by a ^{60}Co radioactive source. Fast neutrons could cause damage to the HPGe detector. Therefore, proper shielding is employed to protect the detector and also reduce the background in the γ -ray spectra. The HPGe detector is protected by a boron-loaded polyethylene shield with rings of lead inserted and a fore-shield of several copper slabs. A tungsten wedge is set close to the tritium gas cell to protect the detector from direct neutrons, as shown in Figure 2.1. The physical setup is shown in Figure 2.2. In order to reduce the background radiation, especially low-energy radiation from the Compton scattering processes, an annular BGO, bismuth germanate ($\text{Bi}_4\text{Ge}_3\text{O}_{12}$), scintillator surrounds the HPGe detector and serves as an

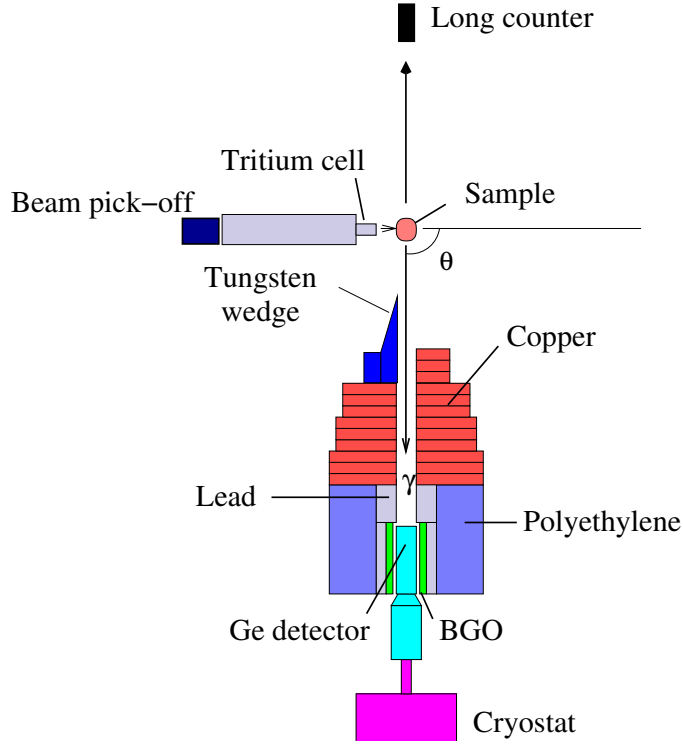


Figure 2.1: Schematic of the experimental setup for singles-mode measurements at the University of Kentucky facility. The figure is not to scale.

active Compton suppression shield. In the prompt spectrum, the background is suppressed by greater than a factor of four [40]. The assembly of the HPGe and BGO together with the shielding is mounted on a carriage or goniometer, which is pivoted about the position of the scattering sample. The goniometer is moved manually to change the angle of the detector with respect to the incident neutrons. Before the start of the experiment, the pivot point about which the goniometer rotates was checked to be exactly positioned at 0° with respect to the beam line.

The advantageous technique of time-of-flight (TOF) gating was employed to reduce background in the prompt γ -ray spectra [42]. This technique is based on the difference in the velocities of the reaction products, e.g., scattered neutrons and the γ rays from the $(n,n'\gamma)$ reaction. A prompt gate is defined as the time window in which the γ rays from the scattering sample (beam-correlated events) are recorded, rejecting the non-correlated events (background); see Section 2.2.2. A schematic of a TOF spectrum is shown in Figure 2.3.

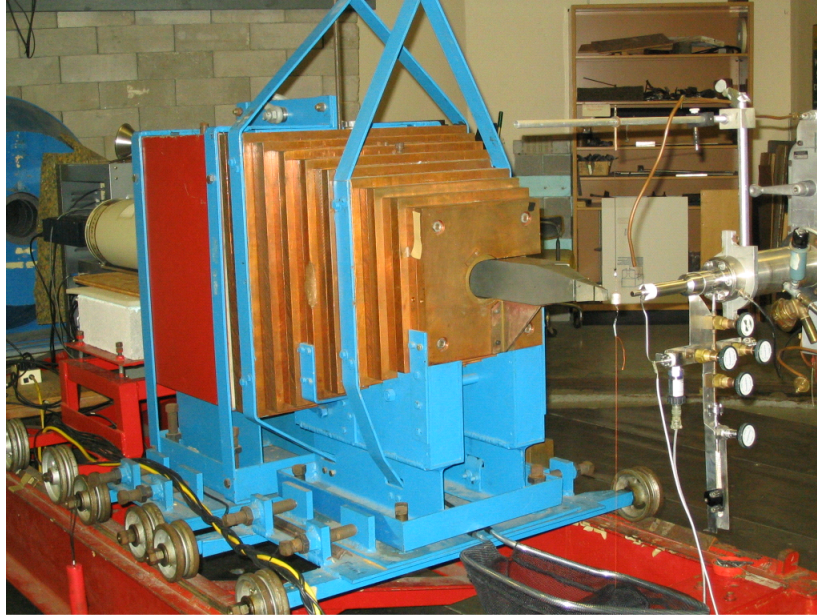


Figure 2.2: Picture of the $(n,n'\gamma)$ singles measurement setup. The tritium gas cell, scattering sample, shielding, and part of the HPGe detector cryostat are shown.

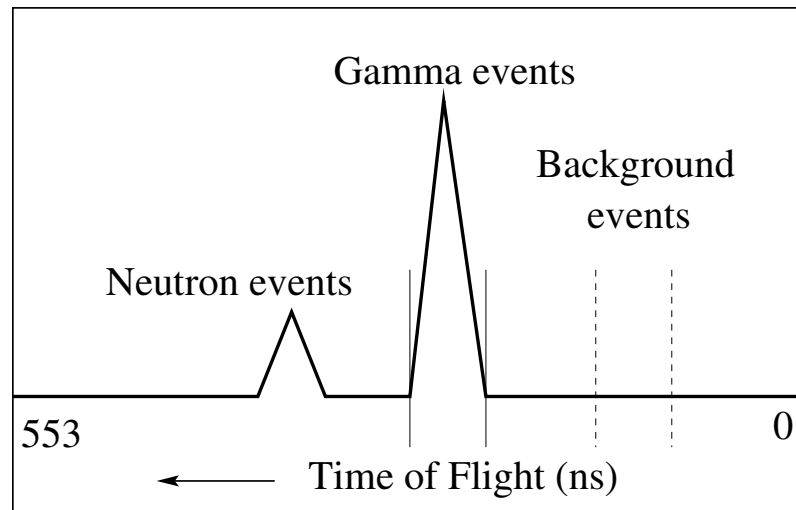


Figure 2.3: Schematic of a TOF spectrum. The prompt gate is applied to record only beam-correlated γ -ray events, rejecting the uncorrelated events.

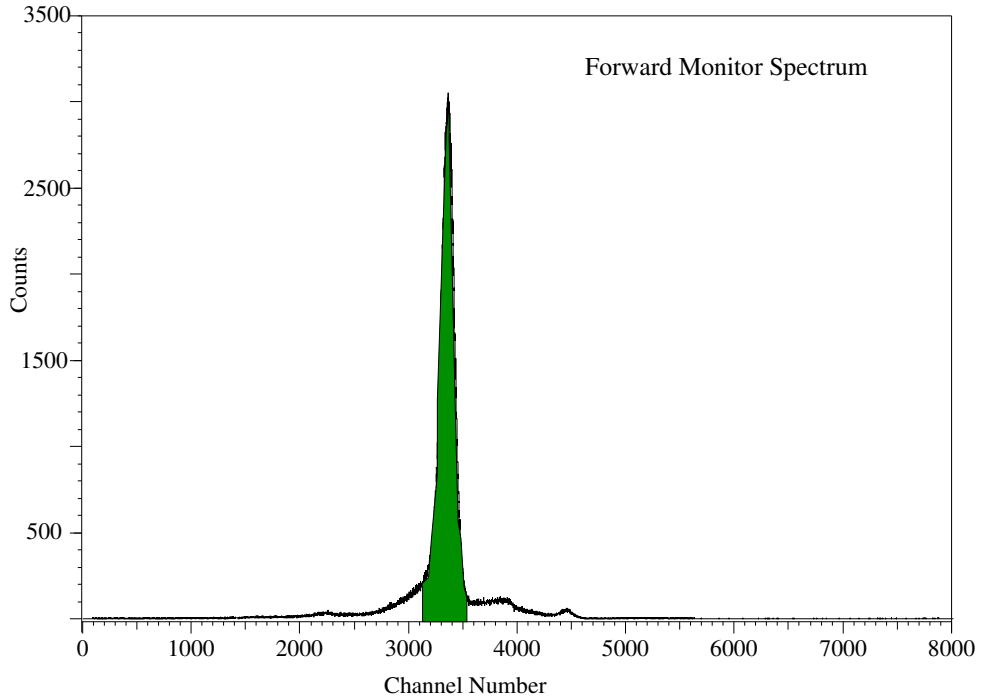


Figure 2.4: Forward monitor spectrum obtained in a $^{94}\text{Zr}(n,n'\gamma)$ angular distribution measurement. The highlighted area under the neutron peak is used for normalization. The data was taken at $E_n = 2.3$ MeV.

2.2.1 Neutron Detection for Normalization Purposes

The flux of neutrons incident on the scattering sample during an experiment should be measured in order to normalize the γ -ray yields. The long counter and forward monitor were used as designated neutron monitors to record the neutron flux in each measurement. The long counter consisted of a $^{10}\text{BF}_3$ -filled proportional counter embedded in polyethylene. The polyethylene is used to thermalize the neutrons with high energies to be detected by the counter. More details on the long counter neutron detector can be found in Ref. [43]. The long counter was located at ≈ 4 m from the gas cell at 90° with respect to the beam line. Its spectra cannot provide any timing or energy information; it only measures the flux of neutrons produced in an experiment. The forward monitor is an NE-218 organic liquid scintillator, placed on a shelf at 43° with respect to the beam line. This type of detector is sensitive to both neutrons and γ rays, but produces different pulse shapes for each. The events solely due to neutrons can be selected by pulse shape discrimination. The area of the neutron peak in the forward monitor spectrum can be used as a normalization factor for the γ -ray yields (see Figure 2.4). In ^{94}Zr measurements, only the long counter was used for normalization; see Section 3.4.

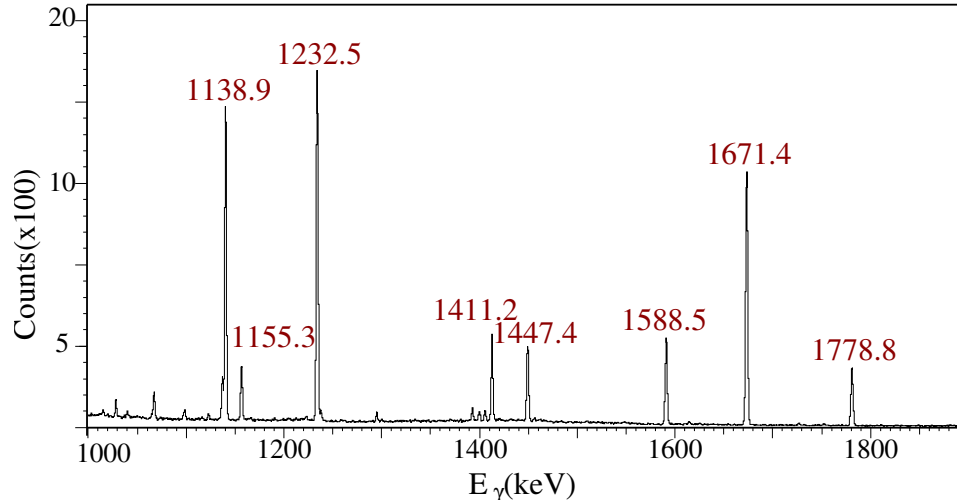


Figure 2.5: γ -ray spectrum obtained in $^{94}\text{Zr}(n,n'\gamma)$ excitation function measurement at $E_n = 3.5$ MeV and $\theta = 90^\circ$ detection angle.

2.2.2 Data Acquisition and Electronics Setup

The data acquisition system operates through a CAMAC (Computer Automated Monitoring And Control) crate on a Linux operating system. The details of the setup were documented by Nigel Warr [44]. The crate contains several ADC's (Analog-to-Digital Converter), depending on the measurement hardware setup. The prompt and background γ -ray spectra, forward monitor histogram, as well as the long counter, charge, and time scalars were defined according to their hardware setup in the singles-mode measurements. The software also provides a linear energy calibration for the γ -ray spectra, as discussed in Section 2.2.3.

The electronics setup used in this experiment was the standard setup for singles measurements at the University of Kentucky facility. The principal characteristic of the data acquisition is the use of a pulsed beam for TOF discrimination, which reduces the background radiation in the spectra. The γ rays produced from Compton scattering processes were suppressed by the BGO shield when it is employed in anti-coincidence mode with the HPGe detector. TOF information is provided by a beam pick-off positioned close to the end of the beam line. Figure 2.5 shows an example of a Compton and background suppressed γ -ray spectrum obtained in these measurements.

The electronics schematic diagram is shown in Figure 2.6. The timing signals from the HPGe detector, BGO, and the beam pick-off provide information about the time at which an event, i.e., the detection of a γ ray, has occurred. The prompt and background time gates were selected, based on the TOF spectrum shown in Figure 2.3. The time-of-flight spectrum is a digitized histogram of a TAC/SCA (time-to-amplitude converter/single channel analyzer) module. The two peaks in the TOF spectrum correspond to the events

from neutrons and γ rays, both time-correlated with the beam pick-off. The γ rays reach the detector faster than the neutrons. The prompt time gate is made on the γ -ray events, and the background time gate is made on the background. These two gates usually have equal widths, and the time limits can be adjusted on the TAC modules by viewing their histograms on an MCA (multi-channel analyzer).

The time gates were applied to the energy signal from the HPGe detector to record a histogram by the ADC module, and obtain the prompt and background γ -ray spectra. The beam pick-off is a small cylinder at the end of the beam line, shown in Figure 2.1, which produces a signal based on the pulsed beam (1.875 MHz). It serves as a time reference to distinguish between the signals from the scattering sample and the background. Further constraints on the time signals in the HPGe and BGO provided a Compton suppressed γ -ray spectrum. For example, if the signals from the HPGe detector and the BGO are time-correlated, within the beam pick-off time window, the signal is vetoed and not recorded. The prompt spectrum represents the events from the HPGe detector, time-correlated with the beam pick-off, but not with the BGO signal. This constraint gives a ratio of prompt γ rays to total events $\approx 1/3$. The rate of the prompt γ -ray detection was typically 100-200 counts.

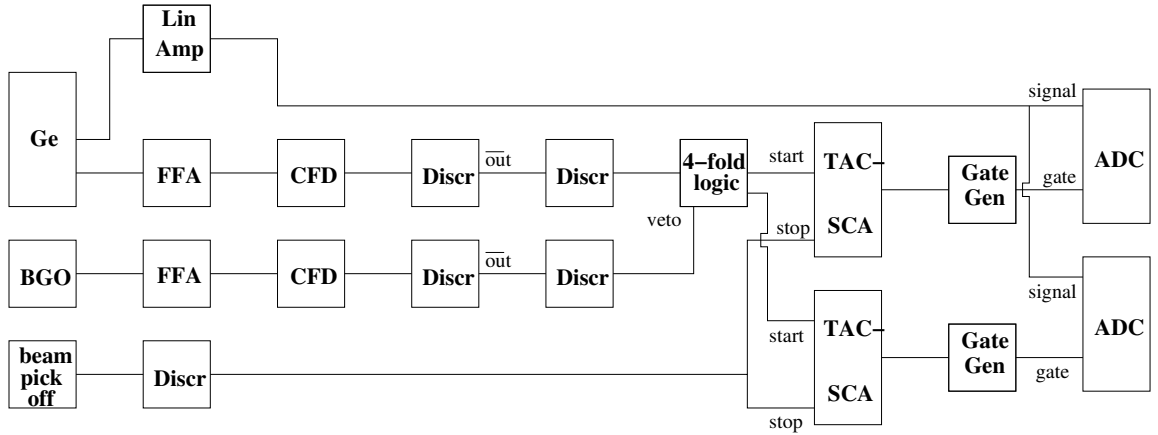


Figure 2.6: The UK singles-mode measurement electronics, Ref. [44]

Figure 2.7(a) shows the electronics diagram for the long counter and the schematic of the forward monitor setup is shown in Figure 2.7 (b). More details about these hardware setups can be found in Ref. [44].

2.2.3 Excitation Function Measurements

In these measurements, the incident neutron energy was varied from 2.5 to 4.0 MeV in 100-keV intervals, while the detector position was fixed at 90° with respect to the beam

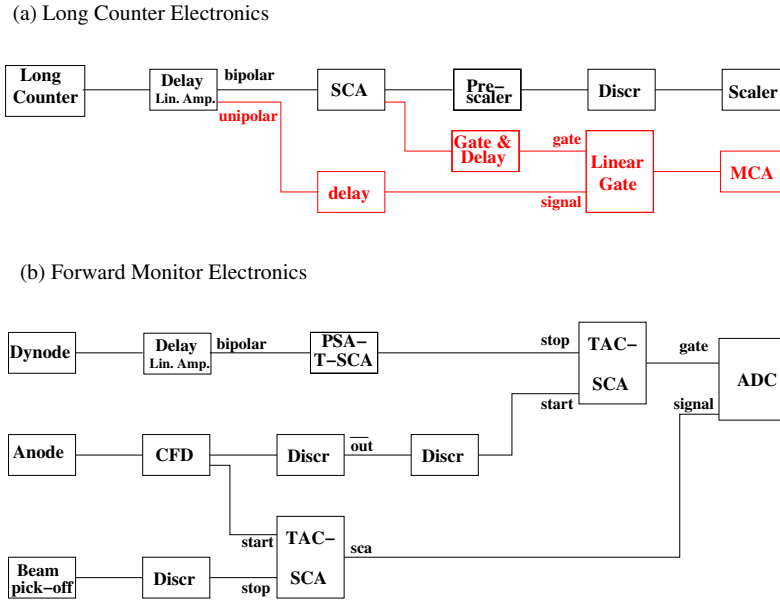


Figure 2.7: The long counter and forward monitor electronics, Ref. [44]

line. The geometry of the experimental setup is given in Table 2.2. The data were taken for a total of 172 hours. A γ -ray spectrum obtained in a $^{94}\text{Zr}(n,n'\gamma)$ excitation function measurement at $E_n = 3.5$ MeV is shown in Figure 2.8.

In order to calibrate the ^{94}Zr γ -ray spectra, radioactive ^{226}Ra or ^{152}Eu sources were used. The γ -ray energies of these standard sources are well known and do not widely differ from those to be measured in the ^{94}Zr nucleus. The radioactive source was placed in front of the detector and a γ -ray spectrum was acquired before the start of the ^{94}Zr measurements. A linear energy calibration ($E = a \times \text{Chn} + b$), was performed with two points to determine a and b . In the ^{226}Ra spectrum, the positions or channel numbers of two well-defined peaks and their corresponding energies, E , were used as inputs to *Spectrum Calibration* in the data acquisition software. This calibration was used just as a preliminary energy calibration of the spectra and more accurate calibrations were employed for later data analysis. More details about the calibration of the γ -ray spectra are presented in Chapter 3.

At the end of a measurement, the ^{226}Ra source was placed at the position of the scattering sample and a γ -ray spectrum was acquired for several hours. These data were used for the detector efficiency calibrations. Therefore, the electronics setup should be the same. In the absence of the beam, a pulser of the same frequency as the beam was used in place of the beam pick-off signal to acquire a γ -ray spectrum. The TAC window was open; in the absence of neutron, no rejection was necessary and all γ -ray events were recorded.

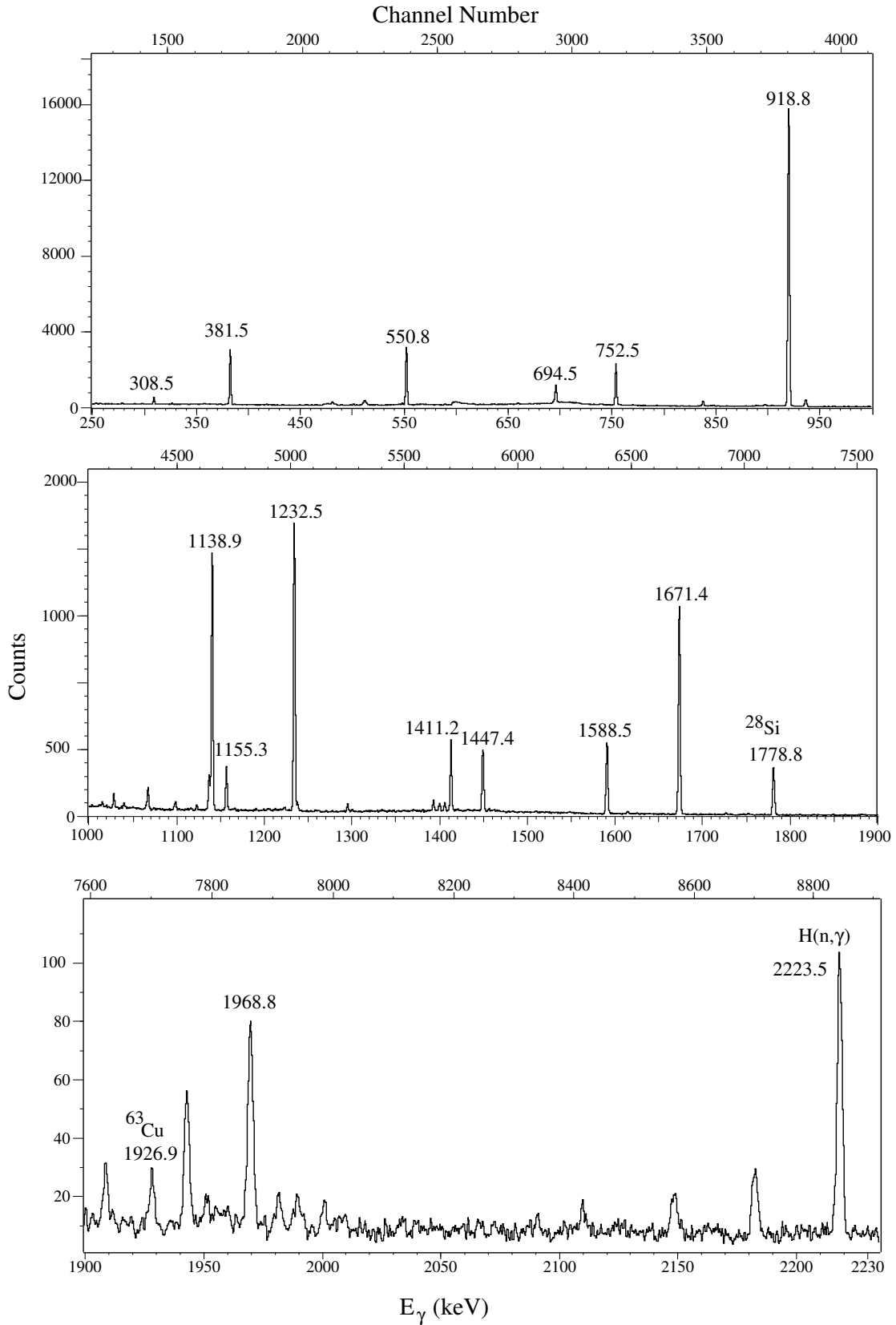


Figure 2.8: Energy sections of a singles-mode γ -ray spectrum of ^{94}Zr from the $(n,n'\gamma)$ reaction at $E_n = 3.5$ MeV and 90° . Some of the background γ rays are also shown.

Table 2.2: The geometric characteristics of the experimental setups for measurements at the UK facility. Exc. Ftn. refers to excitation function and Ang. Dis. to angular distribution measurements.

Experiment	Sample Center-T Cell Distance (cm)	Sample-HPGe Det. Distance (cm)
Exc. Ftn. ($E_n = 2.5 - 4.0$ MeV)	5.5	116.5
Ang. Dis. ($E_n = 2.3$ MeV)	6.0	112.5
Ang. Dis. ($E_n = 2.8$ MeV)	5.5	116.5
Ang. Dis. ($E_n = 3.5$ MeV)	6.0	112.5

Table 2.3: The list of the angles measured in the angular distribution measurements.

Angular Distribution	Angles (degrees)
$E_n=2.3$ MeV	40, 55, 67, 79, 90, 101, 113, 125, 140, 150
$E_n=2.8$ MeV	40, 55, 65, 72, 80, 90, 106, 116, 125, 137, 150
$E_n=3.5$ MeV	40, 55, 67.5, 79, 90, 101, 113, 125, 140, 146

2.2.4 Angular Distribution Measurements

In angular distributions, the observation angle is varied, while the incident neutron energy is kept constant. For ^{94}Zr , the angle of the detector relative to the beam was varied from 40° to 150° in approximately 10° intervals at several neutron energies in order to study the low-lying states excited by the reaction in more detail. The neutron energies were selected based on the energies of the levels of interest. Angular distributions at $E_n = 2.3$, 2.8 and 3.5 MeV were performed in search of one-phonon and two-phonon MS states. The data were taken for a total of 324 hours. The geometry of each experimental setup is given in Table. 2.2, and the list of the angles for each angular distribution are given in Table. 2.3.

An accurate knowledge of the γ -ray energies should be obtained from the angular distribution data. Radioactive sources with well-defined γ -ray peaks within the energy range of the γ rays emitted from the scattering sample should be used as on-line calibration sources. ^{24}Na γ rays of 1368.596(29) and 2753.849(40) keV met the requirements for the ^{94}Zr nucleus. The ^{24}Na source was in the form of a polyethylene ring filled with $^{23}\text{NaCl}$. The rings were exposed to ^{252}Cf , a source of thermal neutrons, to produce the ^{24}Na isotope. The half-life of ^{24}Na is about 15 hours, therefore, the Na ring was changed for each angle run, which lasted 12 hours. As in the excitation function measurements, the ^{226}Ra source was used for an energy calibration at the time of data acquisition and efficiency calibrations; see Chapter 3.

2.3 The Experimental Setup at TUNL

2.3.1 γ - γ Coincidence Measurements

Low-lying states in ^{94}Zr were studied through $\gamma\gamma$ coincidence measurements following inelastic neutron scattering, i.e., $(n,n'\gamma\gamma)$. In this technique, the γ rays which belong to the same cascade are detected in coincidence with the help of multiple detectors [38, 41]. Figure 2.9 shows an example of two cascades in a nucleus. Any transition is connected to another transition in a cascade manner, e.g., $\gamma 2$ is in coincidence with $\gamma 1$ and $\gamma 3$, but not with $\gamma 4$ and $\gamma 5$. Along with the excitation function data, the coincidence information can be used to place the γ -ray transitions and build the decay scheme of the nucleus of interest.

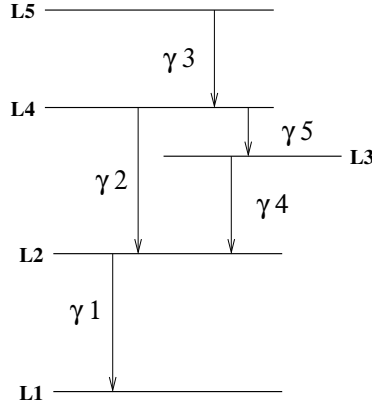


Figure 2.9: Example of two cascades in a nucleus. $L5 \rightarrow L4 \rightarrow L2 \rightarrow L1$ is one cascade and $L5 \rightarrow L4 \rightarrow L3 \rightarrow L2 \rightarrow L1$ is another cascade.

The γ rays are detected by several detectors placed at various angles with respect to the scattering sample. The detectors are placed very close to the scattering sample to improve the efficiency of detection of such coincidence events. In order to shield the detectors from the incident or scattered neutrons, the incident neutrons are collimated and the scattering sample is placed at a large distance from the neutron source compared to the singles measurements. At the University of Kentucky facility, $\gamma\gamma$ coincidence measurements are performed by the use of four HPGe detectors in closed geometry, without Compton suppression, see Section 3.8. Details on $(n,n'\gamma\gamma)$ measurements at the UK facility can be found in Refs. [38, 41, 45]. The coincidence data analysis is discussed in Appendix G.

It was in the interest of our collaborators from TUNL (Triangle Universities Nuclear Laboratories) to perform an $(n,n'\gamma\gamma)$ experiment at their facility, using clover detectors with higher detection efficiency and equipped with Compton suppression shields. This presented an opportunity for us to perform such experiments using a different setup and examine the differences between the data taken at the TUNL and UK. The $\gamma\gamma$ coincidence

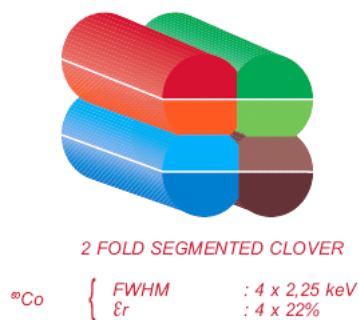


Figure 2.10: A schematic of a clover detector used in coincidence measurements. The four single Ge crystals are placed in a 4-fold clover. The FWHM value for each quadrant is 2.25 keV at 1.33 MeV from ^{60}Co .

experiments for ^{94}Zr were performed in the shielded neutron source area at the TUNL facility at Duke University, in collaboration with Dr. Anton Tonchev and his research group. This experiment was the first $(n,n'\gamma\gamma)$ measurement performed at this facility.

At TUNL, the monoenergetic neutrons were produced via reaction 2.1.2, $d(d,n)$, by delivering a deuteron beam from the 10-MV FN Tandem electrostatic accelerator on a deuterium gas cell. The gas cell is mounted at the end of the 20° -beam line inside the shielding wall. The multi-layered shielding wall is composed of concrete, paraffin, lead, steel, and iron to reduce the background radiation in the target area. There is an opening inside the shielding wall for neutron collimation. A double-truncated collimator, 79 cm long and made from tapered copper and polyethylene bars, is fitted inside the opening 33.5 cm from the deuterium gas cell. This collimator minimizes the neutron scattering from the inner sides of the wall, so the scattering sample can be exposed to a spatially homogeneous field of unscattered neutrons [46].

Three clover detectors, each equipped with a BGO Compton suppression shield, were used to record the coincidence events. A clover detector consisted of four two-fold segmented, n-type Ge crystals side-by-side in the geometry of a four-leaf clover, as shown in Figure 2.10. The relative efficiency of each detector was $4 \times 22\%$ and a FWHM of 2.25 keV for each quadrant at the 1.33 MeV γ -ray emitted by a ^{60}Co source. The high efficiency of the clover detectors made them very applicable to modern γ -ray spectroscopy. A liquid scintillation neutron detector was placed at 0° with respect to the neutron beam at approximately 2 m from the scattering sample to monitor the neutron beam characteristics [46]. The scattering sample consisted of 20.4501 grams of $^{94}\text{ZrO}_2$ powder enriched to 98.57% ^{94}Zr in a 2.6 cm \times 3.9 cm cylindrical vessel, and it was suspended at 214 cm from the shielding wall. The experimental setup diagram and the physical setup are shown in Figures 2.11 and 2.12.

Table 2.4: The composition of the Havar foil used in the D-gas cell at TUNL .

M	Nucleus (Z)	Fraction
52.00	Cr (24)	0.2000
55.85	Fe (26)	0.2170
58.93	Co (27)	0.4250
58.71	Ni (28)	0.1300
183.85	W (74)	0.0280

The deuterium gas cell was 3.15 cm long and 1 cm in diameter, and was isolated from the beam line by a 6.35 μm (0.25 mil) Havar foil window. The Havar foil composition is given in Table. 2.4. At the beginning of the $^{94}\text{Zr}(n,n'\gamma\gamma)$ experiment, the gas cell was filled up to 7 atm in pressure. The Havar foil was ruptured twice during the first day of the experiment. Therefore, the gas pressure was reduced to 5 atm for the rest of the experiment.

A pulsed deuteron beam with a repetition rate of 2.5 MHz and current up to 2 μA was delivered to the gas cell to produce a 5-MeV neutron beam. A pulsed beam of 2-ns width and energy spread of $\Delta E_n \approx 300$ keV was initially obtained. Pulsed-beam maintenance required special attention. The pulsed beam was lost in the middle of the first night shift, and hence, the rest of the experiment was carried out with a DC (continuous) beam. The coincidence data from the first few runs with the pulsed beam and with the DC beam were inspected and did not show any significant differences.

The clover detectors were mounted on movable plates, so different detection angles were provided by rotation of these plates about the target (0° to 140°). The plates also moved in radial directions to provide different distances, ranging from 0 to 26 cm from the scattering sample. The detector distances were measured from the scattering sample to the front window of the clover detectors and the angles were measured with respect to the neutron beam in the clockwise direction. The position of the detectors are given in the setup diagram of Figure 2.11.

The standard radioactive sources, ^{60}Co , ^{22}Na , ^{152}Eu , and ^{226}Ra , were used for energy and efficiency calibrations for each clover in single modes. The geometries of the clovers were changed for the efficiency measurements, due to the high counting rates. The three clovers, 1, 2, and 3, were moved to 8.4, 14.7, and 9.35 cm from the scattering sample position at angles of 269° , 132.5° , and 116° , respectively.

2.3.2 Electronics and Data Acquisition System

Each clover detector consisted of four quadrants and the coincidences between any two quadrants should be considered. The signal from each quadrant was treated as a single detector signal, which carries time and energy information; a total of 24 signals were to be processed. The electronics setup for the coincidence measurements is shown in Figure 2.13;

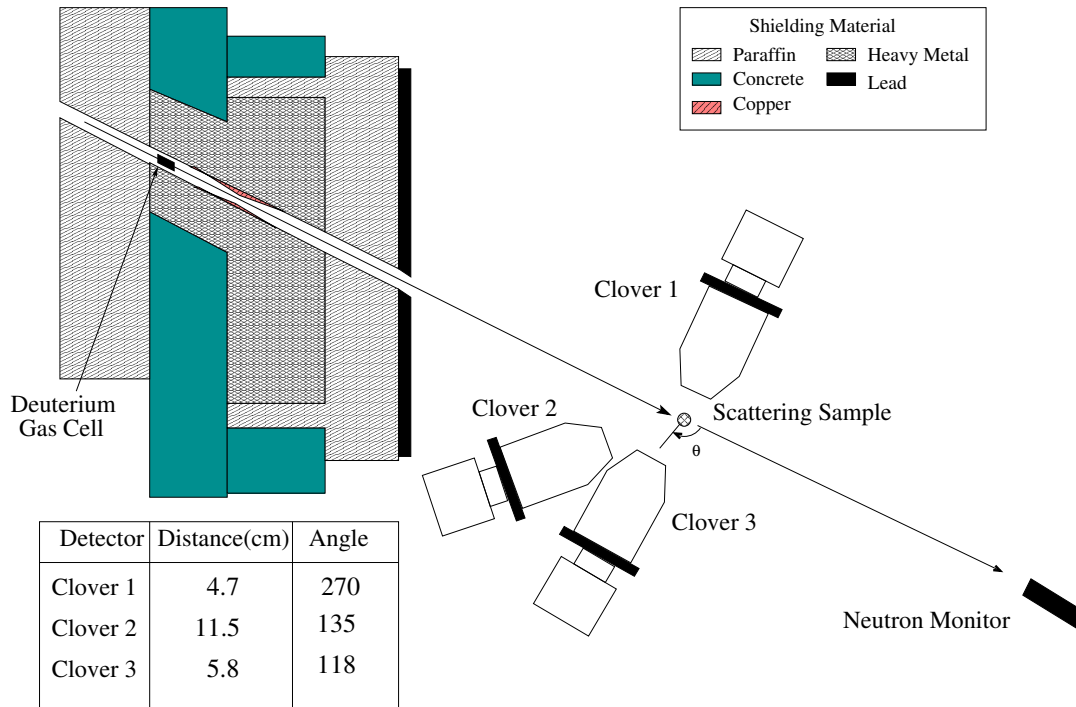


Figure 2.11: Schematic of the γ - γ coincidence setup at the TUNL facility. The detailed specifications of the shielding are from Ref. [46].

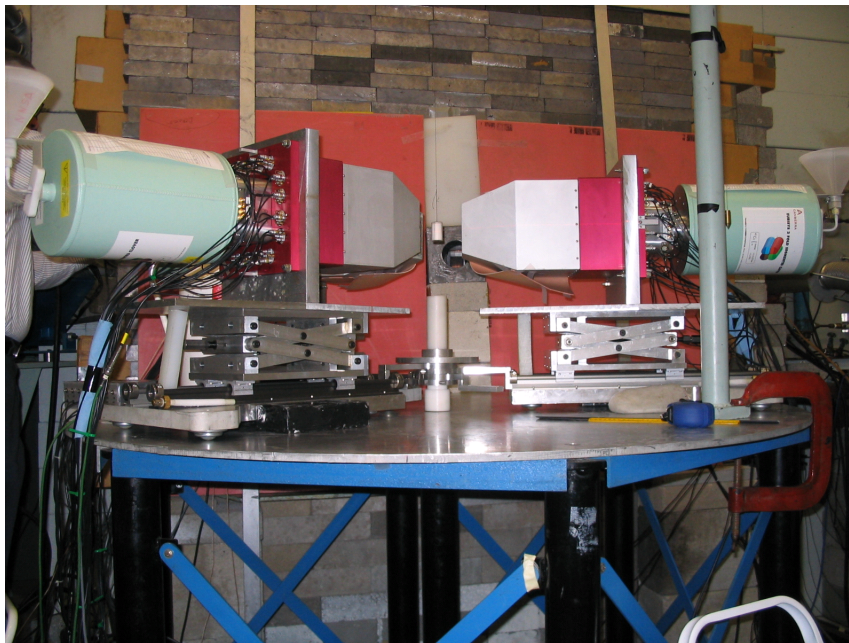


Figure 2.12: Photograph of the experimental setup used in ^{94}Zr coincidence measurements at the TUNL facility.

the setup is shown for only one detector, and the same electronics were applied to the other two clovers. The timing signal from quadrant 1 in clover 1 was used as a trigger for other

quadrants, see Section 3.8.1.

The timing signals were used to determine a coincidence time window, a time in which coincidence events between any two quadrants were recorded. In another words, if any two quadrants fired within that coincidence time window, the signal was recorded as a coincidence event. In jargon, this is called “two-fold” multiplicity. In more complicated coincidence setups where many more detectors are used, multiplicities up to 4-fold can be acquired. When a pulsed beam is used, the time reference for the detectors can be supplied by the pulsed beam. Since a DC beam was used, there was no such time reference for the quadrant time signals; therefore, a relative time between any two quadrants was considered. The time in which Quadrant1 in Clover1 fired was used as a reference time for other quadrants. More details will be discussed in Chapter 3.

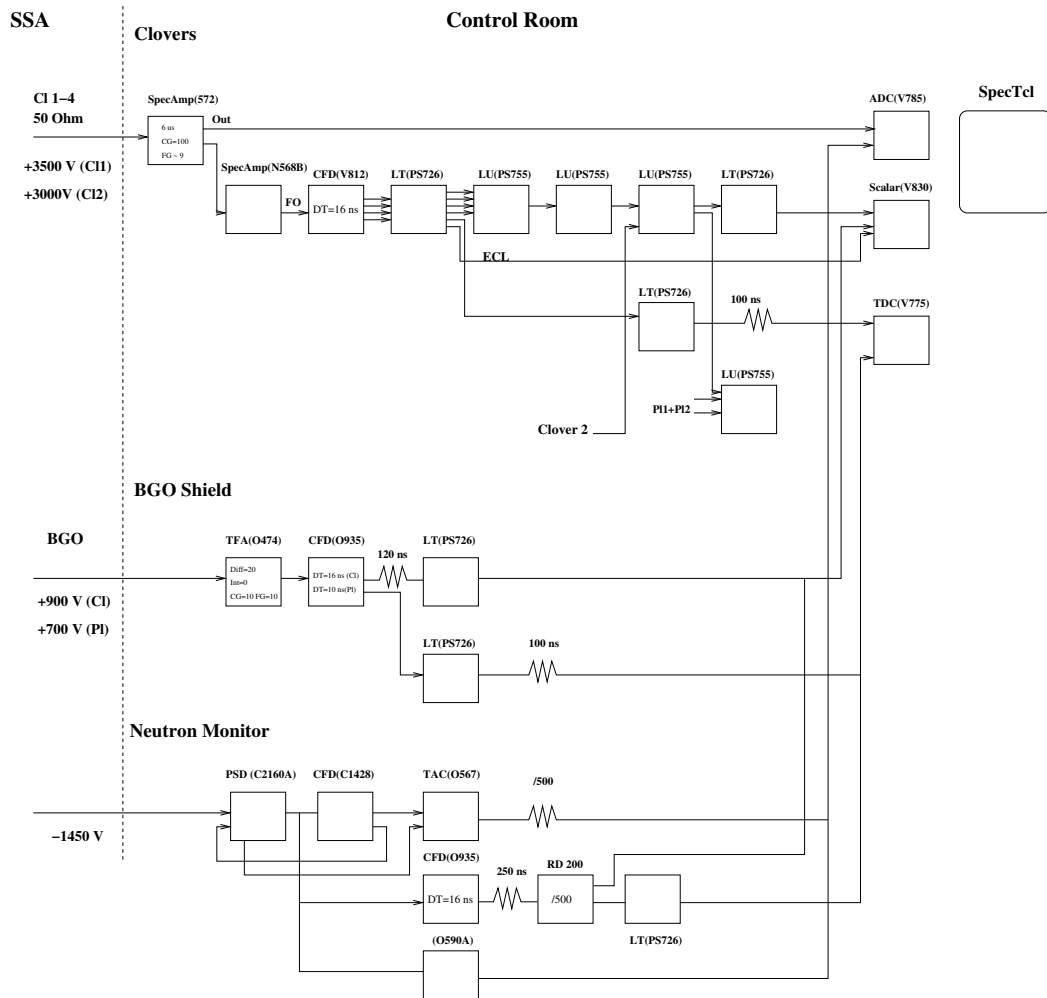


Figure 2.13: Schematic of the electronics setup for $^{94}\text{Zr}(n,n'\gamma\gamma)$ coincidence measurements at the TUNL facility.

The data acquisition was performed by SpecTcl software, developed at the National Superconducting Cyclotron Laboratory in Michigan State University [47]. At TUNL, for

the data acquisition in the $^{94}\text{Zr}(n,n'\gamma\gamma)$ experiment, a scripted **SpecTcl** was used. The scripts were in Tcl/Tk, pronounced “*tekel*”, command language [48]. In a separated *.tcl* script, the hardware parameters in the electronics setup were defined, as described in Appendix F.5. The data acquisition system was run by sourcing the *hardware94Zr.tcl* file in the **SpecTcl** Tk/Con prompt. The version of **SpecTcl** used in this measurement was only for data acquisition and/or on-line data analysis. A separated *.tcl* file, e.g., *uk_spectcl.tcl* Appendix F.4, was used to create spectra. The spectra were written in **Tv** format to be analyzed off-line; details are discussed in Section 3.7. The $^{94}\text{Zr}(n,n'\gamma\gamma)$ experiment ran for eight days, and a total of 105 hours of coincidence data with a counting rate of about 300 events per second were recorded.

CHAPTER 3: DATA ANALYSIS

3.1 Spectrum Calibrations

Energy, nonlinearity, and efficiency calibrations are among the most important corrections to be considered in γ -ray spectroscopy [43]. Since various peaks in the spectrum are to be properly identified, the first step is accurate energy calibration of the spectrum against the spectrum of a known radioactive source. The relationship between the energy of a γ -ray peak and its position in the spectrum, or corresponding channel number in the multi-channel analyzer (MCA), is not linear, even for the best spectrometers. The nonlinearity of a detector depends also on its stability in the course of an experiment, which usually lasts from a few days to a few weeks. Data from the ^{226}Ra spectrum provided the energy, nonlinearity and efficiency calibrations for the ^{94}Zr data. In this chapter, the computer codes used for data analysis are indicated in **bold**, and the input/output files in *italics*. The details on the data analysis procedures are documented in Ph.D. dissertation of Dr. Shelly Lesher [45].

For nonlinearity calibration, the **dsnonlin** code was used to fit a polynomial of 7th degree to the ^{226}Ra data. The sorted fitted parameters file, *fname.sho*, and a tabulated energy list, *fname.tab*, taken from Nuclear Data Sheets (NDS) [49] were inputs to the code. Figure 3.1 shows the nonlinearity curve for the excitation function measurements at the UK facility. The output file, *fname.nlp*, contains the coefficients of the polynomial fit.

A spectrometer's detection efficiency depends on the geometry of the detector, and also the source of the emitted γ rays, i.e., the scattering sample in these measurements. The efficiency calibration curve was obtained by comparison of the yields of the γ -ray peaks in the ^{226}Ra efficiency spectrum (see Section 2.2.3) to their standard intensities taken from NDS [49]. The output file of the code **effic**, *fname.prn*, *fname.spe_pic*, which contains the fitted parameters, and *fname.tab* files were used as inputs in **polyfit**. The output files were the calibration file, *fname.pol*, and a plot of $\ln(\text{efficiency})$ as a function of $\ln(E_\gamma)$. Figure 3.2 shows a 5th-order polynomial fit to the data used in $^{94}\text{Zr}(n,n'\gamma)$ excitation function measurements.

3.2 Spectrum Fitting Programs

There are several γ -ray peak-fitting programs. At the University of Kentucky, **FitPic V5.0** has been used for several years. It takes a spectrum, which is a histogram read from a data acquisition system, finds the peaks in the spectrum and determines their position, area, and corresponding statistical uncertainties. The fitting parameters were determined for the whole spectrum at once, which results in some restrictions in fitting complicated spectra. The excitation function and angular distribution data at $E_n=2.3$ MeV were analyzed with **FitPic**. **CNE** is another γ -ray spectrum analysis program [50], generally not used for fitting

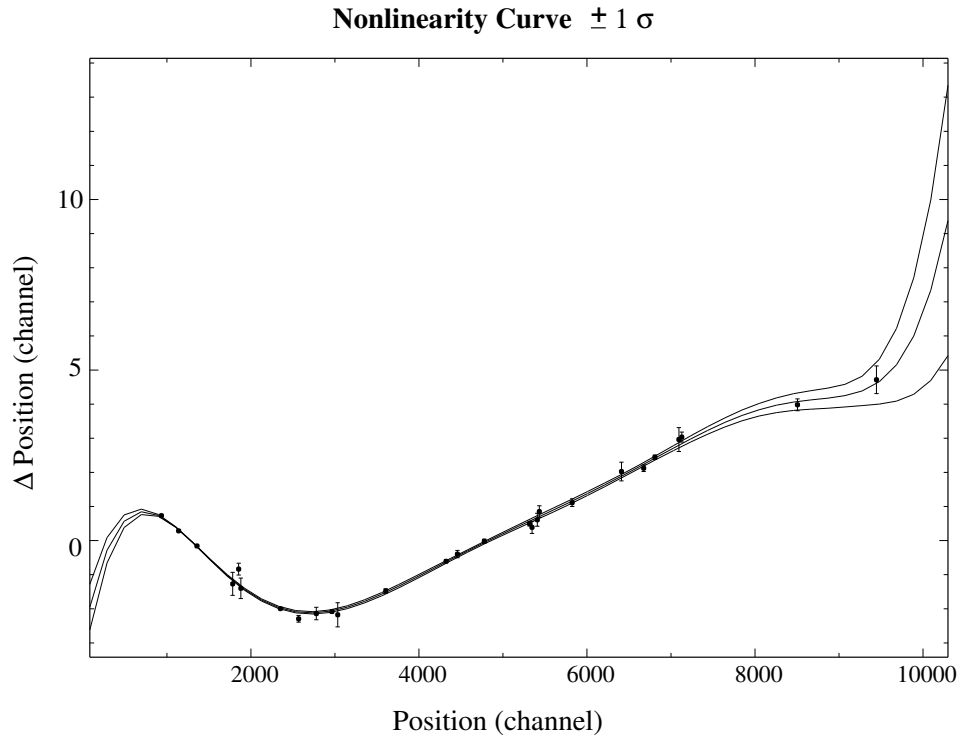


Figure 3.1: The nonlinearity curve for ^{94}Zr excitation function data. The upper and lower curves represent $\pm\sigma$ to the fitted curve.

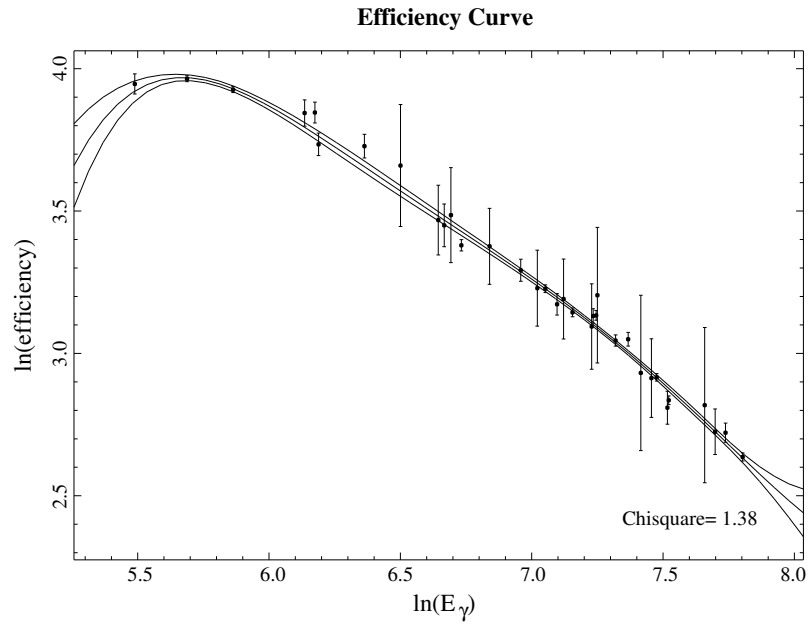


Figure 3.2: Efficiency curve for the HPGe detector used in $^{94}\text{Zr}(n,n'\gamma)$ excitation function measurements at the UK facility.

the peaks. It was mainly used for energy calibrations of the spectra to be fitted with `FitPic` or checking the spectra for any gain shifts, which may occur during long runs.

A more recent and widely used program is `Tv`, which was adapted in our lab with the help of Marcus Scheck, a postdoctoral scholar. The program was developed by Andreas Fitzler at the Institute for Nuclear Physics, University of Köln, Germany, 2000 [51]. `Tv` is more interactive and flexible than `FitPic`. It allows the user to define the fitting parameters based on the characteristics of any given peak in the spectrum, resulting in a more detailed data analysis. The angular distribution data at $E_n=2.8$ and 3.5 MeV were analyzed with `Tv`.

The user can define some specific peak characteristics, e.g., position, energy, yield, width and left tailing, and their corresponding statistical uncertainties. A knowledge of the role of some of these parameters is useful. In general, a Gaussian distribution is considered for fitting the shape of the γ -ray peaks. But, in reality, a γ -ray peak has a tail on the low-energy side of the peak. This left tailing can arise from imperfect charge collection in some regions of the detector or secondary electron and bremsstrahlung escape from the detector active volume [43]. The effect can be minimized by adjustment of the electronics (*pole zero*) and/or improvement of the HPGe detector’s electronic properties by “grilling”. Grilling a detector refers to exposure of the detector to very high intensity radiation from a radioactive source. Such standard procedures took place before the start of any measurements. The left tailing has an effect on the γ -ray peak shape; therefore, the centroid and the area under the peak can be affected. In `Tv`, like most other γ -ray peak-fitting programs, such corrections are considered. The user can define or adjust the width or left tailing parameters based on plots of the width vs. E_γ and left tailing vs E_γ , respectively; plots were obtained from the ^{226}Ra calibration spectrum. The analysis of complicated spectra benefits from such fine tuning in the peak-fitting procedures.

3.3 Excitation Functions

An excitation function is given by the γ -ray yield as a function of neutron bombarding energy. The threshold energy, E_x , for exciting the level from which the γ ray was emitted can be obtained from this plot. The shape of this plot can also be used to determine the spin of the excited level.

The ^{226}Ra source was employed for the preliminary energy calibrations. A few well-known and well-defined γ -ray peaks from ^{94}Zr were used for more accurate energy calibrations performed in CNE. Those peaks were 381.57(19), 550.88(10), 752.60(10), 918.74(5), 1232.55(19), 1411.4(6), 1447.41(19), and 1671.41(10) keV [34]. Also, additional peaks from the ^{94}Zr spectra were used as input to the `dsonlin` code, to account for the nonlinearity calibrations in the energy range not covered by the ^{226}Ra spectrum. Excitation function measurements were performed in two sets: $E_n = 2.5$ to 2.9 MeV and $E_n = 3.0$ to 4.0 MeV.

There was a substantial gain shift between two data sets, therefore, each data set was analyzed separately. For each data set, the fitted γ -ray peak parameters were sorted by the **efsort** code, where the normalizations, efficiency, and nonlinearity corrections were applied to the data. The γ -ray yields were normalized to an equal number of incident neutrons. The average value of the long counter scalar over the whole excitation function measurement, multiplied by 100, was used as the normalization factor. The order of magnitude does not affect the final results, but larger numbers are preferable, especially for angular distribution data analysis. Two output files obtained, *fname1.exf* and *fname2.exf*, and were used as inputs to the **exfplot** code, which provided plots of normalized yields for any γ ray vs. the bombarding neutron energy. The threshold of a given γ ray can be determined from these plots. For example, Figure 3.3(b) shows the excitation function for the 1236-keV transition. Its threshold is about 3 MeV, which is in agreement with the appearance of the peak in the spectra shown in Figure 3.3(a). Other sets of output were E_γ vs E_n plots. The accuracy of the energy calibration and application of the nonlinearity correction could be checked from these plots.

When the transitions from and to a level are known, the level's experimental yield, as a function of E_n , can be obtained from the excitation function data. The spin of the level can be determined from the comparison of the experimental yields to the theoretical values for any given J^π . The details of this analysis are described in Appendix E.

3.4 Angular Distributions

The compound nucleus mechanism governing the INS reaction at a lower neutron energies leads to an alignment of the excited nuclei, resulting in an anisotropic angular distribution of γ -rays emitted from the excited levels. The incident neutrons can be considered as plane waves with wave vector k along the incident direction, which is considered as the symmetry axis. The projections of the orbital angular momenta along the symmetry axis, m_l , is zero for incident neutrons, which bring to the compound system orbital angular momenta only in the $m_l = 0$ substate. This process provides enough angular momentum to excite the states with $J \leq 6$ in the target nucleus. Therefore, based on conservation of angular momentum, the population of the magnetic substates in the target nucleus, other than $m_j = 0$, depends solely on the spins of the projectile neutron and the target nucleus [52]. This population is symmetric about $m_j = 0$ and is regarded as alignment of the excited nucleus. The decay of the aligned states is then characteristic of the distribution in the population of the magnetic substates, the multipolarity of the radiation, and the spins of the initial and final states.

The angular distribution data analysis was based on the Sheldon and Van Patter approach for γ -ray angular distributions resulting from a compound system [53]. The angular

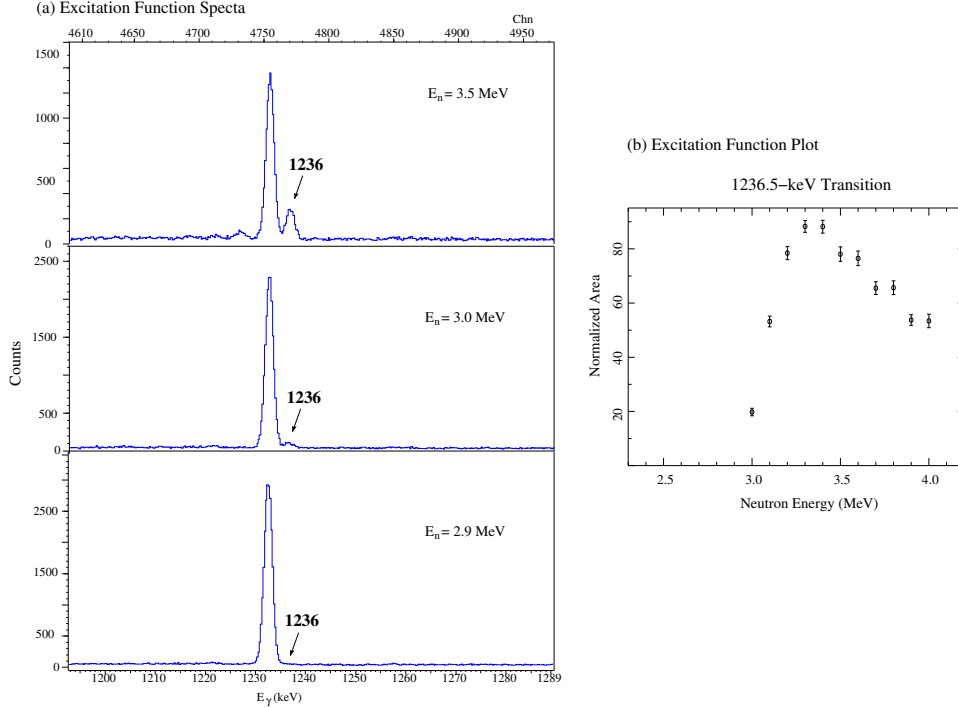


Figure 3.3: Examples of prompt γ -ray spectra from the ^{94}Zr excitation function measurements at different incident E_n (a). Note the appearance of 1236-keV peak as E_n increases. The output plot for the 1236-keV transition obtained by `explot` code (b), shows that the transition threshold is above 2.9 MeV.

distribution could be expressed as an expansion in even-order Legendre polynomials:

$$W(\theta) = \sum_{\nu} A_{\nu} P_{\nu}(\cos\theta), \quad (3.4.1)$$

where $\nu = 0, 2, 4, \dots$, limited by angular momentum coupling rules. ν is even due to parity conservation rules. The first three terms are usually included, and normalizing to A_0 gives:

$$W(\theta) = 1 + a_2 P_2(\cos\theta) + a_4 P_4(\cos\theta), \quad (3.4.2)$$

where a_2 and a_4 are experimental expansion coefficients to be determined from a least-squares fit to the data. The angular distribution is symmetric about an observation angle of 90° . This is a characteristic of a fully aligned excited nucleus, produced in inelastic neutron scattering. For a pure quadrupole transition, e.g., $2 \rightarrow 0$, $a_4 < 0$ and $a_2 > 0$ result in a minimum of $W(\theta)$ at 90° . A pure dipole transition, e.g., $1 \rightarrow 0$, $W(\theta)$ peaks at 90° . Examples of such angular distributions are shown in Figure 3.4. The shape of the angular distribution is closely related to ΔJ and the change in parity, which describe the transition multipolarity.

The energy calibrations for the angular distribution data were performed more carefully than for the excitation function data. The well-known γ rays from the ^{94}Zr spectrum [34],

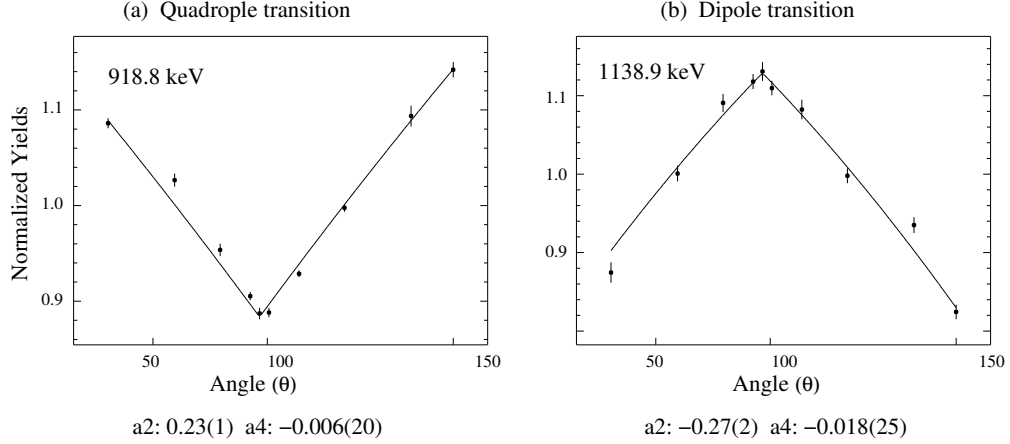


Figure 3.4: Examples of angular distribution plots of pure quadrupole ($2^+ \rightarrow 0^+$) and dipole ($3^- \rightarrow 2^+$) transitions.

381.57(19), 550.88(10), and 918.74(5) keV, were used for calibration in the low-energy region, 300 - 920 keV. The ^{24}Na γ rays of 1368.596(29) and 2753.849(40) keV, along with the $^1\text{H}(n,\gamma)^2\text{H}$ 2223.254(3)-keV peak were used for the high-energy region, 920-2800 keV. The peaks selected from ^{94}Zr were transitions from states with relatively long lifetimes, on the order of a few ps to ns, thus providing an unshifted peak in the spectrum and suitable for energy calibrations.

The fitted γ -ray peak parameters were sorted by the **adsort** code, where the normalizations and nonlinearity corrections were applied to the yields and peak centroids, respectively. The normalization of the angular distribution was a more delicate process. The long counter scalar value at each angle was normalized to the value at the 55° angle; the $P_2(\theta = 55^\circ) \rightarrow 0$ and P_4 is too small to contribute in the angular distribution. This procedure was used as a primary normalization. Fine tuning was employed by the use of the corrected yields of a transition with an isotropic angular distribution, e.g., a $0^+ \rightarrow 2^+$ γ -ray transition. In ^{94}Zr , the 381-keV γ -ray, $0_2^+ \rightarrow 2_1^+$ transition, was used. The latter step was also taken when forward monitor spectra were used for normalization purposes. The use of long counter scalar values and the yields in the forward monitor spectra resulted in the same outcome. For consistency, the long counter scalar values were used for yield normalization of the angular distribution data. The only data set which was not included in the analysis was the angular distribution data at 116° at $E_n = 2.8$ MeV. This elimination was due to an inconsistency with respect to the other data points, after the final normalization of the γ -ray yields.

The source of emitted γ rays, the scattering sample, is not a point source. Therefore, multiple scattering of the incident neutrons and photoabsorption of the γ rays in the scattering sample can obscure proper counting of yields. The yields should be corrected for neutron attenuation, multiple scattering, and γ -ray attenuation in the scattering sample. The correc-

tions were calculated for each incident neutron energy with the **gambit** code, Appendix D. The experimental expansion coefficients, a_2 's and a_4 's, were obtained by a least-squares polynomial fit to the experimental differential cross sections using the **adlegpol** code. The experimental yields, in arbitrary units, vs. $\cos^2\theta$ were plotted, from which the quality of the polynomial fit could be examined. By including the theoretical calculations of the angular distributions at a given E_n , along with a tentative level scheme which covers the levels up to E_n , as inputs to **adlegpol**, multipole mixing ratios and branching ratios were determined. The tentative level scheme, *fname.dec*, was obtained by the **levener** code. The multipole mixing ratio (δ) was obtained from the comparison of the experimental data with the theoretical calculations given by a modified version of the code **CINDY**. This theoretical model is based on a statistical compound nucleus theory of Hauser-Feshbach-Moldauer [54], using an optical model potential.

The optical potential dependency on the incident neutron energy, E_n , was expressed as $V = V_0 + V'_0 E_n + V''_0 E_n^2$ for the real part and $W = W_0 + W'_0 E_n + W''_0 E_n^2$ for the imaginary part. The parameters used were: $V_0 = 47$ MeV, $V'_0 = -0.27$ (MeV) $^{-1}$, and $W_0 = 9.00$ MeV, $W'_0 = 0$ (MeV) $^{-1}$. The second order parameters, V''_0 and W''_0 were zero. The radius and diffusion parameters were: $r_0 = 1.215$ fm, $a = 0.658$ fm, $r'_0 = 1.264$ fm, and $a'_0 = 0.524$ fm. The spin-orbit potential, V_{so} , is a function of incident neutron energy, E_n , through Eqn. 3.4.3, with parameters, $v_{so1} = 6.2$ MeV, $v_{so2} = 0.004$ (MeV) $^{-1}$, and $E_f = -7.34$ MeV. The same parameters were used as input for the excitation function **CINDY** calculations; see Appendix E. The input file description can be found in Ref. [54]. From these comparisons a plot of χ^2 vs. δ was obtained.

$$V_{so} = v_{so1} \exp(-v_{so2}(E_n - E_f)) \quad (3.4.3)$$

An example of the angular distribution plot and corresponding a_4 vs a_2 and χ^2 vs. δ plots are shown in Figure 3.5. The ellipse in the a_4 vs a_2 plot represents the experimental coefficient values. The crossing lines are part of the theoretical ellipse, where the closeness of these two ellipses is represented in the χ^2 vs. δ plot. Therefore, the lower χ^2 value usually corresponds to the spin assignments and also the corresponding multipole mixing ratio.

3.5 Lifetime Measurements

From the angular distribution measurements the lifetimes of the excited levels are deduced by the Doppler-shift attenuation method (DSAM) [55]. Following inelastic neutron scattering, the nucleus recoils in the viscous medium of electrons and nuclei and the γ rays produced experience an attenuated Doppler-shift. Although the recoil velocity for heavy nuclei is usually small ($\frac{v}{c} \approx 0.001$), it is sufficient to produce a measurable Doppler shift, and lifetimes of excited levels in the range of a 10^{-15} - 10^{-12} seconds can be measured.

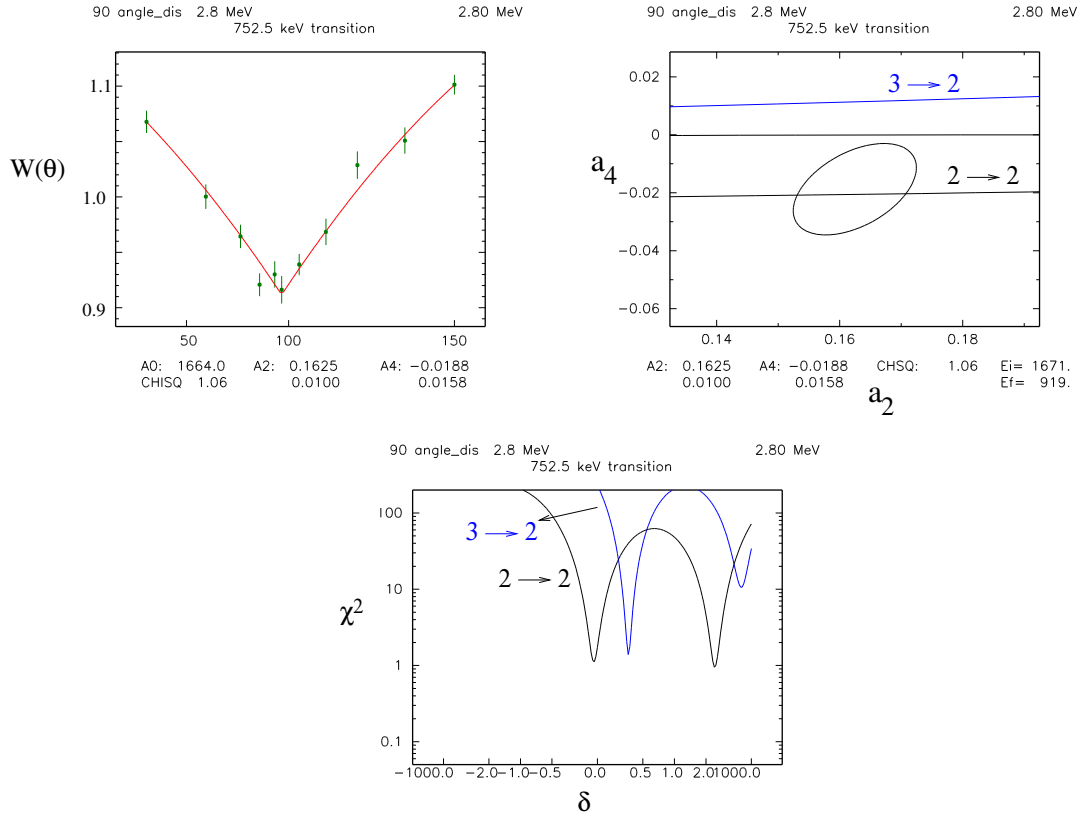


Figure 3.5: Example of angular distribution output plots for 752-keV γ -ray transition, with a least-squares Legendre polynomial fit to the experimental data, along with the corresponding a_4 vs a_2 and χ^2 vs δ plots. The data are from the angular distribution at $E_n=2.8$ MeV.

Figure 3.6 is an example of Doppler shifts for the emitted γ ray at 2648.4 keV. No Doppler broadening was observed in the spectra.

If $E_{\gamma 0}$ is the energy of a γ ray emitted by the nucleus at rest, the energy of the Doppler-shifted γ ray as a function of the observation angle, $E_{\gamma}(\theta_{\gamma})$, is given by:

$$E_{\gamma}(\theta_{\gamma}) = E_{\gamma 0} \left[1 + \frac{v_{cm}}{c} F_{exp}(\tau) \cos \theta_{\gamma} \right] \quad (3.5.1)$$

where v_{cm} is the initial velocity of the center-of-mass of the recoiling excited nucleus and the outgoing neutron in the laboratory frame. From the kinematics of the reaction, $\beta = \frac{v_{cm}}{c}$ is related to the nucleus and neutron masses, and incident neutron energy in MeV, given by Eqn. 3.5.2 [55].

$$\beta (= \frac{v_{cm}}{c}) = 0.04635 \frac{A_n}{A_n + A_A} \sqrt{\frac{E_n}{A_n}} \quad (3.5.2)$$

$F_{exp}(\tau)$, the experimental attenuation factor is related to the stopping process of the residual nucleus in the scattering sample as described by Blaugrund [56], in which an average

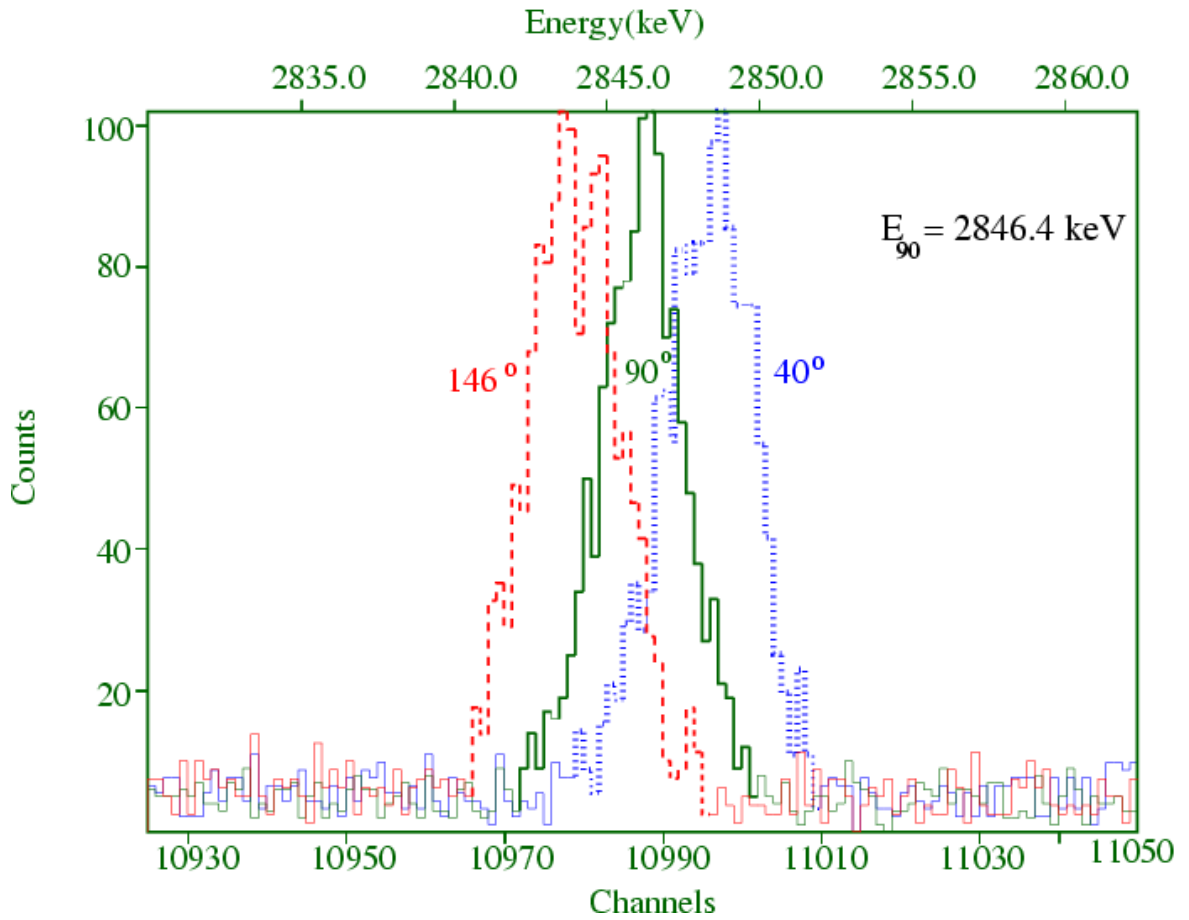


Figure 3.6: Example of Doppler shifts in the γ -ray spectra at different angles. The Doppler shift is toward higher energy at forward angles and lower energies at backward angles with respect to 90° . Data are taken from the ^{94}Zr angular distribution measurement at $E_n = 3.5$ MeV.

recoil velocity for the residual nucleus in all directions was included. The plot of E_γ vs. $\cos \theta$ for the 752-keV transition is shown in Figure 3.7(a), where the slope is related to $F_{exp}(\tau)$ such that $slope = E_{\gamma 0} \beta F_{exp}(\tau)$. The $F_{exp}(\tau)$ is then compared with the theoretical value calculated with the Winterbon formalism [57]. From this comparison a mean lifetime, τ , is determined, as shown in Figure 3.7(b).

The details of the DSAM method employed at the University of Kentucky are discussed by Belgya *et al.* [55]. The geometry of the scattering sample and the closeness of the neutron bombarding energy to the threshold of a level of interest were the main factors included in the formalism of the **v1pgm** code to calculate the theoretical attenuation factors, $F(\tau)$. The input file to **v1pgm** contains information on the scattering sample characteristics and incident neutron energy [45].

The fitted γ -ray peak parameters, from angular distribution spectra, were sorted by the **dssort** code, where the nonlinearity corrections were applied to the peak centroids. The output file, *fname.dls*, contains energy, centroid, and observation angles for each transition. A computer code, **ftauplt**, provided the E_γ vs. $\cos(\theta)$ plots and an output file, *fname.tau*, which contains $F_{exp}(\tau)$ and corresponding τ for each γ -ray transition. The averaged values, $\overline{F}_{exp}(\tau)$, and lifetimes of the levels were obtained when a level scheme file, *fname.dec*, was provided as input to the code. These data were listed in the *fname.tau* file.

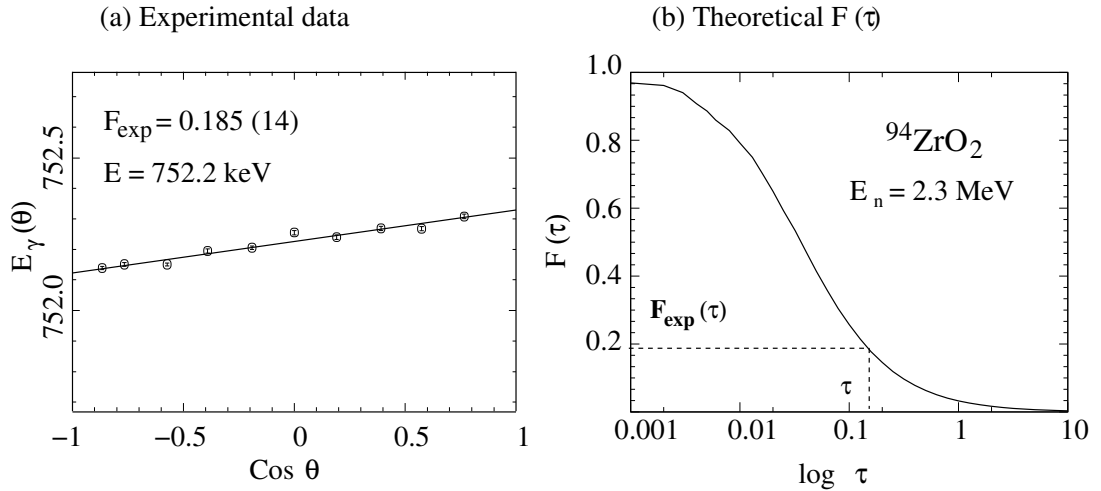


Figure 3.7: Plot of E_γ vs. $\cos \theta$ for the 752-keV γ -ray transition and the calculated theoretical $F(\tau)$ vs. τ for ^{94}Zr at $E_n = 2.3$ MeV. The lifetime of the level at 1671.4 keV, from which 752 keV decays, is $\tau = 185_{-12}^{+13}$ fs.

3.6 Reduced Transition Probabilities

In electromagnetic transitions, parity and total angular momentum are conserved. If the spin and parity of the initial state is J_i^π and that of the final state is J_f^π , conservation of

the total angular momentum gives a simple rule on the photon multipolarity, L :

$$|J_i - J_f| \leq L \leq J_i + J_f \quad (3.6.1)$$

The emitted radiation is described by the vector field [58] and it changes sign under coordinate inversion. Therefore, the photons of multipolarity L can be electric radiation, with parity $\pi_E = (-1)^L$, or magnetic radiation, with parity $\pi_M = (-1)^{L+1}$. The parity conservation, $\pi_i \pi_f \pi_\gamma = 1$ [58], thus, gives:

$$\begin{aligned} \pi_i \pi_f &= (-1)^L && \text{for electric radiation} \\ \pi_i \pi_f &= (-1)^{L+1} && \text{for magnetic radiation} \end{aligned}$$

Table 3.1: Multipolarity of the lowest order in transitions based on ΔJ and change in parity selection rules.

Pure Multipolarity	ΔJ	Change in Parity
E1	1	Yes
M1	1	No
E2	2	No
M2	2	Yes
E3	3	Yes

The parity conservation and angular momentum selection rule, $\Delta J = L$, can be summarized in Table 3.1. Only the multiplicities of lowest order are included. The reduced transition probability, $B(\pi l)$ is related to the nondiagonal matrix element of the operator $\hat{T}(\pi l)$ through:

$$\begin{aligned} B(\pi L; J_i \rightarrow J_f) &= \sum_M |\langle J_f M_f | \hat{\mathbf{T}}(\pi \mathbf{L}, \mathbf{M}) | J_i M_i \rangle|^2, \\ &= \frac{1}{2J_i + 1} |\langle J_f || \hat{\mathbf{T}}(\pi \mathbf{1}) || J_i \rangle|^2 \end{aligned} \quad (3.6.2)$$

where in $\hat{T}(\pi l)$, π refers to parity of the transition, electric or magnetic, and L is the order of multipolarity, $L = 1$ for *dipole*, $L = 2$ for *quadrupole*, $L = 3$ for *octupole*, etc. Therefore, transitions can be $E1$, $M1$, $E2$, etc. as mentioned above.

There are transitions which have mixed multiplicities. For example, a $(2^+ \rightarrow 2^+)$ transition, in which $\Delta J^\pi = 0$ and parity does not change, both $E2$ and $M1$ multiplicities are allowed; there is no $M0$ transition. The reduced transition probabilities are then determined from the multipole mixing ratio, δ , which is defined by Eq. 3.6.3. It is a ratio of the $L+1$ multipolarity to that of L . The probability of higher multipole electric and magnetic transition decreases as the order of multipolarity increases. Therefore a $3^- \rightarrow 2^+$ transition is dominated by $E1$, even though it can be a mixed transition of $E1$ and $M2$ character.

$$\delta = \frac{\langle J_f || L + 1 || J_i \rangle}{\langle J_f || L || J_i \rangle} \quad (3.6.3)$$

A computer code, **transnuclear.pl**, was used to obtain the reduced transition probabilities, $B(\pi L)$ values for each transition. The γ -ray energy ($E_\gamma(\text{keV})$), lifetime of the level in ps (τ), multipole mixing ratio value (δ), and branching ratios (BR) of the transitions decaying from the level were used as the input parameters to the code. For $E_\gamma < 600$ keV, the total internal conversion corrections were applied by including the total conversion coefficients, α_e [60]. The code is written in *perl* and **perl -w transnuclear.pl** compiles the code. The $B(E2)$ and $B(M1)$ values are usually expressed in W.u., Weisskopf units, and μ_N^2 respectively, which are related to the single-particle reduced transition probabilities, $B(\pi L)_{s.p.}$, according to the Weisskopf approximation [Refs. [4] and [58]], by :

$$W_E(L) = B(EL)_{s.p.} = \frac{1}{4\pi} \left(\frac{3}{3+L} \right)^2 R^{2L} e^2 (fm)^{2L}, \quad (3.6.4)$$

$$W_M(L) = B(ML)_{s.p.} = \frac{10}{\pi} \left(\frac{3}{3+L} \right)^2 R^{2L-2} \times \left(\frac{e\hbar}{2M_p c} \right)^2 (fm)^{2L-2} \quad (3.6.5)$$

where $R = 1.2 A^{1/3}$ is the nuclear radius in fm. Therefore, $B(E2)(\text{W.u.}) = 0.0594 \times A^{4/3} e^2 fm^4$. For ^{94}Zr , $B(E2)(\text{W.u.}) = 25.39 e^2 fm^4$. $B(E2)$ is also expressed in $e^2 b^2$, $1 \text{ barn} = 10^{-24} cm^2$: $B(E2)(\text{W.u.}) = 25.39 \times 10^{-4} e^2 b^2$. $B(M1)$ is independent of nuclear mass, A , and therefore, is expressed in μ_N^2 .

$B(E2)$ and $B(M1)$ can be calculated by the following formule:

$$B(E2)(W.u) = \frac{9.527 \times 10^6 \times BR \times \delta^2}{E_\gamma^5 \times A^{4/3} \times t_{1/2} \times (1 + \alpha_e) \times (1 + \delta^2)}, \quad (3.6.6)$$

$$B(M1)(\mu_N^2) = \frac{0.3939 \times 10^2 \times BR}{E_\gamma^3 \times t_{1/2} \times (1 + \alpha_e) \times (1 + \delta^2)} \quad (3.6.7)$$

where the E_γ is in MeV and $t_{1/2}$ in fs.

3.7 $\gamma\gamma$ Coincidences

As mentioned in Section 2.3, the $\gamma\gamma$ coincidence experiments were the first performed at the TUNL facility. The analysis of these data was a challenge, since no one had dealt with such data previously. The data analysis procedures are discussed in this section.

The analysis of coincidence data of two-fold multiplicity (or $\gamma\gamma$ coincidences) first involves building a *matrix* of the detected γ rays. For triple coincidences, a *cube* should be built, but will not be discussed as such events in our data are rare.

Figure 3.8 shows a simple example of how the coincidence technique in 2-fold multiplicity works. A two-dimensional symmetric matrix, E_γ vs. E_γ , is built based on the coincidence events between any two quadrants. The two axes of the symmetric matrix correspond to $E1$ and $E2$ in keV. For each coincident event of $(E1, E2)$ on the matrix, there is another point, $(E2, E1)$. The recorded events and their corresponding positions on the matrix are shown

in Figure 3.8(a). For example for 550 and 918 keV in *evt 1*, the two points on the matrix are (550,918) and (918,550). The positions of these points are symmetric with respect to the matrix diagonal, the dashed line in Figure 3.8(a). A projection on X (or Y) will be a spectrum, in which the counts at each E_γ correspond to the total number of events recorded in coincidence with that γ ray, Figure 3.8(b). If the matrix is gated on a specific E_γ , e.g., 918 keV, it results in the spectrum shown in Figure 3.8(c) top panel, which contains 381-550-, 658- and 752-keV γ rays; they are in coincidence with the 918-keV γ ray. A gate on 381 keV is a spectrum which only contains 918-keV γ rays, as shown in Figure 3.8(c), the bottom panel. A decay scheme, shown in Figure 3.8(d), can be constructed based on the spectra obtained from gating on different γ rays.

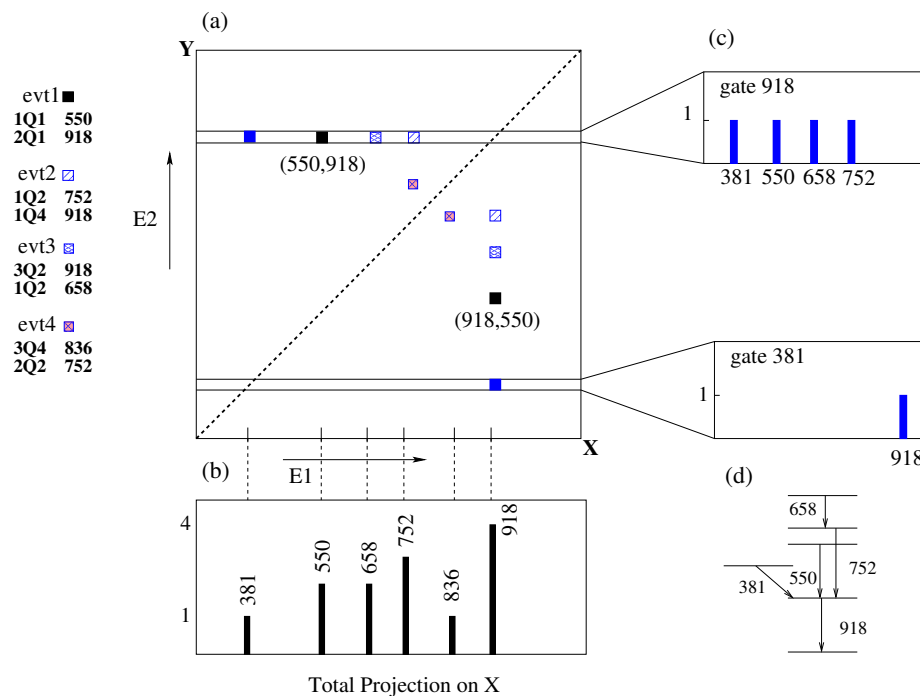


Figure 3.8: Schematic of coincidence technique. The matrix in (a) is a simple symmetric matrix, which is built from the coincidence data, e.g., *evt1*, *evt2*, *etc.* The Projection on X (b), the spectra from gates on 918- and 381-keV γ rays (c) are shown. A partial level scheme of ^{94}Zr (d) was built with the help of the coincidence data.

Building a matrix, creating X and Y projections, and gating on a specific E_γ , shown in Figure 3.8, is performed using different computer codes. In the ^{94}Zr coincidence data analysis, a *.tcl* script, *spectcl_uk.tcl*, was used in **SpectC1** to build a matrix; see Appendix F.4. The **matproj** code was used to create X and Y projection spectra; Figure 3.9 shows the X projection of the ^{94}Zr coincidence data. **Tv** was used to create the gated spectra. For example, Figure 3.10 shows the spectrum gated on the 918-keV γ ray.

3.7.1 Building a Matrix, using a SpecTcl .tcl script

The recorded raw data were in the NSCL (National Superconducting Cyclotron Laboratory) format, with extension *.evt*. The parameters recorded as raw data, time and energy signals for each quadrant, coincidence time between any 2 clovers, and BGO-shield time for each clover were defined in the *94Zrhardware.tcl* script; see Appendix F.5. The code *spectcl_uk.tcl* was used to replay the data, and also contains software to unpack and read out the raw data according to the data acquisition modules. The details of each process is described in the *spectcl_uk.tcl* script in Appendix F.4. The output histograms were defined based on the *SpecTcl User Guide* [47]. The main steps taken to build a matrix for ^{94}Zr coincidence data in *spectcl_uk.tcl* were:

1. Setup of the parameter pairs to create a histogram of a matrix type,
2. Application of an energy calibration to the energy parameters,
3. Definition of the histogram to create a symmetric matrix,
4. Definition of the time gates based on time constraints need to be applied to the matrix, and
5. Application of the final gate to the defined matrix.

Each part is discussed in more detail. Further information can be found in the *SpecTcl User Guide* [47].

1. A definition for a histogram created with a pairs of parameters was set up by:

```
set ghisto {}
foreach pair $pairs {
    set x [lindex $pair 0]
    set y [lindex $pair 1]
    set res [lindex $pair 2]
    spectrum $x-vs-$y g2 "$x $y" "$res $res"
```

The last line determines the type of output: `spectrum` for a histogram, `x-vs-y` is the name, and `g2` is the type of the defined histogram. The parameter entries are in order of `x`, `y` and their resolutions. Other histogram types are `sum`, 1- or 2-dimension histograms; their definition and parameters selections are explained in Ref. [47].

2. The energy calibration was applied to the energy parameters using standard radioactive sources. In the ^{22}Na spectra, the 1274.53-keV γ ray, along with the annihilation radiation at 511 keV, were used for a two-point energy calibration of each quadrant's energy parameters. In NQ# notation, N is the clover number and # the quadrant number. Therefore, the new energy parameters can be created and called NQ#_cal.

```
fit -create linear 1Q1_CALIB
fit -add 1Q1_CALIB {609.25 511} {1344.19 1274.53}
fit -perform 1Q1_CALIB
```



```
calibparam -create 1Q1_cal 101 1Q1 1Q1_CALIB keV
```

For each quadrant these lines were repeated.

3. To create a matrix, a histogram of type `g2` was defined, which can take more than two parameters. All the `NQ#.cal` parameters; 3 clovers with 4 quadrants, a total of 12 parameters were used to define the matrix **ALL**:

```
spectrum ALL g2 {1Q1_cal 1Q2_cal ... 2Q1_cal ... 3Q4_cal} {11,11}.
```

The number of channels is determined by 2^n , where n defines the resolution. The spectra of type 1 can be created with resolution $n = 12$ with $2^{12} = 4096$ channels. Using the same resolution for matrix **ALL** resulted in an error, the software could not **allocate** the spectrum. The parameters in `g2` spectrum are type *long* or 4 bytes. Therefore, the matrix **ALL** would have $4k \times 4k \times 4$ bytes. The error was created, because the maximum *DisplayMegabytes*, given in the *SpecTclInt.tcl* file was **20 MB**. The matrix of $4k \times 4k = 84$ MB was too large for the software to handle. In order to overcome this issue, resolution was given as: `{0.0 8191.0 2048} {0.0 8191.0 2048}`, thus a matrix of x vs. y with 8192 channels was compressed in 2048 channels.

The coincidence experiment was performed with 5-MeV neutrons, a spectrum up to about 4.3 MeV was produced by using this resolution. Other resolutions used were `{11 11}`, which created a spectrum up to about 1900 keV. A resolution of `{0.0 4095.0 2048} {0.0 4095.0 2048}`, which compressed the spectrum of 4096 into 2048 channels, created a spectrum up to 4 MeV.

4. A spectrum is not created until a **gate** has been applied. The *primitive* and/or *complex* gates for application of time constraints on the energy spectra were defined based on their uses, according to the *SpecTcl User's Guide* [47]. A *primitive* gate of type **s** (for slice) for any of the quadrant time parameters, `NQ#T` (T for time), defines the time window in which the quadrant has recorded events in coincidence. These gates were named `QIDN#`, (ID for identification). For example, `QID11` defines the ID time for `1Q1`, quadrant 1 in clover 1. The time in `{}` were chosen based on the `1Q1T` spectrum, shown in Figure 3.13:

```
gate QID11 s {1Q1T {783 1483}}
```

The time calibration of the TDC module was 0.15 ns/ch. Therefore the ID time windows are about 100 ns. This is the time that a coincident event has been recorded in one quadrant. In the same manner, `COINIDN_N` primitive gates were defined for the coincidence between any two clovers (`COIN` for coincidence). The shield ID time gates were defined for each quadrant separately, for example:

```
gate COINID1_1 s {COIN11 {1 4000}}
gate SHIELD11_COIN s {1SHIELDT {1900 2700}}
```

where the first line is for clover 1 in coincidence with clover 1, and the next line describes the coincidence time between the shield and quadrant 1 in clover 1.

Complex gates were defined by logic combinations of the primitive gates, using AND (*), OR (+), and NOT (-). For example, the complex gate of SHIELD11_NOVETO defines the time window in which the shield and quadrant 1 in clover 1 were **NOT** overlapping. This provides a *veto* on the signals from the shield if it is in coincidence with a signal from any quadrant in that clover. The name SHIELD11_NOVETO might be misleading, but it actually refers to the time window in which the shield has not been fired at all.

```
gate SHIELD11_NOVETO - {SHIELD11_COIN}
```

The coincidence time for quadrant 1 in clover 1 is the time overlapped in QID11 AND COINID1_i gates given by:

```
gate COINID11_1 * {QID11 COINID1_1}
gate COINID11_2 * {QID11 COINID1_2}
gate COINID11_3 * {QID11 COINID1_3}
```

The same conditions were applied for all other quadrants. It provides a coincidence time window of about 30-50 ns. The VCOINID11_1 gate, V for shield-vetoed signals, was defined as the overlap between COINID11_1 AND SHIELD11_NOVETO gates:

```
gate VCOINID11_1 * {COINID11_1 SHIELD11_NOVETO}
gate VCOINID11_2 * {COINID11_2 SHIELD11_NOVETO}
gate VCOINID11_3 * {COINID11_3 SHIELD11_NOVETO}.
```

Gates with the same conditions were defined for all the other quadrants in clover 1, as well as for clovers 2 and 3. The final coincidence gates between any two clovers were defined by combining the above mentioned gates. For example, the following shows the final gates for clover 1 only. The same is applied to clovers 2 and 3.

```
gate VDET1_1 + {VCOINID11_1 VCOINID12_1 VCOINID13_1 VCOINID14_1}
gate VDET2_1 + {VCOINID21_1 VCOINID22_1 VCOINID23_1 VCOINID24_1}
gate VDET3_1 + {VCOINID31_1 VCOINID32_1 VCOINID33_1 VCOINID34_1}
```

Since there are repetitive permutations, e.g., DET1-2 and DET2-1, the gates were combined as follows:

```
gate VCF1_2 + {VDET1_2 VDET2_1}
gate VCF1_3 + {VDET1_3 VDET3_1}
gate VCF2_3 + {VDET2_3 VDET3_2}
gate VALL + {VCF1_2 VCF1_3 VCF2_3}.
```

5. The gate `VALL` as the final combination of all gates, was applied to spectrum `ALL` and the matrix was built:

```
apply VALL ALL
```

As it follows from the final *gate* definition, the matrix `ALL` contains the total counts of the coincident events between any two quadrants.

3.7.2 Creating Projection and Gated Spectra

The matrix built in `SpecTc1` could be written in the NSCL *ASCII* or *BINARY* formats. Further analysis of the matrix in those formats was not possible, since no programs were available. Dirk Weisshaar from NSCL/MSU incorporated the line-compressed format of `Tv` to the `SpecTc1` *swrite* command. With his help, the `Tv` format was included in the `SpecTc1` version used. The details of this procedure are discussed in Appendix F.

A symmetric matrix was built, and *X* and *Y* projection spectra were created by the `matproj` code from the `mattool.c` code. Figure 3.9 shows an *X*-projection spectrum obtained from ^{94}Zr coincidence data. The *X*-projection spectrum was used in `Tv` to create a *cut*, i.e., a gate on a specific γ -ray energy, corresponding to a transition in a cascade. The schematics of such spectra are shown in Figure 3.8(c), and Figure 3.10 shows a *cut* spectrum from the data, i.e., gated on the 918-keV, $2_1^+ \rightarrow 0_1^+$ transition in ^{94}Zr . The gated spectrum was created in `Tv`, by selecting channels on either side of the 918 γ photopeak. The same number of channels was marked on the background to create the *cut* spectrum. Usually, for a better outcome, the marked region should not be too wide. More details of using `Tv` for coincidence analysis can be found in Appendix F and the *Tv Manual* [51].

3.8 Coincidence measurements at the UK facility, A Comparison

A comparison of the coincidence measurements and data analysis at the UK facility versus TUNL was performed for future reference. At the University of Kentucky facility, coincidence measurements are performed using **KEGS**, **K**entucky **G**amma-ray **S**pectrometer, Figure 3.11. The principles of the coincidence experimental setup and data acquisition are discussed by McGrath et al. [41].

The data on $^{106}\text{Pd}(n,n'\gamma\gamma)$ coincidence measurements, performed at the UK facility, was available for analysis. The measurement was carried out at $E_n = 3.5$ MeV for a total of ~ 150 hours. Monoenergetic neutrons were produced through the $^3\text{H}(p,n)^3\text{He}$ reaction with a pulsed beam of protons from the electrostatic accelerator. The neutrons produced at the gas cell were collimated by a Li_2CO_3 -loaded paraffin shield [59]. The scattering sample of 19.9813 grams of palladium metal powder, 98.5% enriched in ^{106}Pd , in a cylindrical vessel of 1.8-cm diameter and 3.5-cm long was suspended about one meter from the gas

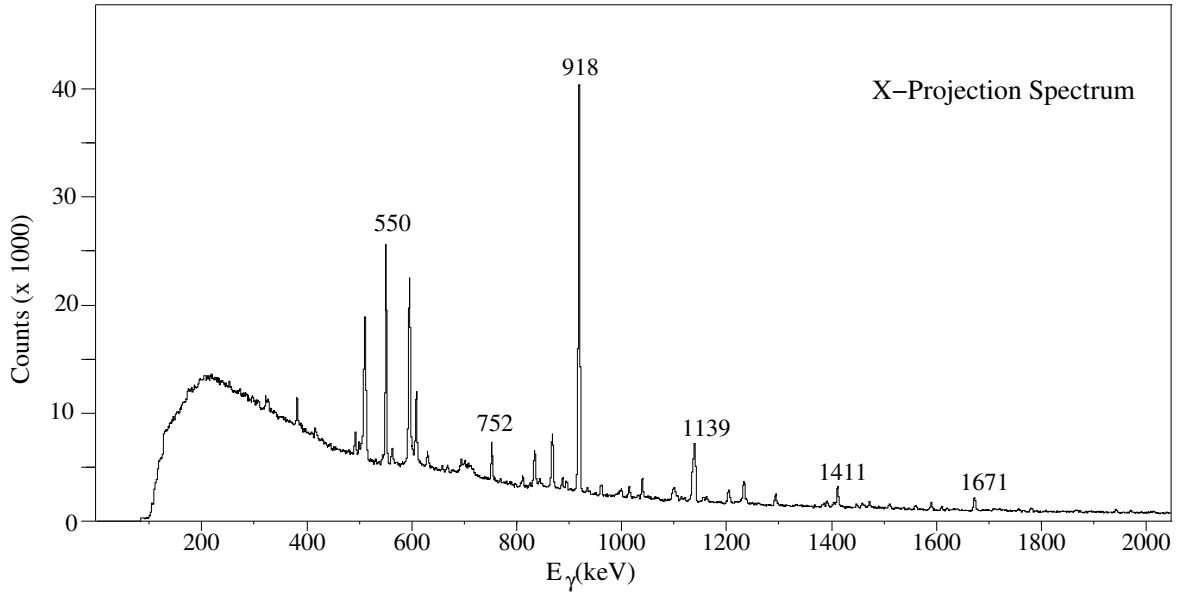


Figure 3.9: The total projection of the matrix ALL in the X direction, or the X-projection spectrum, of the coincidence data for ^{94}Zr . The matrix ALL was obtained by SpectCl software.

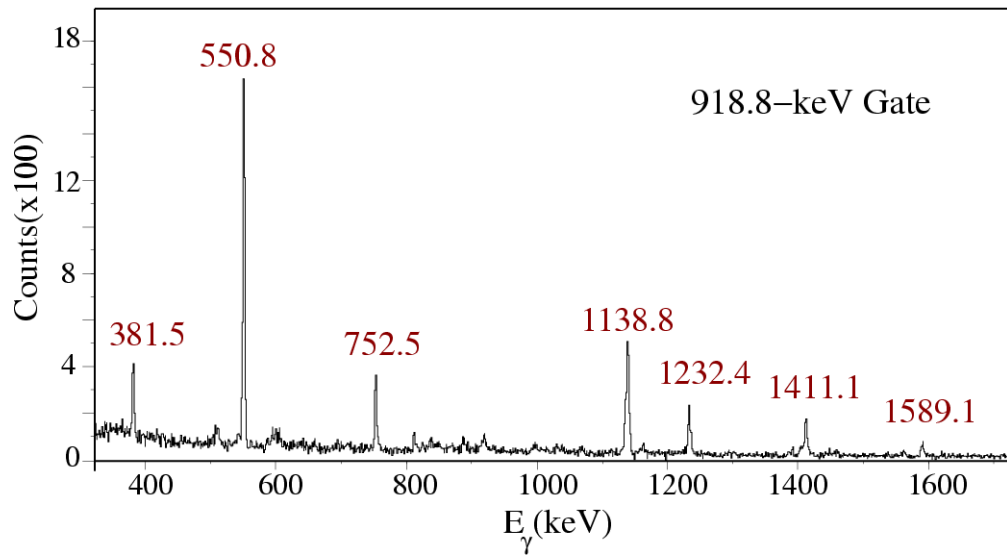


Figure 3.10: Spectrum gated on the 918-keV γ ray, the $2_1^+ \rightarrow 0_1^+$ transition, obtained from the ^{94}Zr coincidence data.

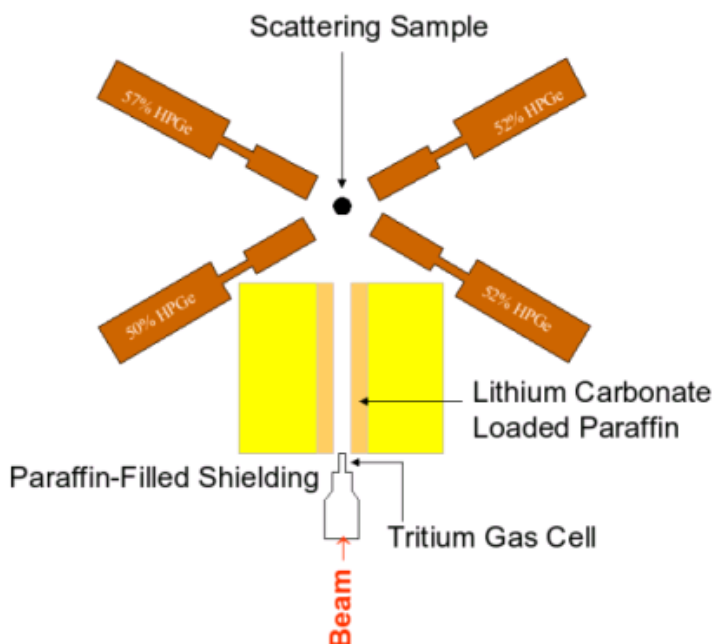


Figure 3.11: KEYS, KEntucky Gamma-Spectrometer, the experimental setup for coincidence measurements at the UK facility. In the physical setup the detectors are in the plane perpendicular to the page.

cell. An array of four HPGe detectors were assembled in an X-shape geometry for γ -ray detection, shown in Figure 3.11. Each detector was at approximately 5 cm from the scattering sample, and the assembly of detectors was in a plane perpendicular to the beam direction. Details on the experimental setup and data acquisition can be found in the *UK Experiment Manual* [44]. The UK coincidence data were recorded for a multiplicity of two (coincidence events between any two detectors) in the University of Kentucky *.emr* format, or in the University of Fribourg format [50].

3.8.1 Coincidence Time Requirements

In the UK coincidence measurements, a typical time window of 100 ns between any two detectors was set up in the electronics to record the coincident events. The time spectrum of the coincident events, shown in Figure 3.12, was used for more stringent time requirements in building a matrix. The width of the peak in a time spectrum corresponds to time-correlated events from the scattering sample detected in the corresponding detector. For example, the peak in the time spectrum for HPGe detector 1 shown in Figure 3.12 has a width of 75 channels (0.13 ns/Chn) $\approx 10 \text{ ns}$. The time width for every detector may not be exactly 10 ns. The pulsed beam used in the measurement was used as a time reference in each detector. In another words, all clocks in the HPGe detectors start and stop based on the pulsed beam duration, 533 ns. On the other hand, in the TUNL coincidence measurements, there was

no such universal time reference, since a DC beam was used. Therefore, an arbitrary time reference was chosen. The detection in quadrant1 in clover1 was used as a time reference for time signals in the other quadrants. A wide window of 800 channels (0.15 ns/Chn) $\approx 120 \text{ ns}$ defined the coincidence ID time for each quadrant, as seen in Figure 3.13. It is the time interval in which a coincidence event was recorded in that quadrant. The final constraint on the coincidences was applied by considering the coincidence times between any two clovers. This constrain would result in a time interval of $\approx 30\text{-}40 \text{ ns}$. The definitions of such time *gates* have already been discussed in the previous section.

The time resolution values (ns/Chn) are determined as follows: in the UK measurements, 533 ns of the beam duration divided by 4000 channels in the *TDC* module gives 0.13 ns/Chn , whereas in the TUNL measurements, $600 \text{ ns}/4000 \text{ channels} = 0.15 \text{ ns/Chn}$.

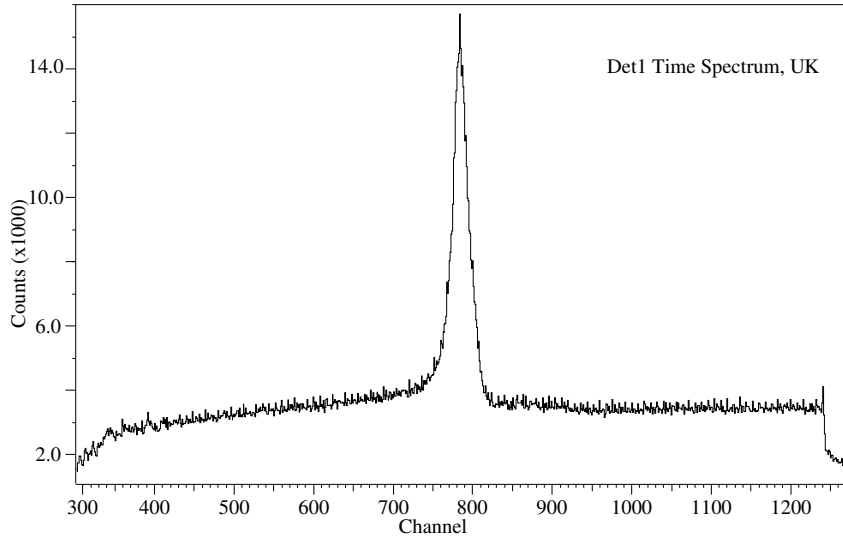


Figure 3.12: Example of a time spectrum from ^{106}Pd coincidence data at UK. The counts show the numbers of events recorded in a detector. The spectrum is only for one run of 8 hours. The width of the peak determines the stringent time requirements for building a matrix; time resolution is 0.13 ns/Chn .

3.8.2 The UK Coincidence Data Analysis

A computer code **cmt5** was used to read out and sort the data in either *projection* or *matrix* mode. The instructions on creating the projections and building the matrix are documented by Nigel Warr in Ref. [50]. Further data analysis instructions are given in Appendix G.

The spectra for each parameter, energy and time, for each detector were produced by **cmt5**, executed in the *projection* mode. The *fname_cmt.inp* file used as input to the code contains raw data and other specifications for the *projection* mode. The limits on the coincidence time window for each detector were determined from the time spectra. The energy calibration

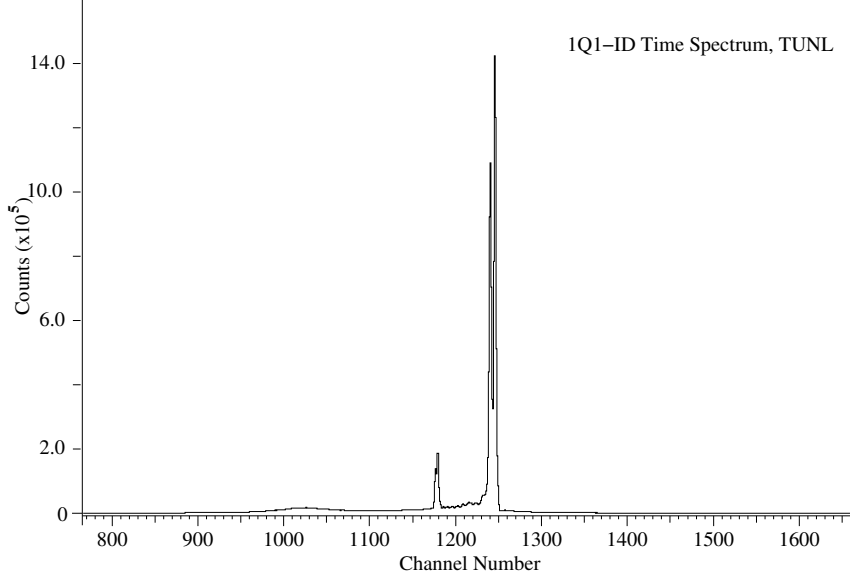


Figure 3.13: Example of a time spectrum from ^{94}Zr coincidence data at TUNL, for quadrant 1 in clover 1. The counts show the number of events recorded in a that quadrant for the whole experiment, a total of 105 hours. The stringent time requirements for building a matrix are explained in the text; time resolution is 0.15 ns/Chn.

coefficients were determined from the energy spectra. This information is from the work by Monica Mynk, a former graduate student.

The **cmt5** code in *matrix* mode was run with the new time limits and energy calibrations incorporated into the input file, *fname_mat.inp*. Further analysis was performed using the **RadWare** package [61]. An *X* or *Y* projection spectrum can be obtained with the **slice** code. The *X* projection spectrum obtained from ^{106}Pd coincidence data is shown in Figure 3.14. A uniform background spectrum was also defined for the projected spectrum, *x.spe* in **gf3**, using the *bg* command. The resulting spectra were used in the **xmesc** environment to create a compressed form of the built matrix. The mentioned background spectrum is subtracted from the total projection when the compressed matrix is built. Details of the mentioned procedure are documented in the Appendix. G.

The coincidence spectrum is gated using **xmesc** program. In the interactive graphical window, **XmEsc18r**, the user can define several gates and study the gated spectra in more detail. The spectrum gated on the 512-keV, $2_1^+ \rightarrow 0_1^+$ transition in ^{106}Pd is shown in Figure 3.15. A gated spectrum has a uniform background spectrum to be subtracted, which will provide an appropriate and consistent background reduction in any gated spectrum.

3.8.3 The Comparison Results

In a simple comparison between the *X* projection coincidence spectra of ^{106}Pd , Figure 3.14, and ^{94}Zr , Figure 3.9, the difference in the statistics is notable. On average, the

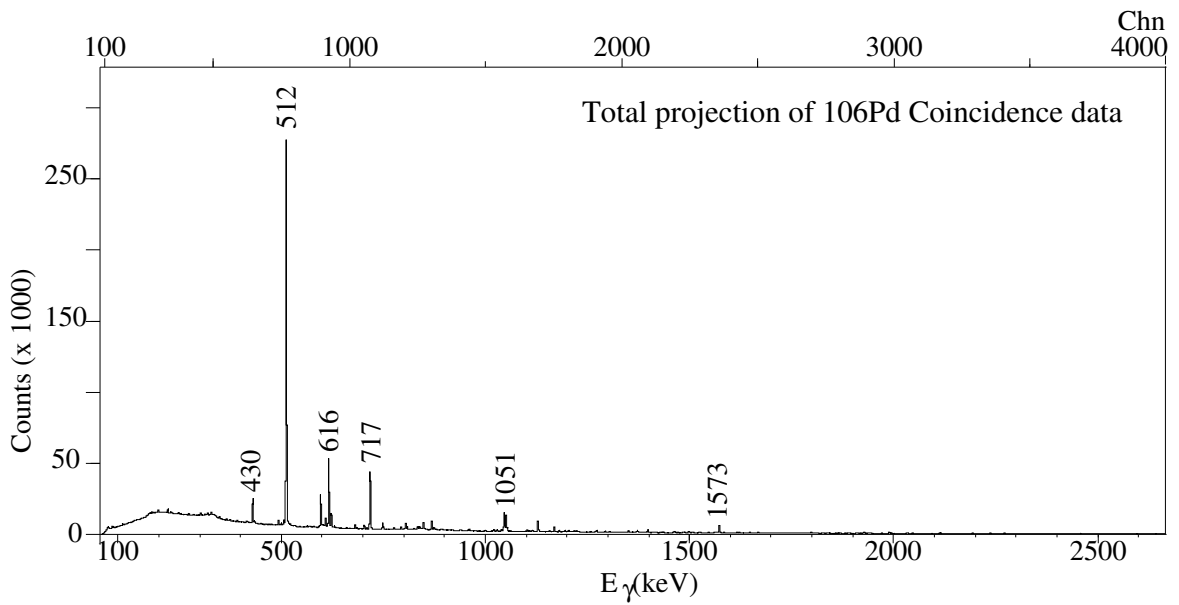


Figure 3.14: Total projection of the coincidence data for ^{106}Pd . The data were taken at the UK facility.

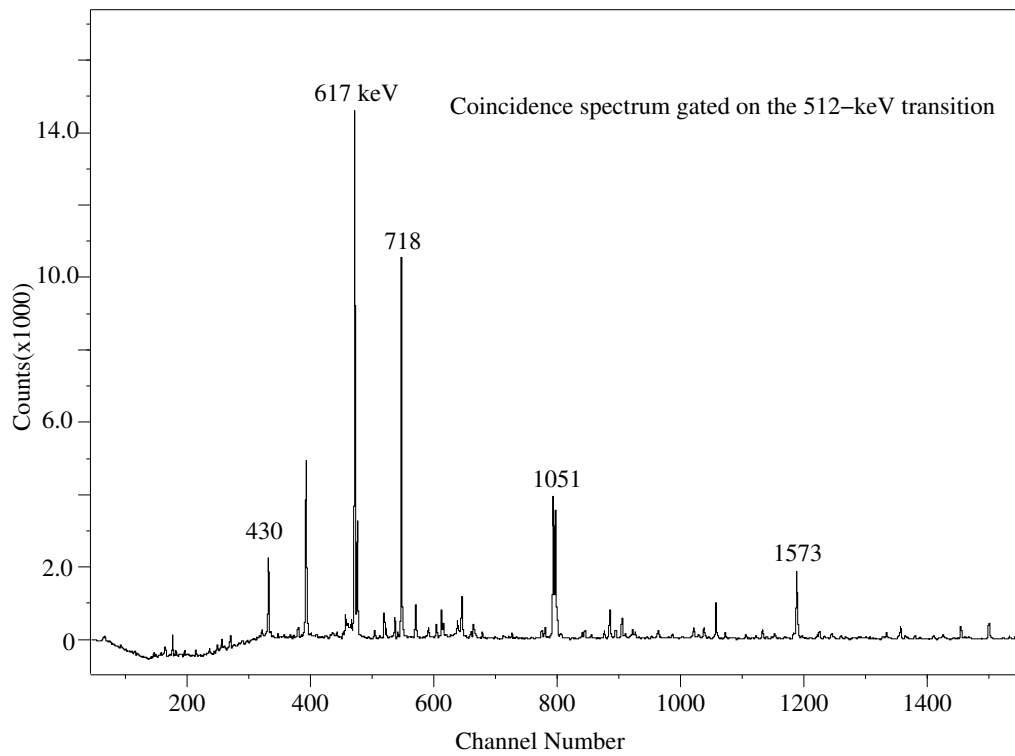


Figure 3.15: Coincidence spectrum gated on 512-keV γ ray, the $2_1^+ \rightarrow 0_1^+$ transition, in ^{106}Pd . The energies of the peaks are given in keV.

counts in the ^{106}Pd spectrum are an order of magnitude higher than in the ^{94}Zr spectrum. The counts in the low-energy region, the bump, look much higher in the ^{94}Zr spectrum, as well. The counts are ~ 14000 at the highest point in the ^{94}Zr spectrum, and ~ 16000 counts in the ^{106}Pd spectrum. Therefore, the peak-to-background ratio would be much smaller in the ^{94}Zr case.

The low statistics in the TUNL experiment were mainly due to the geometry of the coincidence setup. The clover detectors could not be positioned as close to the scattering sample as the HPGe detectors in the UK setup. Three clover detectors were positioned at 4.7, 11.5 and 5.8 cm from the scattering sample at respective angles of 270° , 135° , and 118° , with respect to the neutron beam, as shown in Figure 2.11. In the KEGS setup, on the other hand, all four HPGe detectors were positioned at ≈ 5 cm from the scattering sample at an angle of 90° with respect to the incident neutron beam; see Figure 3.11. This close geometry leads to good coincidence efficiency. In the TUNL geometry, practically only two detectors, clovers 1 and 3, were the dominantly responsive detectors; clover 2 was further back at a backward angle.

The low peak-to-background ratio of the TUNL data was disappointing. Another source contributing to this issue could be the BGO Compton suppression employed at TUNL. Creating the coincidence spectra with and without considering the BGO shields did not make a substantial difference in the spectra. In future experiments, careful adjustment of the BGOs to improve the peak-to-background ratio should be performed.

One important consideration in comparing the $\gamma\gamma$ coincidence data in the two experimental setups is related to the properties of the scattering sample. In the ^{106}Pd nucleus, the first excited state at 512 keV is low in energy compared to the 918-keV state in ^{94}Zr . It would have been a clearer comparison if the coincidence data on a nucleus closer to ^{94}Zr in mass, and level density and valence nuclear structure would have been used, but the only readily available UK data were on ^{106}Pd .

An efficiency calibration on the clover detectors in the same geometry as the coincidence setup was not available. While the TUNL coincidence data could thus not be used to determine the branching ratios in the decay of a level, the data set served the important purpose of building a more detailed level scheme for ^{94}Zr . The branching ratios can be determined when an efficiency calibration of the spectrometers is available. The high counting rates of events from standard calibration sources prompted us to move some of the clovers further from the scattering sample position, as explained in Section 2.3.

The coincidence measurements at TUNL provided an opportunity to have a unique experience of learning more about coincidence techniques and data analysis methods. The details on data analysis procedures for TUNL and UK coincidence experiments are documented in Appendices F and G, respectively.

Some improvements in the TUNL $(n, n'\gamma\gamma)$ measurements are needed in the experimental

setup and the data acquisition software to make it more practical and facile. The positions of the clover detectors, employment of the BGO as an active Compton suppression shield, and careful time window setup should be improved. As for the software, the scripted `SpecTcl` software used was suitable only for on-line data analysis, and many modifications were employed to analyze the data off line. Newer versions of the `SpecTcl` are more user friendly and have more functions, which can be used for off-line as well as on-line data analysis. This would reduce the time and effort necessary for the coincidence data analysis.

Copyright © Esmat Elhami 2008

CHAPTER 4: RESULTS AND DISCUSSION

In the $^{94}\text{Zr}(n,n'\gamma)$ measurement by Glasgow and coworkers [35], branching ratios and multipole mixing ratios for the transitions observed in the angular distribution measurements up to the 2887.7-keV level were obtained. Without lifetimes, transition strengths could not be determined from that study. The aim of this nuclear structure study of ^{94}Zr with the $(n,n'\gamma)$ reaction was the identification of the one-phonon mixed-symmetry (MS) state and possible two-phonon MS states, among other collective excitations, and valuable information was obtained. The experimental results and discussion are presented in this chapter.

4.1 Experimental Results

In this study the decay scheme of ^{94}Zr was established from excitation function and $\gamma\gamma$ coincidence data. A total of 38 new transitions and 8 new levels were established. The lifetimes, branching ratios, and multipole mixing ratios for many of the corresponding γ -ray transitions were obtained from the angular distribution measurements at $E_n = 2.3, 2.8$ and 3.5 MeV. For excited states above the 3.411-keV level, only data from the excitation function, performed up to $E_n = 4.0$ MeV, and $\gamma\gamma$ coincidences at $E_n = 5.0$ MeV, were used to establish the levels.

The experimental information is listed in Table 4.1. L and γ denote a newly observed level or γ -ray transition, respectively. The average $\overline{F}_{exp}(\tau)$ and lifetimes of the levels, τ (fs), are also listed. The levels, marked with *INS*, are known excited states, as given in Ref. [34], and were observed for the first time with the INS reaction. The γ -ray transitions, listed in Table 4.2, could not be placed in the level scheme. E_n refers to the incident neutron energy in the excitation function measurement at which the γ -ray was first observed. The measured reduced transition probabilities, $B(E2)$ and $B(M1)$, along with multipole mixing ratio, δ , are provided in Table 4.3. The electric dipole transitions, $B(E1)$, are listed in Table 4.4.

4.1.1 Level Scheme, $E_x < 3.0$ MeV

2^+ state at 918.8 keV

The first excited state with $J^\pi = 2_1^+$, decays to the ground state via an $E2$ transition. Its half life, $t_{1/2} = 6.9(15)$ ps, has been measured by the Coulomb excitation method [34]. In Table 4.1 the mean lifetimes are listed; the half-life time and the mean lifetime, τ , are related by $t_{1/2} = \tau \ln 2$. The transition to the ground state has $B(E2) = 4.9(3)$ W.u. [34]. In this work, mean lifetimes are the measured quantity. In the text lifetime refers to the mean lifetime.

0^+ state at 1300.4 keV

This level is the first 0^+ excited state, and it has a reported half life of $t_{1/2} = 0.291(11)$ ns. The only γ -ray transition to the 2_1^+ level, 381.58(10)keV, has $B(E2) = 9.4(4)$ W.u. [34]. The lifetime has been measured with the $\beta\gamma\gamma$ fast timing method, $\beta\gamma\gamma(t)$, by Mach et al. [62]. This level, based on its collective decay to the 2_1^+ , could be assigned as a member of two-phonon symmetric triplet in the vibrational limit.

4^+ state at 1469.6 keV

This level is the first 4^+ excited state, with a half life of $t_{1/2} = 0.500(13)$ ns, as measured with the $\beta\gamma\gamma(t)$ method [62]. The 550.8-keV γ ray, the decay to the 2_1^+ state, has a $B(E2)$ value of 0.879(23) W.u. [34], which is much weaker than the $0_2^+ \rightarrow 2_1^+$ $E2$ transition. Therefore, there is no convincing evidence to assign this excited state as a member of the two-phonon symmetric triplet. The validity of description of ^{94}Zr in the vibrational limit will be discussed in next chapter.

2_2^+ state at 1671.4 keV

The spin and parity of this state were determined previously [34] and were confirmed from our data. A lifetime of $\tau = 185_{-10}^{+15}$ fs was determined from the DSAM measurements at $E_n = 2.3$ MeV (see Figure 3.7). The branching intensities for the two transitions depopulating this level were also determined from the same data and are in disagreement with the NDS database [34]. Our results are, however, in agreement with the ^{94}Y β^- decay results, where intensities of $I_\gamma(752 \text{ keV}) = 2.5(2)$ and $I_\gamma(1671 \text{ keV}) = 4.4(4)$ were measured, indicating that the 1671-keV transition has a larger decay branch than the 752-keV transition [34].

In the previous INS measurements on ^{94}Zr by Glasgow et al. [35], the branching ratios of the γ -ray transitions depopulating a level were determined from the γ -ray cross sections, $\sigma_\gamma(E_\gamma)$ mb. These values were obtained from the a_2 and a_4 expansion coefficients in a least-squares polynomial fit to the angular distribution data at $E_n = 3.1$ MeV and are given in Table IV in Ref. [35]. The data showed a σ_γ of 169(16) mb for the 752-keV γ ray and 247(24) mb for 1671-keV γ ray, which naturally would result in a higher I_γ (and branching ratio) for the 1671-keV transition. Unfortunately, the compiled data in the ^{94}Zr level scheme in Fig. 21 of Ref. [35] shows 59 and 41 as branching ratios for 752- and 1671.8-keV transitions, respectively. These values appear to have been inverted in the NDS [34] and the NNDC data for ^{94}Zr [8].

The stronger decay branch to the ground state, the 1671-keV transition, gives a $B(E2)$ value of 7.8(7) W.u. This observation makes ^{94}Zr the only known case in which the $B(E2; 2_2^+ \rightarrow 0_1^+)$ is larger than the $B(E2; 2_1^+ \rightarrow 0_1^+)$.

The multipole mixing ratio for the 752 keV transition, $\delta = 0.02(2)$, shown in Figure 4.1 results in $B(M1) = 0.31(3) \mu_N^2$. This state has been proposed as the one-phonon MS state,

with an anomalous decay behavior [36]. Figure 4.1 also shows another minimum for the same transition at $\delta = 2.2(2)$; this mixing ratio gives a $B(E2; 2_2^+ \rightarrow 2_1^+)$ value of about 250(50) W.u., which is physically unrealistic and is rejected. The spin assignment $J = 3$ is ruled out, because there is also a ground-state transition from this level, 1671 keV. A $\Delta J = 3$ is unlikely. This state will be discussed in greater detail in Section 4.2.

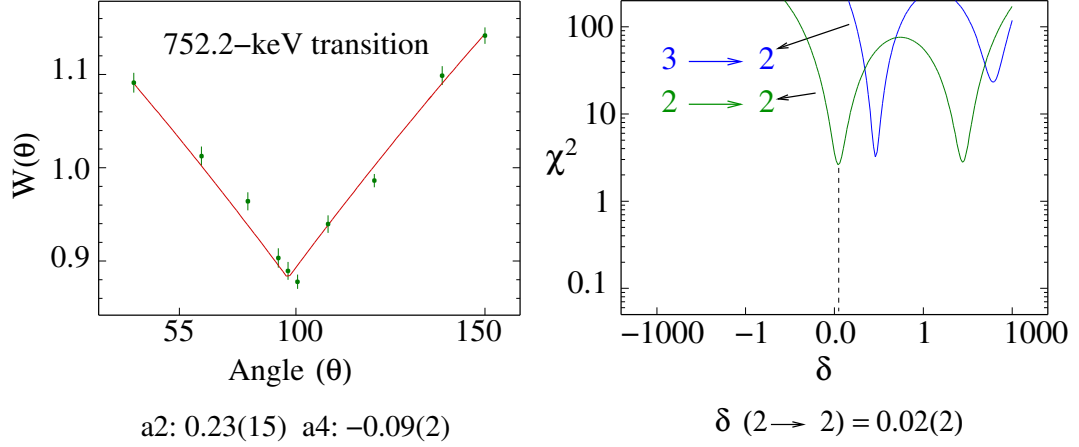


Figure 4.1: Angular distribution for 752-keV γ -ray transition, with a least-squares Legendre polynomial fit to the experimental data. The curve with a lower χ^2 confirms the $2 \rightarrow 2$ transition assignment and the corresponding multipole mixing ratio in the χ^2 vs δ plot. The data are from the angular distribution at $E_n=2.3$ MeV.

2_3^+ state at 2151.3 keV

In addition to the known $2_3^+ \rightarrow 2_1^+$ transition, 1232.4 keV, γ rays to the 2_2^+ state, 479.9 keV, and 0_1^+ state, 2151.3 keV were observed in this work. Although closer to the ~ 2 MeV energy region expected for a MS state, this level has a very weak $M1$ transition to the 2_1^+ state. It is dominantly $E2$ in character. The multipole mixing ratio of $\delta = -0.75^{+0.04}_{-0.05}$ for the 1232.4-keV transition, with a lifetime $\tau = 340^{+100}_{-65}$ fs resulted in $B(E2)$ of 11(3) W.u. and $B(M1) = 0.05^{+0.02}_{-0.01} \mu_N^2$, which is much smaller than the similar transition from the 2_2^+ level at 1671.4 keV. With about twice the strength of the $2_1^+ \rightarrow 0_1^+$ decay, the decay properties of this state are in closer agreement with a two-phonon excitation, although single-particle contributions are certainly present. The $E2$ transition to the ground state is very weak and has a $B(E2)$ value of $0.04^{+0.04}_{-0.02}$ W.u.

A careful analysis of the angular distribution of the $2_3^+ \rightarrow 2_2^+$ 479.9-keV γ ray resulted in δ values of $1.6^{+0.7}_{-0.6}$ and $0.19^{+0.25}_{-0.15}$, which have similar χ^2 values. The resulting transition strengths for the first δ are $B(E2) = 130^{+110}_{-70}$ W.u. and $B(M1) = 0.01(1) \mu_N^2$. If the large $B(E2)$ value is considered to be non-physical, then this δ value should be discarded. The latter δ value, though, results in a non-negligible $B(M1)$ value of $0.07^{+0.04}_{-0.03} \mu_N^2$ for this

transition and $B(E2) = 7_{-3}^{+4}$ W.u.

Even though the 1232.4-keV γ ray, the $2_3^+ \rightarrow 2_1^+$ transition, is dominantly $E2$, its $B(M1)$ amounts to $0.05_{-0.01}^{+0.02} \mu_N^2$, which is again non-negligible. It is larger than the limit of $0.01 \mu_N^2$ for transitions between symmetric multiphonon states, with $\Delta N_{phonon} = 1$ [15]. It will be noted that the $B(M1)$ values in ^{94}Zr do not fit within that limit, and the decay scheme does not fall into the description of the nearly spherical nuclei given by the Q -phonon scheme [15]. Such transitions will be discussed in more detail in Section 4.2.

4_2^+ state at 2329.9 keV

With a lifetime of 280_{-30}^{+40} fs, this level decays predominantly to the 2_1^+ state. A new $4_2^+ \rightarrow 2_2^+$ transition was also observed which, with a small branching ratio of 5.5(3)%, results in a large $B(E2) = 50_{-8}^{+10}$ W.u. The weak decay branch to the 4_1^+ state reported in NDS [34] was not observed in this work. It is surprising that the $E2$ decay branch from the 4_2^+ state to the 2_1^+ state is much stronger than the $4_1^+ \rightarrow 2_1^+$ transition, $B(E2; 4_1^+ \rightarrow 2_1^+) = 0.879(23)$ W.u. [34]. The negative g factor, $-0.8(4)$, measured for the 4_1^+ state [63] indicates a dominant neutron contribution to the wave function. No additional information is available for the 4_2^+ state.

2_4^+ state at 2366.3 keV

All the known transitions from this level [34] have been observed in this work. The δ values for all transitions are in agreement with the results of Glasgow *et al.* [35]. Different signs resulted from the phase conventions used in this work and in Ref. [35], where the Rose and Brink phase convention was used. This phase convention is related to the choice of phase for the electromagnetic vector potential, when the multipole mixing ratio is determined from the angular distribution of an aligned nucleus.

Two δ values were determined for the $2_4^+ \rightarrow 2_2^+$ 694-keV transition, $\delta_1 = 2.90_{-0.25}^{+0.35}$ and $\delta_2 = -0.07_{-0.04}^{+0.03}$. In this case, similar to the 479-keV transition from the 2151-keV level, δ_1 results in an unrealistically large $B(E2)$ value of 190_{-40}^{+60} W.u., whereas δ_2 results in a much smaller $B(E2)$ value but a relatively large $B(M1)$ value of $0.18_{-0.02}^{+0.03} \mu_N^2$. The similarity between this transition and the 479-keV, $2_3^+ \rightarrow 2_2^+$ transition, could be attributed to the characteristics of the 2_2^+ state, which has been identified as an anomalous one-phonon MS state [36]; both transitions populate the 2_2^+ state.

3_1^+ state at 2507.9 keV

The spin was assigned to this level from both the angular distribution and excitation function data. In addition to the known transitions to the 2_2^+ and 2_1^+ states, a new weak transition to the 2_3^+ state was observed in this work, but the angular distribution data were insufficient to provide a value for the mixing ratio of this transition. For the $3_1^+ \rightarrow 2_1^+$ $E2$

transition, $B(E2) = 10(5)$ W.u. is larger than that for the $3_1^+ \rightarrow 2_2^+$ transition, $B(E2) = 4_{-2}^{+1}$ W.u.

(1) state at 2698.5 keV

The 1779.3-keV transition to the 2_1^+ state has been observed in our singles and $\gamma\gamma$ coincidence spectra. It could not be included in the angular distribution and DSAM data analysis because this γ ray is at the same energy as a background γ ray(see Figure 2.8). New transitions to the 2_3^+ , 2_2^+ and 0_1^+ states were observed, and their excitation function plots showed the same threshold. Since these transitions were relatively weak, no δ values could be determined from their nearly isotropic angular distributions. However, from the excitation function and the angular distribution of the ground-state transition, the spin assignment was limited to 1, from (1, 2, 3) given in Ref. [34].

(3⁺) state at 2826.7 keV

In addition to a dominant transition to the 2_2^+ state, a decay branch to the 2_1^+ state was observed. The spin of this level is given in Ref. [34] as (2, 3). From the angular distributions, spin (3⁺) was assigned and confirmed from the excitation function data. Again, the transition to the 2_2^+ state has a large $B(E2) = 11.5(2)$ W.u., accompanied by a relatively large $B(M1)$ value of $0.17(3) \mu_N^2$.

1⁻ state at 2846.4 keV

For this state, the spin and parity (1⁻) as given in Ref. [34] were confirmed from our excitation function and angular distribution data. The decay to the ground state via an $E1$ transition with $\tau = 2.1(9)$ fs for the level. This state was excited in NRF measurements on ^{92}Zr , in which the scattering sample had a contamination of 2.03% ^{94}Zr [64], confirming the $J^\pi = 1^-$ assignment. Also, unpublished NRF results on ^{94}Zr by the Cologne group [65] agrees with this spin assignment. A weak 1927.3 keV γ -ray transition to the 2_1^+ state was also observed. It could not be included in angular distribution and DSAM data analysis as there is a background γ -ray peak at the same energy (see Figure 2.8). Therefore, a branching ratio of 100(2) has been assigned for the stronger ground-state transition, resulting in a slightly larger $B(E1)$ than the actual value. Nevertheless, this transition is $E1$ in character.

(5⁺) state at 2860.7 keV

A spin and parity assignment of 4⁺ is given for this level in Ref. [34]. In the $^{94}\text{Zr}(d, d')$ experiments, spin 4 was assigned to a level at 2.87 MeV [66]. From our data, a spin of 5⁺ was assigned from the angular distribution data. The unique δ value for a $5 \rightarrow 4$ transition was deduced from the χ^2 vs. δ plot. Also, the excitation function data favors the spin 5⁺. The only transition depopulating this level, $5^+ \rightarrow 4_1^+$, has a relatively small $B(E2)$ and a

non-negligible $B(M1)=0.07(2) \mu_N^2$.

(4^+) state at 2873.6 keV

This level, established in this work, decays predominantly to the 4_1^+ state. Other branches are the decays to the 4_2^+ and 2_1^+ states. The tentative spin of (4^+) was assigned based on excitation function and, less convincingly, from angular distribution data. With a relatively short lifetime, $\tau = 190_{-30}^{+40}$, this level decays to the 4_2^+ state with a large $B(M1) = 0.5(1) \mu_N^2$ and $B(E2) = 24(5)$ W.u. The δ value for this transition could be in question as the 543.7-keV γ ray is a weak transition and is close to the strong 550.8-keV (the $4_1^+ \rightarrow 2_1^+$ transition) γ ray, which could affect the peak fitting. Nevertheless, this transition has an unusual $B(M1)$ and $B(E2)$. Also, the angular distribution of the 1403-keV transition, the decay to the 4_1^+ state, could not provide a δ value.

2_5^+ state at 2908.0 keV

The assigned spin and parity, obtained from the angular distribution and excitation function data, confirm the results given in Ref. [34]. In addition to the known transitions to the 2_2^+ , 2_1^+ and 0_1^+ states, a new transition to the 2_3^+ state has been observed, with a $B(M1)$ value of $0.18(2)\mu_N^2$ and $B(E2) = 0.34(5)$ W.u. The 1236-keV transition to the 2_2^+ state, with 45(1)% branching ratio, has an anisotropic angular distribution, with two δ 's close in χ^2 value. The larger value, 6_{-2}^{+3} , for 1236-keV transition results in $B(E2) = 30_{-15}^{+30}$ W.u. and $B(M1)=0.002(1) \mu_N^2$, whereas the other, $\delta = -0.24_{-0.07}^{+0.06}$, results in $B(E2) = 1.7(2)$ W.u. and $B(M1) = 0.08(1) \mu_N^2$. Once again, a transition to the 2_2^+ state shows unusual decay behavior.

If the 2_3^+ state is considered as the two-phonon symmetric state, then the large $B(M1)$ of the $2_5^+ \rightarrow 2_3^+$ and large $B(E2)$ of the $2_5^+ \rightarrow 2_2^+$ transition indicate that the 2_5^+ state is a good candidate as the 2^+ two-phonon MS state, $2_{2,ms}^+$ in the multiphonon excitation scheme.

3_2^- state at 2927.5 keV

The angular distribution of the only transition to the 4_1^+ state indicates dipole character. The expansion coefficients, $a_2=0.11(17)$ and $a_4=0.11(22)$, favor $J^\pi = 3^-$ from the $J^\pi = (1^-, 3^-, 4^+)$ given in Ref. [34], as 3^- agrees better with the angular distribution data. The energy of the level is very close to the sum energy of the 3_1^- , at 2057.8 keV, and 2_1^+ states, which indicates this level could be a member of the two-phonon quadrupole-octupole coupled $(2_1^+ \otimes 3_1^+)$ quintuplet.

5_2^- state at 2945.3 keV

The spin and parity of this level were previously known [34], and it only decays to the 3_1^- state. A lower limit on the lifetime, 380 fs, was obtained from the DSAM measurements,

resulting in an upper limit of 150 W.u. for the $B(E2)$ value. This level could belong to the $2_1^+ \otimes 3_1^+$ quintuplet, since the energy of the level fits well with this assignment.

4.1.2 Level Scheme, $E_x > 3.0$ MeV

(0^+) state at 3000.1 keV

This new state decays only to the 2_1^+ state. The 2081.3-keV γ -ray was observed in the coincidence spectrum gated on the 918-keV transition. The excitation function plot shows a small yield, from which a tentative spin of (0^+) could be deduced. The closest level to this state, given in [34], is the 3014(8)-keV level with no J^π assignment, which was observed with the $^{92}\text{Zr}(t,p)^{94}\text{Zr}$ reaction [69].

(2^+) state at 3056.6 keV

The γ -ray peak, 2137.7 keV, is a doublet with the 2141 keV depopulating the level at 3058.5 keV. The spin assignment to this new observed level was obtained from the angular distribution of its transitions to the 2_1^+ state. A lifetime, $\tau = 100_{-25}^{+40}$ fs and a δ value were obtained for this transition, for which the $B(M1)$ and $B(E2)$ are provided in Table 4.3. The angular distribution favors a dominant $M1$ over an $E2$ character with $a_2=0.3(1)$ and $a_4=-0.01(12)$.

(2^-) state at 3058.5 keV

This state is a newly observed state, different from the state at 3059.31(17) keV, given in Ref. [34], with $J^\pi = (1, 2, 3)^+$. Three transitions are given as 1001.8(3), 1384.9(10), and 2140.60(20) keV, decaying to the 3_1^- , 2_2^+ , and 2_1^+ states, respectively. In this work, the only transitions observed and confirmed from the $\gamma\gamma$ coincidences were the 1385- and 2141-keV γ rays, which are from a level at 3058.5 keV. A 1001-keV γ ray was observed in the angular distribution data, but the spectral peak could not be fitted and it was not included in the data. The lifetime of the level, $\tau = 43(4)$ fs, was obtained from the DSAM data, and for both transitions, two δ values were obtained. From the angular distribution data a spin 2 was assigned.

The angular distribution of the 1385-keV γ ray has $a_2 = 0.16(6)$ and $a_4 = -0.06(8)$, which indicates a dominant dipole component. Depending on the parity of the state, it could be an $M1$ or an $E1$ transition. One of the δ value for the $(2) \rightarrow 2_2^+$ transition is almost zero, $-0.06(6)$, indicating this transition should be $E1$. The same is true for the 2141-keV γ ray, $a_2 = 0.11(7)$ and $a_4 = -0.06(9)$, with one $\delta = -0.13(8)$ approaching zero. The energy of this level is very close to the sum energies of the 2_1^+ and 3_1^- states, making it a good candidate for a member of the $2_1^+ \otimes 3_1^-$ quintuplet.

(4⁻) state at 3089.4 keV

The spin for this new level was assigned from the excitation function and the angular distribution of the 1031-keV γ ray, its stronger decay branch to the 3_1^- state, which indicates a dominant dipole component; $a_2 = -0.72(12)$ and $a_4 = 0.09(15)$. The angular distribution of the 1619-keV transition, the decay to the 4_1^+ state, favors 4^- , from the only δ value of $-0.1(1)$ for this transition. If the negative parity is accepted, this level, along with (2^-) level at 3058 keV, may belong to the $2_1^+ \otimes 3_1^-$ quintuplet, since it fits the energy characteria.

(4⁺) state at 3141.6 keV

In Ref. [34], a state at 3142.4(4) keV is given with $J^\pi = (6^+)$, which was assigned from the high-spin studies on ^{94}Zr with the $^{173}\text{Yb}(^{24}\text{Mg}, \text{F}\gamma)$ and $^{176}\text{Yb}(^{28}\text{Si}, \text{F}\gamma)$ reactions [34, 67], from the ground-state cascade of $6^+ \rightarrow 4^+ \rightarrow 2^+ \rightarrow 0^+$ and comparisons to the neighboring isotopes and shell model calculation predictions. This spin assignment does not agree with our results.

Three transitions are listed from this state in Ref. [34], but only one transition similar in energy with the $J_i \rightarrow 4_2^+$, 812.5-keV transition has been observed in our work. The observed γ ray is at 811.68(2) keV, with a relatively large yield in the excitation function, which favors $J = 4$ and rules out a higher spin. Also, from the determined lifetime, $\tau = 120_{-25}^{+30}$ fs, an assumed (6^+) $\rightarrow 4_2^+$ pure $E2$ multipolarity for the 811.68-keV transition would lead to a $B(E2) = 620_{-120}^{+140}$ W.u., which is unrealistic.

A very weak branch to the 2_2^+ state, 1470.1(5) keV, has also been observed in the excitation function prompt spectra, which has the same threshold as the 811.6-keV transition. The angular distribution could not provide any additional information. Even though the peak at 1470 keV was not observed in the background spectra, it could be mixed with the 1471.7-keV prompt γ ray in ^{74}Ge . This γ ray is a transition from a level at $E_x=2935$ keV, different from that in ^{94}Zr , yet not included in data. The placement of this transition could not be confirmed from the $\gamma\gamma$ coincidence data. The possibility that the 811.6-keV γ ray is a background radiation was ruled out from the the excitation function data, showing E_x above 3.0 MeV. There is a γ ray, similar in energy, from the $E_x=2673$ -keV level in ^{63}Cu [68]. Also with an anisotropic angular distribution, a background origin is unlikely.

These results indicate that the level at 3141.66(4) keV is a newly observed in this work. A tentative spin (4^+) is assigned from the angular distribution data. The data in Table 4.3 shows this transition has a large $B(M1) = 0.89_{-0.20}^{+0.24} \mu_N^2$.

(4⁺) state at 3155.9 keV

The spin and parity obtained from the angular distribution of the only γ -ray transition to the 2_1^+ state and the excitation function are in agreement with the (4^+) assignment given in Ref. [34]. This transition has $B(E2) = 11(1)$ W.u., which is reasonably large. The weak

decay branch to the 3_1^+ state was observed in the excitation function spectra, but the peak could not be fitted, and it was not included for determining branching ratios and lifetimes in Table 4.1.

(1⁺) state at 3200.3 keV

This new level with a short lifetime, $\tau = 9(3)$ fs, decays dominantly to the ground state. A weaker branch is observed to the 2_1^+ state. The spin (1⁺) assignment was obtained from angular distribution and excitation function data. This state was first observed in the NRF measurements [65] and $J = 1$ has been assigned. The angular distribution of the 2281.7-keV transition does not provide any information on δ values. If $J^\pi = 1^+$, the ground-state transition has $B(M1) = 0.16_{-0.04}^{+0.08} \mu_N^2$, which is large and could make it a candidate for the two-phonon 1^+ MS state; but other experimental signatures are not present, e.g., $1^+ \rightarrow 2_3^+$, or $1^+ \rightarrow 2_2^+$ transitions.

(3⁺) state at 3219.7 keV

Spin (1,2,3) is assigned to this level in Ref. [34]. In addition to the known transitions to the 3_1^- and 2_1^+ states, a new transition to the 2_3^+ state has been observed. The transition to the 4_1^+ state, 1751 keV, was observed, but it is contaminated with a background radiation. The spin of the level is limited to (2,3), otherwise, a transition to the 4_1^+ state would require $\Delta J = 3$, which is unlikely. The tentative spin (3) was assigned from the angular distribution. From the δ value of a $3 \rightarrow 3_1^-$ transition, $\delta = -0.064(64)$, which is almost zero, one can argue this transition could be either even or odd in parity. The transition to the 2^+ state has a non-zero δ value, which means it is not likely to be a parity-changing transition.

(2⁺) state at 3284.5 keV

This state, observed for the first time with the INS reaction, is closest in energy to the 3281(6)-keV level given in Ref. [34], which has only been observed with the (d, d') reaction. It decays to the 3_1^- , 2_1^+ , and 0_1^+ states. The spin (2⁺) has been assigned from the angular distribution, verified from the ground-state transition and excitation function data. The level has a very short lifetime, $\tau = 50_{-5}^{+6}$ fs, but the resulting transition strengths are not remarkable.

2⁺ state at 3318.6 keV

This state, observed for the first time with the INS reaction, decays with almost equal intensities to the 2_2^+ and 0_1^+ states. This level with a spin assignment of 2 has been observed in the NRF measurements [65]. In this work, spin 2⁺ is assigned from the ground-state transition, which clearly indicates quadrupole character. The level is very short lived, $\tau = 40_{-6}^{+7}$ fs, yet the ground-state $E2$ transition has a small $B(E2)$ value of $0.98_{-0.23}^{+0.30}$ W.u. From

the angular distribution of the 1647.0-keV transition, the decay branch to the 2_2^+ state, no unique δ value could be obtained.

(1⁺) state at 3331.3 and (5⁺) state at 3336.2 keV

A level at 3331(6), with a $J^\pi = (5^-)$ assignment, is given in Ref. [34] and has been observed in (d, d') , (p, p') , and (α, α') reactions [34]. But in this work, there are two states near this energy. Two γ -ray transitions were observed: 2412.5 keV, depopulating the state at 3331.3 keV to the 2_1^+ state and 1866.5 keV, decaying from the level at 3336.2 keV to the 4_1^+ state. The γ -ray excitation function plots show similar thresholds, but with the help of the $\gamma\gamma$ coincidence data, the transitions were placed as decays from two separate levels. The tentative spins were assigned from the angular distribution and excitation function data. The 3331-keV level has a long lifetime with a large uncertainty, $\tau = 270_{-120}^{+570}$ fs, which can be attributed to large uncertainties in the γ -ray peak centroid. The 3336-keV level, on the other hand, has a very short lifetime, $\tau = 53_{-14}^{+20}$ fs, indicating these levels are two separated levels.

(3) state at 3361.4 keV

In addition to the known transitions to the 2_1^+ and 4_1^+ states, a new transition to the 2_4^+ state has been observed. Its excitation function shows a threshold similar to the other transitions, but its placement could not be confirmed from the $\gamma\gamma$ coincidences. This transition was not included in obtaining the branching ratios and lifetime for this level. The transition to the 3_1^- state, given in [34], was not observed. The 2442-keV transition to the 4_1^+ state indicates dipole character, but it did not provide any information on the δ or spin assignment of this level. In the Ref. [34] spin (1,2,3) are given, from which a tentative spin (3) was obtained from the excitation function data.

(4⁺) state at 3411.2 keV

A level at 3407(6) keV, with spin $(3^-, 4^+)$, is given in Ref. [34], which have been observed in the (d, d') and (α, α') reactions [34]. The only transition, to the 2_1^+ state, has an isotropic angular distribution. A tentative spin (4^+) was obtained from the excitation function data. With this spin assignment, a pure $E2$ transition would have $B(E2) = 25_{-10}^{+15}$ W.u. For a negative parity, the dominant $E1$ transition strength would amounts to $B(E1)=7(2)$ mW.u.

Excited states above the 3411.2-keV level

For most of these excited states, spin 4 or 5 has been assigned from the excitation function data. Therefore, the spin assignments are not held in high confidence.

Table 4.1: Experimental information on the ^{94}Zr level scheme. I_γ , the relative intensities of the transitions from a given level, sum to 100. A 10% systematic uncertainty in the $F(\tau)$ value due to uncertainty in the stopping power process is not included in the data. γ denotes a new transition, and L for a level established in this work. Spin assignments were obtained from the angular distribution, denoted by $J(AD)$, or excitation function data, denoted by $J(Exf)$. The J^π values in parentheses are tentatively assigned spins from this work. A known level also observed with the INS reaction is marked as *INS*.

E_l (keV)	J_i^π	J_f^π	E_γ (keV)	I_γ (%)	$F(\tau)$	τ (fs)	Notes
918.82(2)	2_1^+	0_1^+	918.82(2)	100	-	9.9(21)	a
1300.39(2)	0_2^+	2_1^+	381.58(10)	100	-	420(16)	a
1469.70(2)	4_1^+	2_1^+	550.78(10)	100	-	721(18)	a
1671.47(2)	2_2^+	2_1^+	752.50(10)	42(1)	0.180(11)	185_{-10}^{+15}	b
		0_1^+	1671.40(10)	58(1)			b
2057.87(2)	3_1^-	4_1^+	588.05(10)	2.5(5)	0.351(20)	75(6)	
		2_1^+	1138.96(5)	97.5(5)			
2151.34(2)	2_3^+	2_2^+	479.90(20)	5(1)	0.097(22)	340_{-65}^{+100}	γ
		2_1^+	1232.40(10)	93(1)			
		0_1^+	2151.30(30)	2(1)			γ
2329.97(2)	4_2^+	2_2^+	658.45(5)	5.5(3)	0.127(14)	280_{-33}^{+40}	γ
		2_1^+	1411.11(5)	94.5(3)			
2366.34(2)	2_4^+	3_1^-	308.50(5)	8(1)	0.094(11)	390_{-45}^{+60}	
		2_2^+	694.80(5)	40(1)			
		0_2^+	1065.89(5)	10.5(5)			
		2_1^+	1447.55(20)	41.5(5)			
2507.92(2)	3_1^+	2_3^+	356.6(5)	3(2)	0.070(14)	520_{-90}^{+140}	$\gamma, c, J(AD, Exf)$
		2_2^+	836.39(10)	14(2)			

Table 4.1: (continued)

E_l (keV)	J_i^π	J_f^π	E_γ (keV)	I_γ (%)	$\overline{F}(\tau)$	τ (fs)	Notes
		2_1^+	1589.15(20)	83(2)			
2605.39(3)	5_1^-	4_1^+	1135.67(30)	100	0.201(41)	160_{-30}^{+50}	
2698.45(3)	(1)	2_3^+	547.30(7)				$\gamma, J(AD), c$
		2_1^+	1779.32(10)				d
		2_2^+	1026.91(20)				γ, e
		0_1^+	2698.88(35)				γ
2826.75(3)	(3^+)	2_2^+	1155.27(2)	88.5(5)	0.209(25)	170_{-20}^{+30}	$J(Exf, AD)$
		2_1^+	1907.91(4)	11.5(5)			γ
2846.36(3)	1^-	2_1^+	1927.30(10)	-	0.962(16)	2.1(9)	$J(AD), d$
		0_1^+	2846.36(5)	100(2)			
2860.70(3)	(5^+)	4_1^+	1390.99(2)	100	0.138(24)	270_{-45}^{+65}	$J(Exf)$
2873.65(3)	(4^+)	4_2^+	543.74(20)	27(1)	0.189(27)	190_{-30}^{+40}	$\gamma, L, J(AD, Exf), c$
		4_1^+	1403.93(2)	60(1)			γ
		2_1^+	1954.91(7)	13(1)			γ, c
2888.25(7)	4^+	2_1^+	1969.42(5)	100	0.231(17)	145_{-10}^{+15}	
2908.04(2)	2_5^+	2_3^+	756.71(3)	22.5(7)	0.211(17)	165_{-15}^{+20}	$\gamma, J(AD, Exf), INS$
		2_2^+	1236.57(2)	45(1)			
		2_1^+	1989.21(3)	17.5(7)			
		0_1^+	2908.05(10)	15(1)			
2927.50(5)	3_2^-	4_1^+	1457.79(4) ⁿ	100	0.141(56)	260_{-85}^{+200}	$\gamma, J(AD), INS$
2945.33(5)	5_2^-	3_1^-	887.46(3)	100	0.028(71)	>380	$J(AD)$

Table 4.1: (continued)

E_l (keV)	J_i^π	J_f^π	E_γ (keV)	I_γ (%)	$\overline{F}(\tau)$	τ (fs)	Notes
3000.01(4)	(0 ⁺)	2 ₁ ⁺	2081.27(3)	100	0.175(26)	200 ₋₃₀ ⁺⁴⁰	$\gamma, L, J(Exf), INS, c$
3029.72(13)	(5 ⁺)	4 ₁ ⁺	1560.01(10)	100	0.000(32)	>1250	$\gamma, J(Exf, AD), INS$
3056.35(13)	(2 ⁺)	2 ₁ ⁺	2137.5(10)	100	0.304(68)	100 ₋₂₅ ⁺⁴⁰	$\gamma, L, J(AD)$
3058.50(50)	(2 ⁻)	2 ₂ ⁺	1385.10(50)	45(1)	0.517(24)	43(4)	$J(AD)$
		2 ₁ ⁺	2141.10(50)	55(1)			
3089.39(46)	(4 ⁻)	3 ₁ ⁻	1031.48(5)	55(1)	0.157(43)	230 ₋₆₀ ⁺¹⁰⁰	$\gamma, L, J(Exf)$
		4 ₁ ⁺	1619.7(5)	45(1)			γ
3141.66(4)	(4 ⁺)	4 ₂ ⁺	811.68(2)	100(2)	0.265(45)	120 ₋₂₅ ⁺³⁰	$\gamma, L, J(Exf), INS$
		2 ₂ ⁺	1470.1(5)				γ, d, e
3155.93(3)	(4 ⁺)	2 ₁ ⁺	2237.11(2)	100	0.466(17)	50(3)	
3200.28(4)	(1 ⁺)	2 ₁ ⁺	2281.73(11)	11.5(2)	0.838(47)	9(3)	$\gamma, c, L, J(Exf)$
		0 ₁ ⁺	3200.27(3)	88.54(2)			γ
3219.72(4)	(3 ⁺)	2 ₃ ⁺	1069.58(50)	22.5(8)	0.321(29)	95 ₋₁₀ ⁺¹⁵	$\gamma, J(AD)$
		3 ₁ ⁻	1161.82(3)	52(1)			
		4 ₁ ⁺	1751.04(11)	-			d
		2 ₁ ⁺	2301.44(10)	25.5(8)			c
3224.84(4)	(4 ⁺)	4 ₁ ⁺	1755.22(10)	75(1)	0.346(27)	80 ₋₉ ⁺¹⁰	$\gamma, L, J(AD)$
		2 ₁ ⁺	2305.98(10)	25(1)			γ, u
3284.46(6)	(2 ⁺)	3 ₁ ⁻	1226.34(5)	34(1)	0.476(30)	50 ₋₅ ⁺⁶	γ, INS
		2 ₁ ⁺	2365.65(5)	58(2)			γ
		0 ₁ ⁺	3284.29(16)	8(2)			γ

Table 4.1: (continued)

E_l (keV)	J_i^π	J_f^π	E_γ (keV)	I_γ (%)	$\overline{F}(\tau)$	τ (fs)	Notes
3318.63(7)	(2 ⁺)	2 ₂ ⁺	1647.00(50)	51(5)	0.527(41)	40 ₋₆ ⁺⁷	$\gamma, J(AD), INS$
		0 ₁ ⁺	3318.63(5)	49(5)			γ
3331.34(65)	(1 ⁺)	2 ₁ ⁺	2412.51(50)	100	0.134(87)	270 ₋₁₂₀ ⁺⁵⁷⁰	$\gamma, c, J(AD), INS$
3336.22(65)	(5 ⁺)	4 ₁ ⁺	1866.52(50)	100	0.451(80)	55 ₋₁₅ ⁺²⁰	$\gamma, J(AD), J(Exf)$
3361.41(6)	(3)	2 ₄ ⁺	996.77(3)		0.355(42)	80 ₋₁₀ ⁺¹⁵	$\gamma, e, J(Exf)$
		4 ₁ ⁺	1891.68(4)	74(2)			
		2 ₁ ⁺	2442.86(14)	26(2)			<i>c</i>
3411.21(12)	(4)	2 ₁ ⁺	2492.38(10)	100	0.774(78)	15 ₋₅ ⁺⁶	γ
3482.33(13)	(4 ⁺)	4 ₁ ⁺	2012.6(1)				$\gamma, J(Exf), INS$
3551.96(13)	-	2 ₁ ⁺	2633.1(2)				γ, INS
3553.13(13)	(5 ⁺)	4 ₁ ⁺	2083.4(1)				$\gamma, L, J(Exf)$
3561.93(26)	(5 ⁺)	4 ₁ ⁺	2092.2(2)				$\gamma, J(Exf), INS$
3579.56(13)	(4 ⁺)	2 ₁ ⁺	2660.7(1)				$\gamma, L, J(Exf), INS$
3597.36(13)	-	2 ₁ ⁺	2678.5(1)				$\gamma, J(Exf), INS$
3699.23(13)	(4 ⁺)	4 ₁ ⁺	2229.5(1)				$\gamma, L, J(Exf), INS$

a Lifetime value in ps from Ref. [34].

b New branching intensities, different from Ref. [34].

c No δ value can be determined, due to the small yields in the angular distribution data.

d This transition was near a background peak, and is not included in the data.

e The placement of the transition is uncertain.

Table 4.2: γ rays which could not be placed in the level scheme. Their thresholds are given as E_n .

E_γ (keV)	E_n (MeV)
1398.1(1)	2.8
1484.3(1)	3.5
1855.6(1)	3.4
1981.4(1)	2.9
2252.8(2)	3.6
2398.5(1)	3.5
2561.9(1)	3.7
2671.3(2)	3.7
3156.3(1)	3.5
3547.6(2)	3.7
3660.8(2)	3.9
3681.3(2)	3.9
3871.6(2)	3.9

Table 4.3: $B(M1)$ and $B(E2)$ values calculated for γ -ray transitions in ^{94}Zr . b denotes the γ rays which are near a background peak. Those transitions for which no δ value could be obtained are marked by d . For most transitions, the δ with the lower χ^2 was chosen, but two δ 's are reported when both had similar χ^2 . The $B(M1) \downarrow$ and $B(E2) \downarrow$ values are given in μ_N^2 and W.u., respectively. For $B(E2)$ values, 1 W.u. = $25.387 e^2 fm^4$ for ^{94}Zr .

E_l (keV)	J_i^π	J_f^π	E_γ (keV)	δ	$B(M1) \downarrow$ (μ_N^2)	$B(E2) \downarrow$ (W.u.)
918.82(2)	2_1^+	0_1^+	918.82(2)	$E2$		4.9(3)
1300.39(2)	0_2^+	2_1^+	381.58(10)	$E2$		9.4(4)
1469.70(2)	4_1^+	2_1^+	550.78(10)	$E2$		0.879(23)
1671.47(2)	2_2^+	2_1^+	752.50(10)	0.02(2)	0.31(3)	0.18(2)
		0_1^+	1671.40(10)	$E2$		7.8(7)
2057.87(2)	3_1^-	4_1^+	588.05(10)	$E1$		
		2_1^+	1138.96(5)	$E1$		
2151.34(2)	2_3^+	2_2^+	479.90(20)	$1.6_{-0.6}^{+0.7}$	0.01(1)	130_{-70}^{+110}
				$0.19_{-0.15}^{+0.25}$	$0.07_{-0.03}^{+0.04}$	7_{-3}^{+4}
		2_1^+	1232.40(10)	$-0.75_{-0.05}^{+0.04}$	$0.05_{-0.01}^{+0.02}$	11(3)

Table 4.3: (continued)

E_l (keV)	J_i^π	J_f^π	E_γ (keV)	δ	$B(M1) \downarrow$ (μ_N^2)	$B(E2) \downarrow$ (W.u.)
		0_1^+	2151.30(30)	$E2$		$0.04_{-0.02}^{+0.04}$
2329.97(2)	4_2^+	2_2^+	658.45(5)	$E2$		50_{-8}^{+10}
		2_1^+	1411.11(5)	$E2$		20_{-2}^{+3}
2366.34(2)	2_4^+	3_1^-	308.50(5)	$E1$		
2366.34(2)	2_4^+	2_2^+	694.80(5)	$2.90_{-0.26}^{+0.34}$	0.018(5)	190_{-40}^{+60}
				$-0.07_{-0.04}^{+0.03}$	$0.18_{-0.02}^{+0.03}$	1.02(15)
		0_2^+	1065.89(5)	$E2$		6(1)
		2_1^+	1447.55(20)	$0.6_{-0.2}^{+0.3}$	0.014(3)	$1.6_{-0.4}^{+0.5}$
2507.92(2)	3_1^+	2_3^+	356.6(5)	d		
		2_2^+	836.39(10)	-0.9(4)	0.01(1)	10(5)
		2_1^+	1589.15(20)	$1.5_{-0.7}^{+0.2}$	$0.006_{-0.002}^{+0.005}$	4_{-2}^{+1}
2605.39(3)	5_1^-	4_1^+	1135.67(30)	$E1$		
2826.75(3)	(3^+)	2_2^+	1155.27(2)	0.40(3)	0.17(3)	11.5(2)
		2_1^+	1907.91(4)	$0.50_{-0.10}^{+0.15}$	0.004(1)	$0.18_{-0.04}^{+0.05}$
2846.36(3)	1^-	2_1^+	1927.30(10)	$E1$		
		0_1^+	2846.36(5)	$E1$		
2860.70(3)	(5^+)	4_1^+	1390.99(2)	$0.35_{-0.04}^{+0.05}$	0.07(2)	$2.5_{-0.5}^{+0.6}$
2873.65(3)	(4^+)	4_2^+	543.74(20)	$-0.16_{-0.08}^{+0.10}$	0.5(1)	24(5)
		4_1^+	1403.93(2)	-0.5(1)	0.05(1)	4(1)
		2_1^+	1954.91(7)	$E2$		0.8(2)
2888.25(7)	4^+	2_1^+	1969.42(5)	$E2$		7.5(7)

Table 4.3: (continued)

E_l (keV)	J_i^π	J_f^π	E_γ (keV)	δ	$B(M1) \downarrow$ (μ_N^2)	$B(E2) \downarrow$ (W.u.)
2908.04(2)	2_5^+	2_3^+	756.71(3)	$-0.04_{-0.08}^{+0.09}$	0.18(2)	0.34(5)
				$2.7_{-0.6}^{+0.9}$	0.02(1)	130_{-50}^{+75}
		2_2^+	1236.57(2)	6_{-2}^{+3}	0.002(1)	30_{-15}^{+30}
				$-0.24_{-0.07}^{+0.06}$	0.08(1)	1.7(2)
				2_1^+	1989.21(3)	0.005(2)
	0_1^+	2908.05(10)	$E2$		0.14(3)	
2927.50(5)	3_2^-	4_1^+	1457.79(4)	$E1$		
2945.33(5)	5_2^-	3_1^-	887.46(3)	$E2$		<150
3000.01(4)	(0^+)	2_1^+	2081.27(3)	$E2$		4(1)
3029.72(13)	(5^+)	4_1^+	1560.01(10)	$-0.28_{-0.09}^{+0.08}$	<0.01	<0.20
3056.35(13)	(2^+)	2_1^+	2137.5(10)	$0.15_{-0.08}^{+0.15}$	0.06(2)	$0.16_{-0.05}^{+0.06}$
3089.39(46)	(4^-)	3_1^-	1031.48(5)	-0.3(1)	0.11(4)	5(2)
		4_1^+	1619.7(5)	$E1$		
3141.66(4)	(4^+)	4_2^+	811.68(2)	$-0.01_{-0.08}^{+0.09}$	$0.89_{-0.20}^{+0.24}$	0.13(3)
		2_2^+	1470.1(5)	b		
3155.93(3)	(4^+)	2_1^+	2237.11(2)	$E2$		11(1)
3200.28(4)	(1^+)	2_1^+	2281.73(11)	d		
		0_1^+	3200.27(3)	$M1$	$0.16_{-0.04}^{+0.08}$	
3219.72(4)	(3^+)	2_3^+	1069.58(50)	$2.05_{-0.70}^{+0.75}$	0.02(1)	46_{-22}^{+28}
		3_1^-	1161.82(3)	$E1$		
		4_1^+	1751.04(11)	d		

Table 4.3: (continued)

E_l (keV)	J_i^π	J_f^π	E_γ (keV)	δ	$B(M1) \downarrow$ (μ_N^2)	$B(E2) \downarrow$ (W.u.)
		2_1^+	2301.44(10)	d		
3224.84(4)	(4^+)	4_1^+	1755.22(10)	$0.09_{-0.14}^{+0.25}$	0.09(1)	0.17(2)
				$0.99_{-1.07}^{+0.38}$	$0.05_{-0.02}^{+0.05}$	9_{-7}^+
		2_1^+	2305.98(10)	$E2$		1.5(3)
3284.46(6)	(2^+)	3_1^-	1226.3(5)	$E1$		
		2_1^+	2365.65(5)	$1.93_{-0.46}^{+0.72}$	0.014(6)	4_{-1}^{+2}
		0_1^+	3284.29(16)	$E2$		$0.14_{-0.04}^{+0.05}$
3318.63(7)	(2^+)	2_2^+	1647.00(50)	d		
		0_1^+	3318.63(5)	$E2$		$0.98_{-0.23}^{+0.30}$
3331.34(65)	(1^+)	2_1^+	2412.51(50)	d		
3336.22(65)	(5^+)	4_1^+	1866.52(50)	0.5(1)	$0.13_{-0.04}^{+0.06}$	5(2)
3361.41(6)	(3^+)	2_4^+	996.77(3)	d		
		4_1^+	1891.68(4)	-0.01(8)		
		2_1^+	2442.86(14)	d		
3411.21(12)	(4^+)	2_1^+	2492.38(10)	$E2$		25_{-10}^{+15}

Table 4.4: $B(E1)$ values calculated for γ -ray transitions between the low-lying states of ^{94}Zr . The $B(E1) \downarrow$ values are given in mW.u. ($= 1.33 \times 10^{-3} e^2 fm^2$ for ^{94}Zr). b denotes that the transition was mixed with a background line, not included in data analysis.

E_l (keV)	J_i^π	J_f^π	E_γ (keV)	δ	$B(E1) \downarrow$ (mW.u.)	$B(E1) \downarrow$ ($\times 10^{-3} e^2 fm^2$)
2057.87(2)	3_1^-	4_1^+	588.05(10)	$E1$	0.8(2)	1.0(3)
		2_1^+	1138.96(5)	$E1$	$4.3_{-0.3}^{+0.4}$	$5.7_{-0.4}^{+0.5}$
2366.34(2)	2_4^+	3_1^-	308.50(5)	$E1$	3.3(5)	4.36(6)
2605.39(3)	5_1^-	4_1^+	1135.67(30)	$E1$	$2.0_{-0.5}^{+0.6}$	2.7(7)
2846.36(3)	1^-	2_1^+	1927.30(10)	b		
		0_1^+	2846.36(5)	$E1$	10_{-3}^{+7}	13_{-4}^{+10}
2927.50(5)	3_2^-	4_1^+	1457.79(4)	$E1$	0.6(3)	$0.8_{-0.3}^{+0.4}$
3058.50(50)	(2^-)	2_2^+	1385.10(50)	1.9(2)		
		2_1^+	2141.10(50)	$0.60_{-0.05}^{+0.06}$		
3089.39(46)	(4^-)	3_1^-	1031.48(5)	$E2/M1$		
		4_1^+	1619.7(5)	$E1$	0.2(1)	0.3(1)
3219.72(4)	(3^+)	3_1^-	1161.82(3)	$E1$	1.7(2)	$2.3_{-0.3}^{+0.4}$
3284.46(6)	(2^+)	3_1^-	1226.3(5)	$E1$	1.8(3)	2.4(4)
		2_1^+	2365.65(5)	$E2/M1$		
		0_1^+	3284.29(16)	$E2$		
3411.21(12)	(4^-)	2_1^+	2492.38(10)	$E1$	7(2)	

4.2 Discussion

The experimental results, including the transition strengths provided in Table 4.3, indicate interesting and anomalous decay behavior in the low-lying states of ^{94}Zr . The results are discussed in this section.

4.2.1 Quadrupole-phonon Excitations

The ^{94}Zr nuclear structure does not fall into a simple vibrational picture, as one would expect for this nearly spherical nucleus. The 2_2^+ state at 1671.4 keV has a larger $E2$ ground-state transition than the 2_1^+ state. Also, the $B(E2)$ value for the $2_1^+ \rightarrow 0_1^+$ transition, 4.9(3) W.u. [34], is too small to indicate significant collectivity, even smaller than that of ^{92}Zr .

Even if the 2_1^+ state is considered as the one-phonon symmetric state, and the dominant $E2$ transitions of $0_2^+ \rightarrow 2_1^+$, 9.4(4) W.u. [34], suggests that this state belong to the two-phonon symmetric triplet, the 0_2^+ state at 1300.4 keV is at a lower energy than expected. On the other hand, the 2_3^+ state at 2151.3 keV decays with a dominant $E2$ transition to the 2_1^+ state, 11(2) W.u., and the energy of the level agrees with its assignment as a member of the two-phonon symmetric states. But this level also decays to the 2_2^+ state via a 479.9-keV γ ray, for which two δ values were obtained. One δ value resulted in an unrealistically large $B(E2)$, and the other δ in a smaller $B(E2)$, accompanied with a non-negligible $B(M1)$ value. There is no candidate for the third member of the two-phonon triplet, the 4^+ state. The $B(E2)$ of the transition from the 4_1^+ state at 1469.7 keV to the 2_1^+ state, 0.878(23) W.u. [34] is too small to be considered collective. The 4_2^+ state at 2329.9 keV has a larger $E2$ transition strength to the 2_1^+ state than that of the $4_1^+ \rightarrow 2_1^+$ transition. But its $E2$ transition to the 2_2^+ state is even larger than that of the $4_2^+ \rightarrow 2_1^+$ transition, which contradicts its candidacy for a two-phonon symmetric state. More realistic assignments for these states is yet to be determined. In general, the $B(E2)$ values or the energy of the aforementioned levels do not support a collective structure in ^{94}Zr .

4.2.2 $2_1^+ \otimes 3_1^-$ Quintuplet

Even though there is no experimental evidence for the quadrupole multiphonon excitations, there are possible candidates for the quadrupole-octupole coupling excitations, i.e., the members of the $(2_1^+ \otimes 3_1^-)$ quintuplet. According to the energy sum rule in the phonon-coupling excitations, the energy of the 1^- state at 2846.4 keV, 3_2^- at 2925.7 keV, 5_2^- at 2945.3 keV, (2^-) at 3058.5 keV, and the (4^-) state at 3089.4 keV are close to the summed energy of the 2_1^+ and 3_1^- states, $E_{2_1^+} + E_{3_1^-}$, which are 918.8 and 2057.9 keV, respectively. Even though these states fit the energy characteria, not all of them decay to the one-phonon quadrupole (2_1^+) or octupole (3_1^-) states, as expected. For example the 3_2^- state only decays to the 4_1^+ state. The $B(E1)$ values observed are larger than the expected values in this region [70].

4.2.3 Anomalous Decay Behavior of Low-lying States in ^{94}Zr

The 2_2^+ State

The 2_2^+ state at 1671.4 keV decays via a dominant $M1$ transition to the 2_1^+ state, which resulted in its identification as the one-phonon MS state [36]. However, it decays by a stronger $E2$ transition to the ground state than that of the 2_1^+ to ground-state transition. For this reason, we have called this level an anomalous MS state. This argument has yet to be verified by calculations.

The 4_2^+ State

Another excited state with an anomalous decay pattern is the 4_2^+ state at 2329.9 keV. It has a larger $E2$ transition strength to the 2_1^+ state than that of the $4_1^+ \rightarrow 2_1^+$ transition. Also, the $B(E2; 4_2^+ \rightarrow 2_2^+)$ value is larger than that of the $B(E2; 4_2^+ \rightarrow 2_1^+)$ value.

The (3^+) State at 2826 keV

The $(3^+) \rightarrow 2_2^+$ transition has a large $B(E2)$ value, accompanied by a large $B(M1)$. Also, the $3_1^+ \rightarrow 2_1^+$ $E2$ transition strength is larger than the $3_1^+ \rightarrow 2_2^+$ $E2$ transition. It is evident that the decay behavior of the yrast states is different from that of the higher-energy states of the same spin.

4.2.4 A Simple Classification of the Excited States in ^{94}Zr

The low-lying excited states can be classified according to their decay behavior. Partial decay schemes of the positive-parity states depicting interesting behaviors are shown in Figures 4.2 and 4.3 for transitions from the $J^\pi = 2^+$ and $J^\pi = 3^+, 4^+$ states, respectively. There are distinct differences between the states populating the 2_1^+ state and those decaying to the 2_2^+ state. A comparison of these transition strengths may help in understanding the nuclear structure of ^{94}Zr . The 2_1^+ and 2_2^+ states are not treated as symmetric or MS states for this classification.

Some states decay to the 2_1^+ state via transitions with large $B(E2)$ values, e.g., the 0_2^+ and 2_3^+ states. Additional states that decay in this manner are the 4^+ excited states at higher energies (see Figure 4.3).

Other states populate the 2_2^+ state with large $B(E2)$ values, e.g., the 3_1^+ and 4_2^+ states. These states along with the (3^+) state at 2826 keV appear to belong to excitations built on the 2_2^+ state (see Figure 4.3).

Several additional states populate the 2_2^+ state; they suggest either pure $E2$ transitions, with unrealistic $B(E2)$ values, or a smaller $B(E2)$ accompanied with a large $B(M1)$ value. Usually, these are transitions for which a unique δ value could not be determined. The $B(E2)$ resulting from one δ would be too large to be considered realistic, and the other δ value would result in rather large $B(M1)$ values. For example, the decays of the 2_3^+ and 2_4^+ states to the 2_2^+ state show such behavior, as shown in Figure 4.2.

The $2_5^+ \rightarrow 2_2^+$ transition has either a dominant $E2$ character or a smaller $B(E2)$ with a

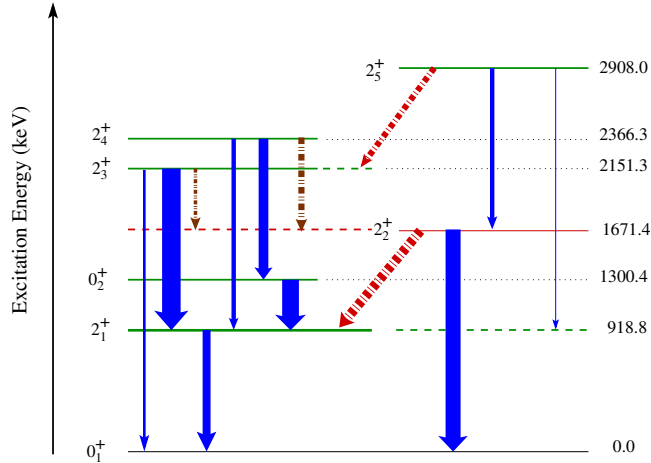


Figure 4.2: Transitions from the 2^+ states. The widths of the arrows are proportional to the transition strengths, as listed in Table 4.3. The solid-line arrows denote $E2$ transitions, while the dash-dotted arrows indicate $M1$ transitions. Dash-double-dotted arrows are used for the transitions to the 2_2^+ state with large $E2$ and $M1$ transition rates.

non-negligible $B(M1)$ value; the angular distribution did not yield a unique δ value.

In addition to the 2_2^+ state, with its $M1$ transition to the 2_1^+ state, the 2_5^+ state at 2908 keV decays to the 2_3^+ state with a $B(M1) = 0.18(2) \mu_N^2$. A new (4^+) level at 3141 keV decays to the 4_2^+ state with a very large $B(M1)$ value, $0.89_{-0.20}^{+0.24} \mu_N^2$, even larger than the $B(M1; 2_2^+ \rightarrow 2_1^+)$ value. The (1^+) level at 3200 keV, also has a considerable $B(M1)$ value, $0.18_{-0.04}^{+0.08} \mu_N^2$, for its ground-state transition. Even though these large $B(M1)$ values are usually associated with the MS states, this could not be verified, as not all of the experimental signatures for the MS states were observed.

In Figs. 4.2 and 4.3, the excited states with dominant $E2$ transitions to the 2_1^+ state are shown toward the right side of the decay schemes and can be considered as excitations built on the 2_1^+ state. Even though the $0_2^+ \rightarrow 2_1^+$ $E2$ transition is large, it could not be reproduced in shell model calculations by Holt *et al.* [71]; therefore, it could be considered as a state outside the model space used. The levels with dominant $E2$ transitions to the 2_2^+ state, considered as excitations built on the 2_2^+ state, are shown toward the right side of the decay schemes in Figs. 4.2 and 4.3. No transition is observed between the 2_2^+ and 0_2^+ states.

4.3 A Simple Interpretation

As the decay scheme of the low-lying states indicates, the ^{94}Zr nuclear structure does not fit into a simple collective vibrational picture, which might have been assumed for a nearly spherical nucleus, nor could it be entirely described by weak neutron-proton coupling as discussed in this section. A simple interpretation is presented below through a comparison

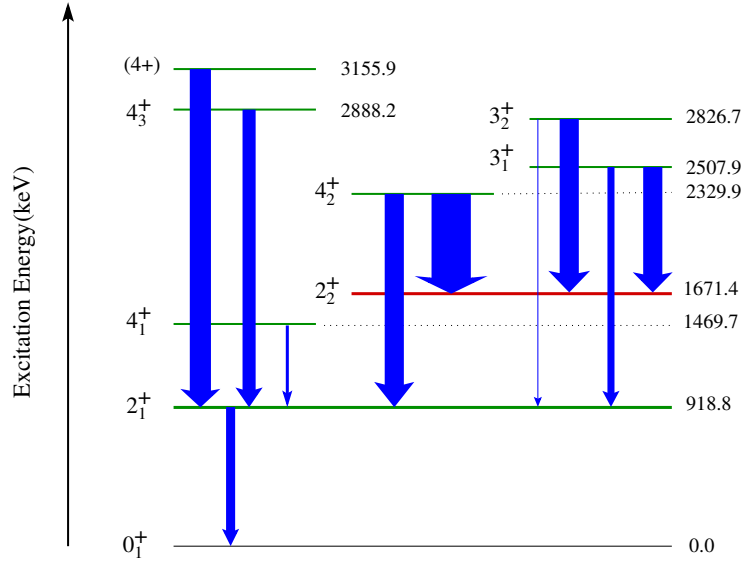


Figure 4.3: Transitions from the 4^+ and 3^+ states to the 2_1^+ and 2_2^+ states. The widths of the arrows are proportional to the $E2$ transition strengths, as listed in Table 4.3.

of ^{94}Zr to ^{92}Zr in light of the findings of this study. Also, a note is given on the comparison to ^{94}Mo , which is treated as exhibiting collective behavior.

4.3.1 Valence Nucleons

In ^{94}Zr , the valence neutrons and protons occupy the $\nu(d_{5/2})$ and $\pi(p_{1/2}, g_{1/2})$ shells, respectively, as shown in Fig 4.4. There is evidence of a subshell closure at $Z = 40$ in the Zr isotopes [20, 71, 72]. Thus one possibility for the choice of a core nucleus is ^{90}Zr . In this case, for proton excitation, breaking of the closed shell is required. In describing the ^{94}Zr spectrum, the choice of ^{90}Zr or ^{88}Sr as a core nucleus can affect model calculations, and many shell model calculations have considered ^{88}Sr as the core nucleus [73, 72, 71].

Even though $Z = 40$ is not a rigid subshell, there is evidence of its effect on the neutron-proton interactions in Zr isotopes. In ^{92}Zr the decay behavior of the 2_2^+ state at 1847.3 keV, identified as the one-phonon MS state, $2_{1,ms}^+$, could not be described with the same approach as in its neighboring isotones, i.e., ^{94}Mo and ^{96}Ru [25, 31], where ^{88}Sr had been used as the core nucleus for model calculations. Theoretical calculations revealed that the $2_{1,ms}^+$ state in ^{92}Zr is not a pure MS state [Ref. [15] and references therein]. In ^{94}Zr the anomalous 2_2^+ state at 1671.4 keV, identified as the one-phonon MS state, shows even less MS character. The question of whether there are such states in this nucleus is yet to be verified through model calculations.

The effect of the $Z = 40$ subshell closure in the Zr isotopes has been demonstrated in a shell model calculation by Holt and coworkers [71]. The experimental $^{92,94}\text{Zr}$ spectra were

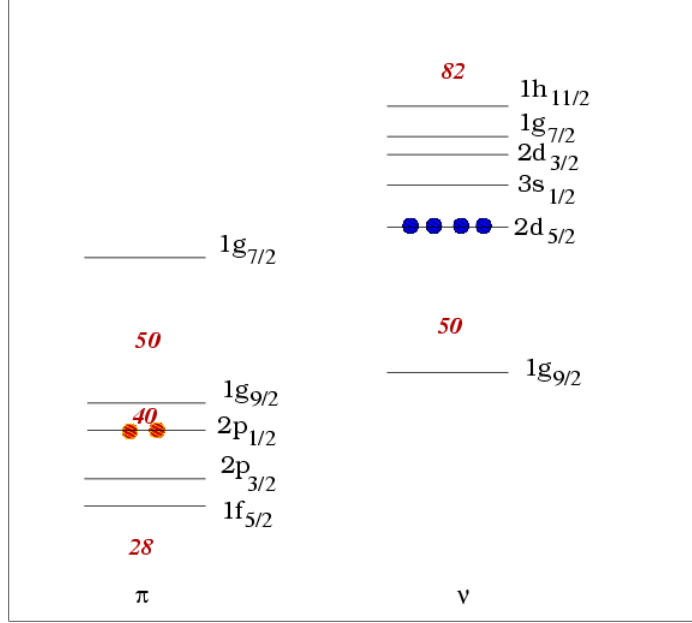


Figure 4.4: Valence proton and neutron orbitals in ^{94}Zr .

described in the neutron-proton weak-coupling scheme, where realistic effective interactions were applied to the nuclear structure of $^{90-98}\text{Zr}$ isotopes. The experimental level scheme in ^{94}Zr was thus compared with the empirical ^{92}Sr spectrum, representing the proton degrees of freedom, together with ^{90}Zr , giving the neutron degrees of freedom, as shown in Figure 4.5; this figure is an updated version of Fig.2 in Ref. [71]. The similarities between the spectra of $^{92}\text{Sr} + ^{90}\text{Zr}$ and ^{94}Zr indicate that the proton-neutron part of the effective interaction in ^{94}Zr is either weak or state-independent [71]. A similar result was obtained from a comparison of the ^{92}Zr spectrum to the empirical $^{90}\text{Sr} + ^{90}\text{Zr}$ spectra. Even though there are similarities in the level schemes, the observed decay behavior is not well represented by the weak-coupling scheme. Accordingly, in ^{92}Sr the 2_1^+ state representing the neutron excitations has $B(E2; 2_1^+ \rightarrow 0_1^+) = 8(3)$ W.u. [8], and in ^{90}Zr , the 2_1^+ state representing proton excitations, the $B(E2; 2_1^+ \rightarrow 0_1^+)$ value is 5.37(18) W.u. [8]. These results are in disagreement with the $2_1^+ \rightarrow 0_1^+$ and $2_2^+ \rightarrow 0_1^+$ $B(E2)$ values in ^{94}Zr , respectively.

As for neutrons, there is evidence of subshell closure, $N = 56$, in ^{96}Zr [20], which rapidly evolves to a shape-coexistence structure in ^{100}Zr [21]. In ^{96}Zr the first excited state, a 0^+ level at 1581 keV, along with the 2^+ state at 2225 keV and a 4^+ state at 2857 keV form a 4p-4h intruder-like band [20]. The proximity of ^{94}Zr to the subshell closures at $Z = 40$ and $N = 56$ is believed to play an important role in its nuclear structure.

4.3.2 Comparison to ^{94}Mo

Considering the $^{88}_{38}\text{Sr}_{50}$ as a core nucleus, ^{94}Zr and ^{94}Mo have the same numbers of valence nucleons: $2\pi-4\nu$ for ^{94}Zr and $4\pi-2\nu$ for ^{94}Mo . As an example of a nearly spherical

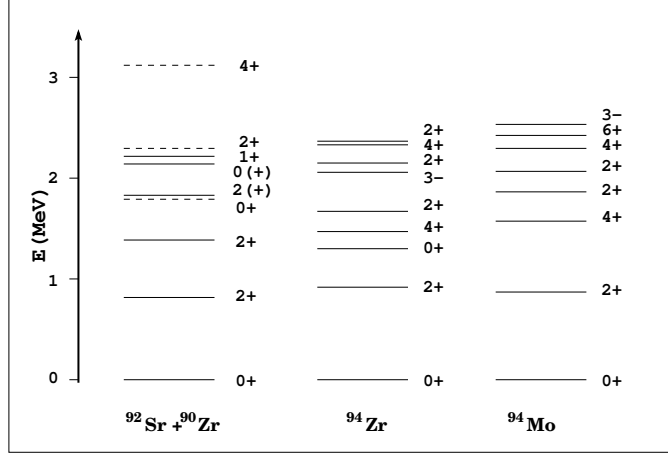


Figure 4.5: Demonstration of the weak coupling scheme for ^{94}Zr , as created from Figure.2 in Ref. [71]. On the left, dashed lines represent ^{90}Zr levels and the solid lines represent ^{92}Sr ; in the middle are ^{94}Zr levels. For comparison, the ^{94}Mo spectrum is shown on the right.

collective nucleus, ^{94}Mo has been successfully described with several collective models [30]. The experimental level scheme of these two nuclei can be compared, as shown in Figure 4.5.

The yrast states in ^{94}Mo are proton excitations [29]. For example the g-factor of the 2_1^+ state in ^{94}Mo is $+0.308(43)$ [76], indicating a dominant proton configuration, $\pi(g_{9/2})^2$, and is confirmed by shell model calculations [29]. The 2_2^+ state in ^{94}Zr is a proton excitation, as inferred from its positive g-factor. The $E2$ transition rates of these two 2^+ states to the ground state are similar. Also, another yrast state in ^{94}Mo has a similar transition rates to that of the non-yrast state in ^{94}Zr , e.g., $B(E2; 4_1^+ \rightarrow 2_1^+) = 26(4)$ W.u. in ^{94}Mo [23] and the $B(E2; 4_2^+ \rightarrow 2_2^+) = 52_{-8}^{+10}$ W.u. in ^{94}Zr . These similarities could indicate that the 4_2^+ and 2_2^+ states in ^{94}Zr are associated with the 4_1^+ and 2_1^+ states in ^{94}Mo , which have dominant proton configurations. The decay scheme of the low-lying states in ^{94}Zr , however, cannot be solely described by a collective model.

4.3.3 The 2_1^+ and 2_2^+ States; Two-Configuration Coexistence

The fact that in ^{94}Zr the transitions to the 2_1^+ and 2_2^+ states have different characteristics could be related to their different microscopic configurations. The configuration of the first 2^+ state at 918.8 keV is dominantly $\nu(d_{5/2})^4$ [71], which has been confirmed by its negative g-factor, $-0.329(15)$ [63]. In comparison, it is even more negative than that in ^{92}Zr , $-0.180(11)$ [63]. This is consistent with neutron dominance, with an increase of neutron number from 52 in ^{92}Zr to 54 in ^{94}Zr . The $B(E2; 2_1^+ \rightarrow 0_1^+) = 4.9(3)$ W.u. is too small to indicate notable collective character. The same is true for this transition in ^{92}Zr .

Most of the shell model calculations for the Zr isotopes only describe the yrast states, and there is no model calculation to determine the microscopic configuration of the 2_2^+ state in ^{94}Zr . The g-factor of the 2_2^+ state has been recently measured [74]; its positive value

indicates proton dominance of the wave function. The same conclusion was obtained from the g-factor measurements of the 2_2^+ state in ^{92}Zr [74].

In addition, two-neutron pick-up, $^{96}\text{Zr}(p, t)^{94}\text{Zr}$ [75], and two-neutron stripping [69], $^{92}\text{Zr}(t, p)^{94}\text{Zr}$ reactions show that in ^{94}Zr the 2_2^+ level at 1671 keV is not populated as strongly as the 2_1^+ state, which may indicate a difference in the neutron configuration of the 2_1^+ state versus the 2_2^+ state. A theoretical calculation for the $^{92}\text{Zr}(t, p)^{94}\text{Zr}$ reaction confirms that, indeed, the neutron configurations in these two states are different; the $3s_{1/2}$ orbit contributes more to the 2_2^+ state than to the 2_1^+ state.

Regardless of their origins, in ^{94}Zr there are two configurations to which other states decay through strong $E2$ transitions. The transitions with large $B(M1)$ values, thus, could be described as connecting the states of one configuration to the states of the other configuration. An example of that is the $2_2^+ \rightarrow 2_1^+$ $M1$ transition, which connects the 2_2^+ state, a proton dominant excitation, to a neutron excitation, the 2_1^+ state. One possible approach will be consideration of particle-hole configurations, e.g., $4p-0h(\nu)$ configuration for the 2_1^+ state, and $6p(4\nu, 2\pi)-2h(\nu)$ configuration for the 2_2^+ state. More thorough theoretical calculations are needed to test this approach.

4.4 Model Calculations

In this section results of some model calculations, i.e., shell model and IBM-2 predictions are presented and compared against the experimental data.

4.4.1 Shell Model Calculations

Shell model calculations have been fairly successful in describing the binding energies, excitation energies, and transition rates between yrast states in ^{94}Zr (Refs. [71, 72, 73, 77], and references therein). In the calculation of the $E2$ transition rates by Holt and coworkers [71], only the experimental $B(E2; 2_1^+ \rightarrow 0_1^+)$ and $B(E2; 4_1^+ \rightarrow 2_1^+)$ values could be reproduced. The calculated $B(E2; 0_2^+ \rightarrow 2_1^+)$ value was far too small; $B(E2)_{cal} = 0.01$ W.u. It was concluded that this disagreement is attributed to some collective configurations not considered in the calculations [71].

We performed new shell model calculations for ^{94}Zr with the Oxbash shell model code [78], using the $V_{low k}$ effective interaction, as described in detail in Ref. [79]. Similar calculations have been carried out successfully in MS findings for ^{93}Nb [28], ^{92}Zr , and ^{94}Mo [79]. The starting point for these calculations is the low-momentum nucleon-nucleon interaction $V_{low k}$ [81]. Ultimately derived from NN scattering data, $V_{low k}$ is an energy and model independent interaction whose only free parameter, the momentum cutoff Λ , is fixed at 2.1 fm^{-1} .

The single-particle energies are listed in Table 4.5, which also shows the model space based on ^{88}Sr as the inert core. The model space used for protons and neutrons are: $\pi[2p_{1/2}$,

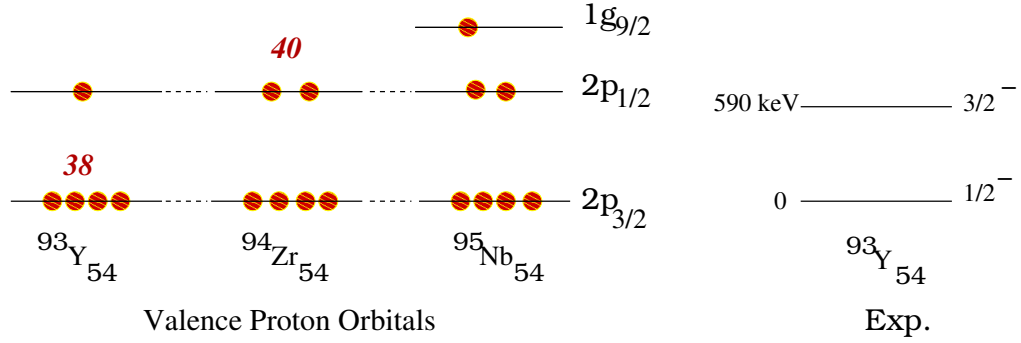


Figure 4.6: Valence proton orbitals in $N = 54$ isotones, ${}^{93}_{39}\text{Y}$, ${}^{94}_{40}\text{Zr}$, and ${}^{95}_{41}\text{Nb}$. The experimental first excited state in ${}^{93}_{39}\text{Y}$ is also shown, which has been used to determine the $\pi(p_{1/2})$ single-particle energy.

$1g_{9/2}$, $1g_{7/2}$, $2d_{5/2}$, $2d_{3/2}$, $3s_{1/2}$] and $\nu[1g_{7/2}$, $2d_{5/2}$, $2d_{3/2}$, $3s_{1/2}$, $1h_{11/2}]$. For valence protons, the $p_{1/2}$ single-particle energy was determined according to the first excited state in ${}^{93}_{39}\text{Y}_{54}$, as shown in Figure 4.6. This value is higher than that used for the $N = 52$ isotones, as is explained below. The other single-particle energies were optimized to fit the experimental spectra of ${}^{90}\text{Zr}$ and ${}^{90}\text{Sr}$.

The results of the calculations for the excitation energies of the low-lying states of ${}^{94}\text{Zr}$ are presented in Figure 4.7, which indicates good correspondence between the experimental and calculated excitation energies, with the exception of the 0_2^+ state, with a 700 keV difference between the experimental and calculated results. The $M1$ and $E2$ reduced transition strengths were also calculated, and compared to the experimental data. A brief description of these operators are given at the end of this section.

Table 4.5: The single-particle energies (s.p.e) used for ${}^{94}\text{Zr}$ shell model calculations

π	$(1p_{1/2})$	$(1g_{9/2})$	$(1g_{7/2})$	$(2d_{5/2})$	$(2d_{3/2})$	$(3s_{1/2})$
$E_x(\text{MeV})$	-6.471	-6.162	2.500	2.500	2.500	2.500
ν	$(1g_{7/2})$	$(2d_{5/2})$	$(2d_{3/2})$	$(3s_{1/2})$	$(1h_{11/2})$	
$E_x(\text{MeV})$	-4.885	-6.358	-4.350	-5.326	-3.300	

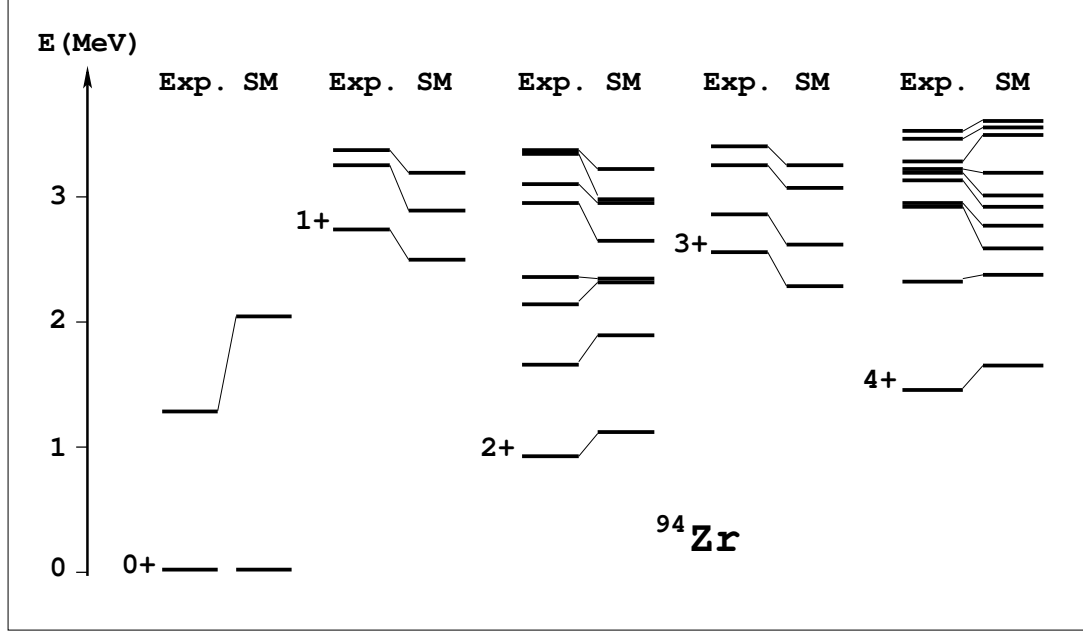


Figure 4.7: The experimental and shell model calculation results for the low-lying excited states of ^{94}Zr .

The calculated results for some of the transition strengths are listed in Table 4.6. The parameters used are $e_p^{eff} = 1.5e$, $e_n^{eff} = 0.5e$, $g_p^l = 1$, $g_s^l = 0$, and the g^s quenching factor of 0.7. The effective charges were determined to reproduce the experimental $B(E2; 2_1^+ \rightarrow 0_1^+)$ transition, but could not reproduce the experimental $B(E2; 2_2^+ \rightarrow 0_1^+)$ value. The $B(E2)$ values are governed by the effective charges, while the spin g factors affect the $B(M1)$ values. Better agreement with the experimental $B(M1; 2_2^+ \rightarrow 2_1^+)$ value was achieved by changing the $\pi(p_{1/2})_{s.p.e}$ from -7.071 MeV to -6.471 MeV, which pushes the $p_{1/2}$ subshell to within 300 keV of the $g_{9/2}$ shell. The result of the former value was $B(M1; 2_2^+ \rightarrow 2_1^+) = 0.025 \mu_N^2$. Raising the $\pi(p_{1/2})$ single-particle energy closer to the $\pi(1g_{9/2})$ indicates that $^{88}\text{Sr}_{50}$ is a better choice of core nucleus for ^{94}Zr than ^{90}Zr . The effect of different choices of effective charges on some $B(E2)$ values are listed in Appendix C in Table C.1. The shell model calculation results can be summarized as follows.

- Excitation energies are in relatively good agreement with the experimental data, as shown in Figure 4.7, except for the 0_2^+ state; *this may be an indication that the $\pi p_{3/2}$ and $\pi f_{5/2}$ contributions are accounted for adequately in the calculations.*
- It seems that the 2_2^+ , 2_3^+ and 4_1^+ , 4_2^+ states are mixed, but the shell model calculations could not reproduce the large collectivity observed in the 2_2^+ and 4_2^+ states.
- Other calculated transition strengths can be used as an alternative guide in choosing multipole mixing ratios.

The fact that our model calculations (and the previous calculations [71]) were not suc-

cessful in describing the transition strengths for the non-yrast states in ^{94}Zr could be an indicative of proton subshells other than $p_{1/2}$. The subshell closure at $Z = 40$ and proximity to the subshell closure at $N = 56$ may affect the observed decay scheme, resulting in an unusual decay scheme for this nucleus. As discussed above, it is probable that there are two distinct intrinsic excitations, the 2_1^+ and 2_2^+ states, and that other excitations are associated with one or the other, resulting in the coexistence of two configurations in ^{94}Zr . The transitions with a large $B(M1)$'s, thus, could be described as transitions from one configuration to the other. An example of that is the ($2_2^+ \rightarrow 2_1^+$) $M1$ transition, which connects a proton dominant excitation, 2_2^+ , to a neutron excitation, the 2_1^+ state.

Transition Operators

The magnetic dipole operator, $\hat{T}(M1)$, in terms of $\hat{\mu}$, the nuclear magnetic moment, can be expressed as [80]:

$$\hat{T}(M1)_\mu = \sqrt{\frac{3}{4\pi}} \left(\frac{e\hbar}{2Mc} \right) (\hat{\mu}) \quad (4.4.1)$$

where $(\frac{e\hbar}{2Mc}) = \mu_N$ is the nuclear magneton, and $\hat{\mu}$ is given by [80]:

$$\hat{\mu} = \frac{1}{2} \sum_k \{g_s^p \mathbf{s}_k + \mathbf{l}_k + g_s^n \mathbf{s}_k\} + \frac{1}{2} \sum_k \{\tau_z(k) (-g_s^p \mathbf{s}_k + g_s^n \mathbf{s}_k - \mathbf{l}_k)\} \quad (4.4.2)$$

The tensor operator can be decomposed to *isoscalar*, \mathbf{IS} , and *isovector*, \mathbf{IV} , parts. By using the g_s^{free} values for protons, $g_s^p = 5.58$, and neutrons, $g_s^n = -3.82$, the \mathbf{IS} part will be expressed as:

$$\hat{T}(M1)_{IS} = \sqrt{\frac{3}{4\pi}} \left(\frac{1}{2} \mathbf{I} + 0.38 \mathbf{S} \right) \mu_N \quad (4.4.3)$$

denotes the transition between the states with the same isospin, or $\Delta T = 0$. The \mathbf{IS} term is non-zero only for the diagonal matrix elements. The \mathbf{IV} term, using the g_s^{free} values for protons and neutron, is given by:

$$\hat{T}(M1)_{IV} = \sqrt{\frac{3}{4\pi}} \left\{ \frac{1}{2} (\mathbf{L}_p - \mathbf{L}_n) + 4.71 (\mathbf{S}_p - \mathbf{S}_n) \right\} \mu_N, \quad (4.4.4)$$

which denotes the transition between the states with different isospin, $\Delta T = 1$. The $M1$ transitions are usually dominated by the \mathbf{IV} term [80]. Detailed derivations are presented in Appendix A. In reality, the protons and neutrons are not treated as free particles, and the g_s^{free} values are reduced by a quenching factor, α_q , which represents the deviation of the nucleon contributions from that of free particles. In another words, the α_q value gives the actual g_s values, as the corresponding nucleons are contributing in the nuclear $M1$ transitions.

The $\hat{T}(E2)$ operator, which represents the electric quadrupole transition, can be expressed by [29]:

$$\hat{T}(E2) = e_p \hat{T}_p(E2) + e_n \hat{T}_n(E2) \quad (4.4.5)$$

Table 4.6: Experimental data and calculated spherical shell model results with the V_{lowk} interaction and ^{88}Sr core for some of the low-lying states in ^{94}Zr ; $e_p^{eff} = 1.5e$, $e_n^{eff} = 0.5e$, $g_p^l = 1$, $g_s^l = 0$, and a g^s quenching factor of 0.7 ($g_p^{s,free} = 5.58$ and $g_n^{s,free} = -3.82$).

J_i	J_f	$B(M1)_{Exp}$ (μ_N^2)	$B(E2)_{Exp}$ (W.u.)	$B(M1)_{SM}$ (μ_N^2)	$B(E2)_{SM}$ (W.u.)
2_1^+	0_1^+		4.9(3)		5.5
4_1^+	2_1^+		0.879(23)		0.4
2_2^+	0_1^+		7.8(7)		2.8
	2_1^+	0.31(3)	0.18(2)	0.08	0.01
2_3^+	0_1^+		0.04(3)		2.9
	2_1^+	$0.05^{+0.02}_{-0.01}$	11(3)	0.16	0.3
	2_2^+	$0.07^{+0.04}_{-0.03}$	7_{-3}^+	0.16	1.1
2_4^+	2_1^+		$1.6^{+0.5}_{-0.4}$		2.4
	0_2^+		6(1)		0.2
	2_2^+	$0.18^{+0.03}_{-0.02}$	1.02(15)	0.002	1.0
4_2^+	2_1^+		20_{-2}^{+3}		7.7
	2_2^+		50_{-8}^{+10}		2.0
2_5^+	0_1^+		0.14(3)		0.2
	2_1^+		$0.4^{+0.2}_{-0.1}$		0.1
	2_2^+		1.7(2)		0.1
	2_3^+	0.18(2)	0.34(5)		0.8

where e_ρ , ($\rho = n$ or p) are the effective quadrupole charges, and $\hat{T}_\rho(E2) = \sum_i (r_i)^2 Y_2(\theta_i^\rho, \phi_i^\rho)$, where Y_2 are spherical harmonics. Again, the $\hat{T}(E2)$ tensor operator can be decomposed into **IS** and **IV** terms, and the observed $E2$ transitions are usually of **IS** character.

$$\hat{T}_{IS}(E2) = \left(\frac{e_p + e_n}{2}\right) [\hat{T}_p(E2) + \hat{T}_n(E2)] \quad (4.4.6)$$

$$\hat{T}_{IV}(E2) = \left(\frac{e_p - e_n}{2}\right) [\hat{T}_p(E2) - \hat{T}_n(E2)] \quad (4.4.7)$$

4.4.2 IBM-2 Results

In the vibrational U(5) limit of the IBM-2, the reduced $M1$ strength for the $2_{ms}^+ \rightarrow 2_1^+$ transition is given by [82]:

$$B(M1; 2_{ms}^+ \rightarrow 2_1^+) = \frac{3}{4\pi} (g_\nu - g_\pi)^2 \frac{6N_\nu N_\pi}{N^2} \mu_N^2 \quad (4.4.8)$$

where N_π and N_ν are the number of proton and neutron pairs, respectively, and $N = N_\pi + N_\nu$. The standard boson g -factors are $g_\pi=1$ for proton bosons and $g_\nu=0$ for neutron bosons, in contrast to the values employed in fermion-based models, as described in Section 4.4.1. Considering $^{88}\text{Sr}_{50}$ as the inert core, the proton and neutron boson numbers for ^{94}Zr are $N_\pi=1$ and $N_\nu=2$, giving $B(M1; 2_{ms}^+ \rightarrow 2_1^+) = 0.32 \mu_N^2$, which is in very good agreement with our experimentally determined value of $0.31(3) \mu_N^2$.

One can also compare the experimental values, $B(E2; 2_1^+ \rightarrow 0_1^+) = 4.9(3)$ and $B(E2; 2_{ms}^+ \rightarrow$

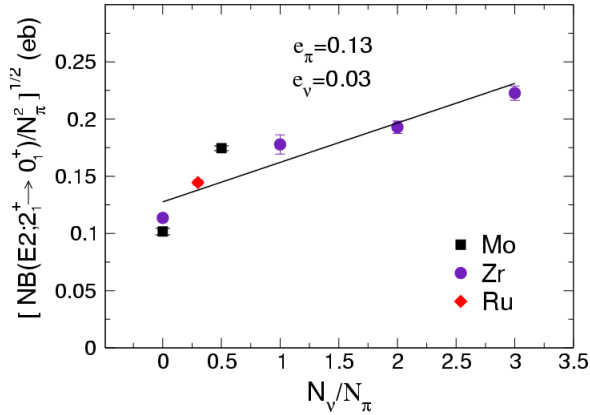


Figure 4.8: The least-squares fit for the plot of $[NB(E2; 2_1^+ \rightarrow 0_1^+)/N^2]^{1/2}$ against N_ν/N_π gives the boson proton (intercept) and neutron (slope) effective charges. $B(E2; 2_1^+ \rightarrow 0_1^+)$ data are taken from the national nuclear data center (NNDC) [8].

$0_1^+)=7.8(7)$ W.u., with the predictions from the U(5) limit [82] given by Eqns. 4.4.9 and 4.4.10, respectively,

$$B(E2; 2_1^+ \rightarrow 0_1^+) = \frac{(e_\nu N_\nu + e_\pi N_\pi)^2}{N} e^2 b^2 \quad (4.4.9)$$

and

$$B(E2; 2_{ms}^+ \rightarrow 0_1^+) = (e_\nu - e_\pi)^2 \frac{N_\nu N_\pi}{N} e^2 b^2 \quad (4.4.10)$$

The $B(E2)$ value in the latter equation depends on the difference of boson effective charges, $e_\nu - e_\pi$, and, therefore, it may be expected to be small. We have calculated the boson effective charges for the region of interest, from Zr to Ru, using the same formalism as in Ref. [83]. From Eq. [4.4.9], the plot of the quantity $[NB(E2; 2_1^+ \rightarrow 0_1^+)/N^2]^{1/2}$ versus N_ν/N_π should be linear, giving e_π (intercept) and e_ν (slope) as the fitting coefficients, i.e.,

$$[NB(E2; 2_1^+ \rightarrow 0_1^+)/N^2]^{1/2} = e_\pi + e_\nu N_\nu/N_\pi \quad (4.4.11)$$

As shown in Figure 4.8, the least-squares fit to the data gives $e_\nu = 0.03$ and $e_\pi = 0.13$, and $B(E2; 2_1^+ \rightarrow 0_1^+) = 4.7$ W.u. for ^{94}Zr . Again, the IBM-2 prediction is in excellent agreement with the experimental value. For the 2_{ms}^+ state to ground-state transition, we obtain $B(E2; 2_{ms}^+ \rightarrow 0_1^+) = 2.6$ W.u. using the effective charges calculated in this work. Recent quasiparticle phonon model (QPM) calculations have shown the proton dominance of the 2_{ms}^+ state in ^{92}Zr [32]. Similar decay properties of the 2_{ms}^+ state in ^{94}Zr might indicate that the extra collectivity in the E2 strength comes from proton core excitations not included in the IBM-2.

CHAPTER 5: CONCLUSION AND FUTURE DIRECTIONS

The low-lying states in ^{94}Zr were studied with the inelastic neutron scattering (INS), the $(n,n'\gamma)$ reaction. The $(n,n'\gamma)$ singles mode measurements, including excitation function and angular distribution were performed in the University of Kentucky, and the $(n,n'\gamma\gamma)$ coincidence measurements, for the first time, at the TUNL facilities.

This study was initiated to search in ^{94}Zr for the one-phonon and multiphonon mixed-symmetry and symmetric states, which have been seen in neighboring nuclei, e.g., ^{92}Zr , ^{94}Mo , ^{96}Mo , and ^{96}Ru . The 2_2^+ state at 1671.4 keV was identified as the one-phonon MS state, but with anomalous behavior [36]. Its $E2$ transition strength to the ground state is larger than that for the $2_1^+ \rightarrow 0_1^+$ transition. *To date, this is the only known example of such behavior.* Further analysis of ^{94}Zr resulted in even more anomalies and puzzling findings. For example, the $4_2^+ \rightarrow 2_1^+$ transition has a larger $B(E2)$ value than that of the $4_1^+ \rightarrow 2_1^+$ transition.

The low-lying level scheme could not be described by a collective model, nor could it be entirely described with the proton-neutron weak-coupling scheme. There are some excited states with decay patterns suggesting they might belong to two-phonon symmetric states, e.g., 2_3^+ and 0_2^+ states, but this assignment is not conclusive. Even though the two-phonon quadrupole vibrational triplet could not be established, candidates for members of the quadrupole-octupole excitations ($2_1^+ \otimes 3_1^-$ quintuplet) were identified. There are some excited states that decay with large $B(M1)$ values to the-might-be lower symmetric excited states, but the MS assignment cannot be conclusive, as not all the required experimental signatures were observed. Therefore, a classification of the states, up to 3.15 MeV excitation energy, based on their decay patterns was established and simple interpretations were proposed. The difference in the decay patterns of the excited states populating the 2_1^+ state and those decaying to the 2_2^+ state presented an indication of some sort of configuration coexistence, possibly attributed to core excitations.

It is hard to understand the ^{94}Zr nuclear structure based only on these experimental results. One would have expected ^{94}Zr to have a relatively simple excitation spectrum, similar to its neighboring nuclei, but the results of this work do not support such a simple picture. In some respects, ^{92}Zr and ^{94}Zr have similar decay behavior, attributed to the p-n weak coupling interactions. One can postulate that the low-lying decay scheme in ^{94}Zr may indicate that the MS excitations, as they have been observed in the neighboring nuclei, do not exist in ^{94}Zr . This experimental observation raises important questions about the nature of MS states, and how p-n interactions play a role in formation of such excitations.

Simple calculations with the shell model and IBM-2 were performed. The shell model calculations, performed with code Oxbash, using the $V_{low k}$ interaction, were not successful in describing the $E2$ transition rates for the 2_2^+ and 2_1^+ states simultaneously. One possible

reason for this result could be the choice of model space for valence protons; other orbits besides the $p_{1/2}$ may contribute in the nuclear excitations.

As an extension of this study, future work will involve a study of higher spin excited states of ^{94}Zr with sensitive experimental probes, such as Coulomb excitation, and possibly identifications of collective states associated with the 2_2^+ and 2_1^+ states. Also, more extensive and detailed theoretical calculations are needed to test and verify the two intrinsic excitation picture offered here. One approach could be consideration of quasi-particle excitations, and the quasi-particle phonon model (QPM) calculation may be beneficial. The effect of the $Z = 40$ and $N = 56$ subshell closures should be considered in theoretical calculations as well.

Appendix A: MAGNETIC DIPOLE MOMENT AND $M1$ TRANSITIONS

A.1 $M1$ Operator

Protons and neutrons, as the constituents of a nucleus, are fermions with spin $\mathbf{s} = \frac{1}{2}\hbar$. Isospin, \mathbf{T} , the same as \mathbf{s} is used to distinguish between the proton, $T_z^p = -\frac{1}{2}$, and neutron, $T_z^n = +\frac{1}{2}$; these assignments are opposite in sign of those used in high-energy physics. The magnetic moment of a nucleus is defined as [80]:

$$\hat{\mu} = \langle I, M = I | \hat{\mu}_z | I, M = I \rangle \quad (\text{A.1.1})$$

where μ_z is the z-component of the vector operator $\hat{\mu}$. Therefore, the nuclear magnetic moment is the diagonal matrix element of the $\hat{\mu}_z$. The nuclear magnetic moment operator, $\hat{\mu}$, in units of the nuclear magneton, μ_N , can be expressed by:

$$\hat{\mu} = \sum_k (g_s(k)\mathbf{s}_k + g_l(k)\mathbf{l}_k) \quad (\text{A.1.2})$$

$$= \sum_k \left\{ \frac{(1 - \tau_z(k))}{2} (g_s^p \mathbf{s}_k + \mathbf{l}_k) + \frac{(1 + \tau_z(k))}{2} g_s^n \mathbf{s}_k \right\}, \quad (\text{A.1.3})$$

where $\tau_z(k)$ is the z component of the isospin Pauli matrix, $\hat{\tau}$, analogous to σ_z for spin. The isobaric spin operators are then: $\mathbf{t} = \frac{1}{2}\tau$, as given in Eqn. A.1.3. For example, the proton isospin matrix, $\begin{bmatrix} 0 & 0 \\ 0 & 1 \end{bmatrix}$, can be expressed as a linear combination of the unit matrix and the z-component of the Pauli matrices, τ_z , as shown in Eqn. A.1.4.

$$\mathbf{1} - \tau_z = \begin{bmatrix} 1 & 0 \\ 0 & 1 \end{bmatrix} - \begin{bmatrix} 1 & 0 \\ 0 & -1 \end{bmatrix} = \begin{bmatrix} 0 & 0 \\ 0 & 1 \end{bmatrix} \quad (\text{A.1.4})$$

By substituting the values, $g_s^p = 5.58$, $g_s^n = -3.82$, $g_l^p = 1$ and $g_l^n = 0$, and $\mathbf{I} = \mathbf{L} + \mathbf{S}$, where \mathbf{L} and \mathbf{S} are the total orbital and spin angular momenta, respectively, Eqn. A.1.3 results in:

$$\begin{aligned} \hat{\mu} &= \frac{1}{2} \sum_k \{g_s^p \mathbf{s}_k + \mathbf{l}_k + g_s^n \mathbf{s}_k\} + \frac{1}{2} \sum_k \{\tau_z(k)(-g_s^p \mathbf{s}_k + g_s^n \mathbf{s}_k - \mathbf{l}_k)\} \\ &= \frac{1}{2} \sum_k \{\mathbf{l}_k + (g_s^p + g_s^n)\mathbf{s}_k\} - \frac{1}{2} \sum_k \{\tau_z(k)((g_s^p - g_s^n)\mathbf{s}_k + \mathbf{l}_k)\} \\ &= \frac{1}{2} \sum_k (\mathbf{l}_k + \mathbf{s}_k) + \frac{1}{2} \sum_k (g_s^p + g_s^n - 1)\mathbf{s}_k - \sum_k \{\tau_z(k)(\frac{1}{2}(g_s^p - g_s^n)\mathbf{s}_k + \frac{1}{2}\mathbf{l}_k)\} \\ \hat{\mu} &= (\frac{1}{2}\mathbf{I} + 0.38\mathbf{S}) - \sum_k \{\tau_z(k)(4.71\mathbf{s}_k + \frac{1}{2}\mathbf{l}_k)\} \end{aligned} \quad (\text{A.1.5})$$

The magnetic dipole transition operator, $\hat{T}(M1)$, related to the magnetic moment, $\hat{\mu}$, can be expressed as a tensor operator:

$$\hat{T}(M1)_\mu = \sqrt{\frac{3}{4\pi}} \left(\frac{e\hbar}{2Mc} \right) (\hat{\mu}) \quad (\text{A.1.6})$$

where $(\frac{e\hbar}{2Mc}) = \mu_N$ is the nuclear magneton. The nondiagonal matrix elements of this operator determine the amplitudes of $M1$ transitions in a nucleus, and are dominantly of isovector character. The tensor operator can be decomposed to *isoscalar*, **IS**, and *isovector*, **IV**, parts. The **IS** part, is given by:

$$\hat{T}(M1)_{IS} = \sqrt{\frac{3}{4\pi}} \left(\frac{1}{2} \mathbf{I} + 0.38 \mathbf{S} \right) \mu_N, \quad (\text{A.1.7})$$

and denotes the transition between states with the same isospin, or $\Delta T = 0$. The **IS** term is non-zero only for the diagonal matrix elements. The first term, $\frac{1}{2} \mathbf{I}$, related to total angular momentum, does not contribute to the transition between different states. The second term is the spin contribution, which is a scalar and it is one order of magnitude smaller than the **IV** term, given by:

$$\begin{aligned} \hat{T}(M1)_{IV} &= \sqrt{\frac{3}{4\pi}} \left\{ - \sum_k \tau_z(k) \left(\frac{1}{2} (g_s^p - g_s^n) \mathbf{s}_k + \frac{1}{2} \mathbf{l}_k \right) \right\} \mu_N \\ &= \sqrt{\frac{3}{4\pi}} \left\{ \frac{1}{2} (\mathbf{L}_p - \mathbf{L}_n) + 4.71 (\mathbf{S}_p - \mathbf{S}_n) \right\} \mu_N. \end{aligned} \quad (\text{A.1.8})$$

and denotes the transition between states with different isospin, $\Delta T = 1$. $M1$ transitions are usually dominated by the **IV** term [80].

Appendix B: BACKGROUND AND ZR GAMMA RAYS

A list of all γ rays observed, $2.5 \text{ MeV} < E_x < 4 \text{ MeV}$, in the $^{94}\text{Zr}(n, n'\gamma)$ singles-mode excitation function measurements at the University of Kentucky is provided in Table B.1. The list includes all background and γ rays from other Zr isotopes contaminations in the scattering sample. The data are from the **exfplot** output file, *fname.tsh*. Some of the γ rays could not be identified; they are marked as unknown. E_x refers to the energy threshold, or E_n , incident-neutron energy, at which the γ ray first arises. The energy calibration for transitions above 2.4 MeV is not optimal. The exact energies of the γ rays are obtained from the angular distribution measurements. This list should be used only as a guide.

Table B.1: All the observed γ rays in the excitation function spectra, including background and γ rays from other Zr isotopic contaminations in the scattering sample. Those transitions observed in ^{94}Zr and reported in the NDS dataset are marked as NDS. **New, placed** are new γ rays observed in this work that were placed in the level scheme.

E_γ	(keV)	E_x (MeV)	Comments
152.3(4)		3.594	a
308.531	(067)	2.366	NDS
322.003	(086)	2.904	^{63}Cu
339.907	(089)	3.279	^{206}Pb
356.493	(084)	2.508	New, placed
380.219	(128)	3.289	^{92}Zr
381.544	(065)	1.300	NDS
386.096	(087)	1.095	^{71}Ge
479.797	(067)	2.151	New, placed
489.2(2)		3.631	a
521.742	(081)	2.735	^{27}Al
537.2(4)		3.142	b
543.486	(080)	2.873(n)	New, placed
546.863	(081)	2.698	New, placed
550.642	(065)	1.469	NDS
587.866	(068)	2.058	NDS
615.125	(091)		bg, unknown
648.7(8)		3.156	b
658.141	(070)	2.330	New, placed
694.481	(065)	2.366	NDS

Table B.1: continued

E_γ (keV)	E_x (MeV)	Comments
713.3	2.902	^{91}Zr
752.360 (065)	1.671	NDS
756.378 (078)	2.908	New, placed
768.542 (275)	2.515	^{72}Ge
792.3	2.992	^{91}Zr
811.428 (093)	3.141	New, placed
815.562 (084)	3.016	^{206}Pb
834.5	0.834	^{72}Ge
836.220 (067)	2.508	NDS
837.4(2)	3.442	a
860	2.329	a
871.589 (127)	1.471	^{74}Ge
887.268 (080)	2.945	NDS
891.3	3.077	^{90}Zr
903.5	2.398	^{90}Zr
918.660 (065)	0.918	NDS
934.	0.934	^{92}Zr
962.2	0.962	^{63}Cu
996.547 (108)	3.362	New, placed
1001.8(3)	3.059	b
1014	1.041	^{27}Al
1026.896 (076)	2.698	New, placed
1031.502 (088)	3.089	New, placed
1039.0	1.039	^{70}Ge
1065.844 (066)	2.366	NDS
1069.486 (102)	3.219	New, placed
1121.5	0.330	^{90}Zr
1132.724 (169)	2.067	^{92}Zr
1135.684 (070)	2.605	NDS
1138.983 (065)	2.058	NDS
1155.276 (075)	2.826	NDS
1161.	3.219	NDS, from ang.dis.
1226.504 (107)	3.284	New, placed
1232.516 (065)	2.151	NDS
1236.534 (079)	2.908	NDS

Table B.1: continued

E_γ (keV)	E_x (MeV)	Comments
1303.8(6)	3.361	a
1385.050 (087)	3.059	NDS
1390.967 (079)	2.861	NDS
1398.050 (081)	2.8	unknown
1403.854 (079)	2873(n)	New, placed
1411.035 (065)	2.330	NDS
1418.647 (088)	2.370	⁹⁵ Zr
1440.654 (160)		too small yield, in coin w/ 550 very weakly
1447.453 (065)	2.366	NDS
1454.147 (089)	2.9	unknown
1457.687 (086)	2.927	New, placed
1484.	3.5	unknown
1470.090 (123)	3.141	c
1559.881 (089)	3.029	New, placed
1588.916 (067)	2.508	NDS
1619.524 (098)	3.089	New, placed
1646.941 (109)	3.318	New, placed
1671.225 (065)	1.671	NDS
1672.9(7)	3.142	a
1750.499 (100)	3.219	NDS
1754.933 (096)	3.224(n)	New, placed
1778.855 (150)	2.698	⁹⁴ Zr and ²⁸ Si
1855.533 (143)	3.5	unknown
1866.034 (113)	3.336	New, placing
1891.181 (110)	3.362	NDS
1907.397 (088)	2.826	New, placed
1926.975 (089)	2.846	⁹⁴ Zr and ⁶³ Cu
1941.743 (100)	2.536	⁷⁴ Ge
1950.318 (102)	2.390	²³ Na
1954.339 (086)	2.873(n)	New, placed
1958.104 (120)		bg, unknown
1968.789 (079)	2.888	NDS
1981.365 (102)	2.9	unknown
1988.742 (066)	2.908	NDS

Table B.1: continued

E_γ (keV)	E_x (MeV)	Comments
2007.334 (155)	2.007	⁷⁰ Ge
2012.563 (100)	3.482	New, placed
2080.555 (067)	3.000(n)	New, placed
2083.401 (144)	3.553	New, placed
2092.220 (173)	3.561	New, placed
2136.802 (091)	3.056(n)	New, placed , doublet w/ 2141
2140.196 (065)	3.059	NDS
2150.389 (080)	2.151	New, placed
2185.208 (073)	2.186	⁹⁰ Zr
2221.848 (131)		H(n, γ)
2229.454 (134)	3.8	unknown
2235.929 (093)	3.155	NDS(2237)
2252.775 (180)	3.724	NDS(2255)
2280.725 (143)	3.200(n)	New, placed
2300.197 (075)	3.219	NDS
2304.830 (102)	3.224(n)	New, placed
2364.137 (110)	3.284	New, placed
2388.917 (099)	2.390	²³ Na
2398.476 (126)	3.5	unknown
2410.709 (116)	3.331	New(2412),?placing
2440.838 (122)	3.361	NDS(2442)
2490.434 (112)	3.411	NDS(2492)
2522.983 (152)	3.452	⁹² Zr
2526.446 (342)		bg, unknown
2561.911 (118)	3.7	unknown
2564.968 (098)	3.482	New, placed
2617.	3.211	⁷⁴ Ge
2632.906 (210)	3.551	New, placed
2660.664 (110)	3.578(n)	New, placed
2671.338 (178)	3.7	unknown
2678.501 (105)	3.595	New, placed
2695.731 (079)	2.698	New(2698),placed
2843.129 (083)	2.846	NDS
2904.598 (123)	2.908	NDS(2908)
3153.189 (279)	3.155	New(3155),placed

Table B.1: continued

E_γ (keV)	E_x (MeV)	Comments
3195.984 (077)	3.200(n)	New(3200),placed
3280.193 (160)	3.284	New, placed
3314.140 (113)	3.318	New, placed
3532.		bg
3547.585 (165)	3.7	c
3660.810 (210)	3.9	c
3681.284 (232)	?	c
3711.572 (244)	3.9	c

a : Reported in Ref. [34], but not observed in this work.

b : Observed, but not included. The peakshape was not acceptable for fitting.

c : Not a good peak in coincidence spectra: It could not be placed.

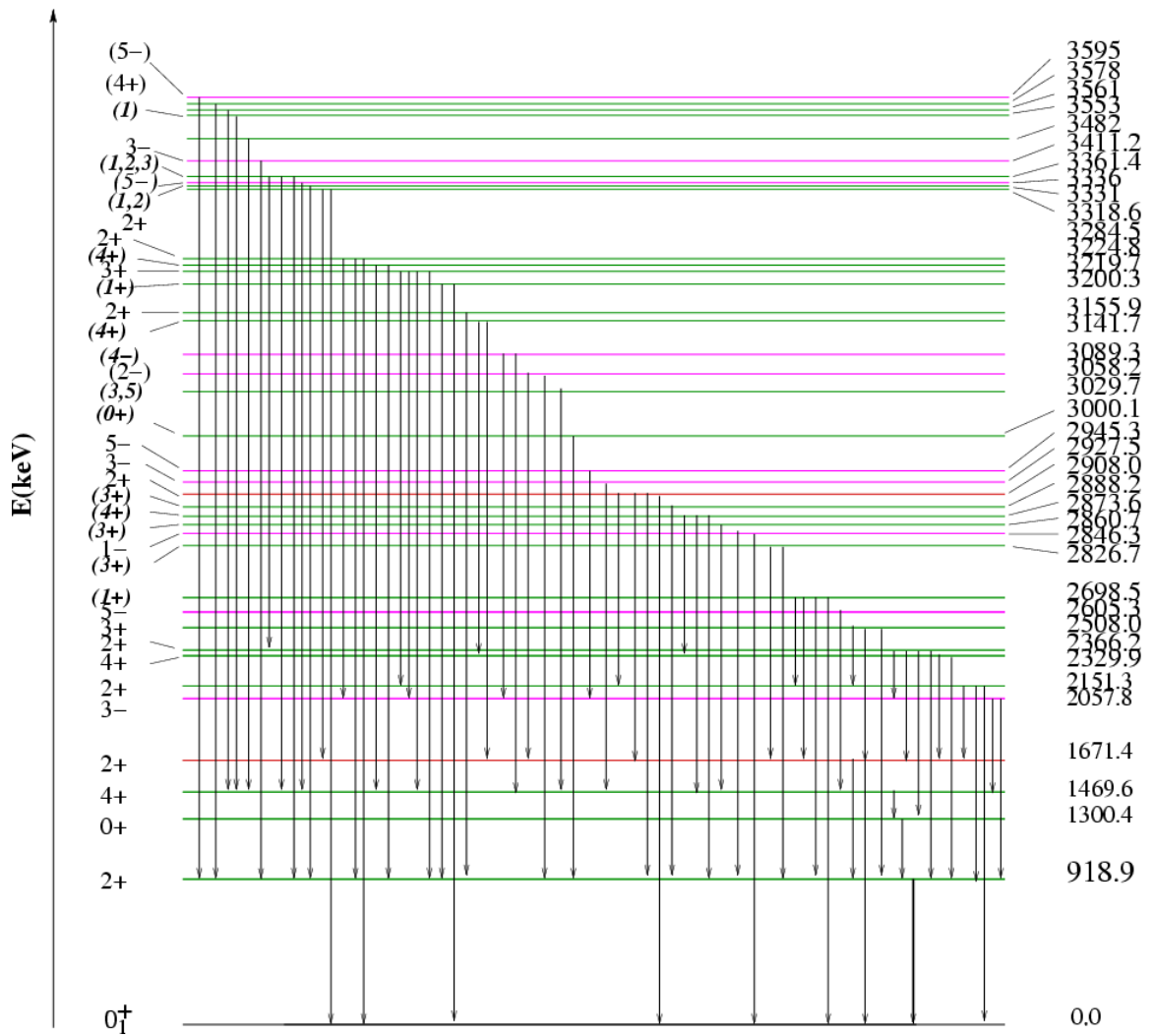


Figure B.1: ^{94}Zr Level Scheme as observed in this work

Appendix C: EFFECTIVE CHARGES IN THE SHELL MODEL

The effect of different choices of effective charges on some $B(E2)$ values are listed in Table C.1.

Table C.1: Shell model calculation results for some of the $B(E2)$ values in ^{94}Zr . The $e^p = 1.5e$ and $e^n = 0.5e$ results are best in agreement with the $B(E2; 2_1^+ \rightarrow 0_1^+)$ experimental value.

e_p^{eff}	e_n^{eff}	J_i^π	J_f^π	$B(E2) (e^2 fm^4)$	$B(E2) (W.u.)$	$B(E2)_{exp} (W.u.)$
1.8e	1.3e	4_1^+	2_1^+	30.99	1.22	0.88(2)
		2_2^+	0_1^+	419.8	16.5	4.9(11)
1.8e	0.6e	2_1^+	0_1^+	156.9	6.2	4.9(11)
1.5e	0.6e	2_1^+	0_1^+	134	5.3	4.9(11)
		2_2^+	0_1^+	60.67	2.4	7.8(7)
1.5e	0.7e	2_1^+	0_1^+	161.7	6.4	
		2_2^+	0_1^+	68.44	2.7	
1.4e	0.6e	2_1^+	0_1^+	126.8	5.0	
		2_2^+	0_1^+	55.7	2.2	
1.5e	0.5e	2_1^+	0_1^+	109	4.3	
		2_2^+	0_1^+	53.4	2.1	
		4_1^+	2_1^+	10.2	0.4	
1.6e	0.6e	2_1^+	0_1^+	141.5	5.6	
		2_2^+	0_1^+	65.5	2.6	
1.8e	1.0e	2_1^+	0_1^+	292.1	11.5	
		2_2^+	0_1^+	114.3	4.5	
1.6e	1.4e	2_1^+	0_1^+	48.26	1.9	
		2_2^+	0_1^+	38.1	1.5	

Appendix D: GAMBIT CORRECTIONS

D.1 Neutron Scattering

The corrections due to multiple scattering and absorption of the incident neutrons and absorption of γ rays in a cylindrical scattering sample were performed with a computer code, **gambit**. The geometry of the scattering sample and the detector angle affect the yields of the detected γ rays. Therefore, these corrections are crucial for angular distribution data analysis and were applied to each set of data measured at any E_n separately. The physical and chemical characteristics of the scattering sample, such as the radius and the height of the sample, its chemical formula and molecular weight, were taken as input information for the code. Other parameters were included, which are dependent on the bombarding E_n : the total (σ_{tot}) and inelastic (σ_{inel}) neutron scattering cross sections in barns, differential neutron cross sections ($\frac{d\sigma}{d\Omega}(\theta)$) at 0° and 180° in $\frac{mb}{Sr}$ and photoabsorbption cross sections for any element in the scattering sample in $\frac{barns}{atom}$. Only the details on the input file formats are well documented in other references [45]. The details on obtaining the cross sections values are discussed here.

For each element in the scattering sample, i. e., ^{94}Zr and ^{16}O in $^{94}\text{ZrO}_2$, the following was performed. The values of σ_{tot} , σ_{el} , and $\frac{d\sigma}{d\Omega}(\theta)$ were obtained from the ENDF, Evaluated Nuclear Data File, website [84] for any given E_n . In the ENDF website, for the σ_{tot} value, (n,tot) was chosen for the reaction, (MF=3, MT=1, total cross section), and for the σ_{el} value, (n,*) was chosen for the reaction, (MF=3, MT=2, elastic scattering) for a given E_n , e.g., 2.8 MeV. The σ_{inel} value was then obtained by subtracting the σ_{el} from the σ_{tot} value. The neutron differential cross section as a function of angle can be expressed as:

$$\frac{d\sigma}{d\Omega} = \sum_{l=0}^N \frac{2l+1}{2} a_l P_l(\cos\theta) = a_0 \sum_{l=1}^N \frac{2l+1}{2} \frac{a_l}{a_0} P_l(\cos\theta) \quad (\text{D.1.1})$$

where normalizing to $a_0 = \sigma_{tot}/4\pi$, the equation becomes:

$$\frac{d\sigma}{d\Omega} = \frac{\sigma_{tot}}{4\pi} [P_0(\cos\theta) + \sum_{l=1}^N (2l+1) a'_l P_l(\cos\theta)] \quad (\text{D.1.2})$$

The a'_l values were also obtained from the ENDF website at $E_n = 2.8$ MeV, (MF=4, MT=2, angular distribution cross section). If the coefficients are not available for the exact E_n , a linear extrapolation can be performed to determine the a'_l values. In the ^{94}Zr analysis, this extrapolation was performed for $E_n = 2.3$ and 3.5 MeV; the exact values were available for $E_n = 2.8$ MeV.

After obtaining the σ_{tot} , σ_{inel} , and differential neutron scattering cross sections at 0° and 180° for ^{94}Zr and ^{16}O , the cross section for the compound, $^{94}\text{ZrO}_2$, was determined by addition of the cross section value for ^{94}Zr to twice the cross section for ^{16}O , as shown below:

$$(\sigma_{inel})^{94}\text{ZrO}_2 = (\sigma_{inel})^{94}\text{Zr} + 2(\sigma_{inel})^{16}\text{O} \quad (\text{D.1.3})$$

The above mentioned parameters are used in the file *fname.gmb*, as input for the **gambit** code.

D.2 Photoabsorption

A computer code, **xcom**, provides the photoabsorption cross sections for each element separately. The output has several cross sections, from which the (*total cross section without coherent*) for Zr and O were the values taken and included in the **gambit** input file, *fname.gmb*. These values are given for a standard list of γ -ray energies, which were provided by the code **xcom**. The photoabsorption cross sections are independent of the incident neutron energy, therefore, the **xcom** output could be used for all three angular distribution data sets. If the **xcom** output for some specific γ -ray energies is required, a list of the γ -ray energies can be created. The format of such a file, e.g., *energies.txt*, is as follows:

```
16 the number of data points
6.00000E-05 8.00000E-05 1.00000E-04 1.50000E-04 2.00000E-04 3.00000E-04 4.00000E-04
5.00000E-04 6.00000E-04 8.00000E-04 1.00000E-03 1.50000E-03 2.00000E-03 3.00000E-03
4.00000E-03 5.00000E-03 , the energies are given in keV.
```

The data file can be given as the input to the **xcom** code.
Note: In the following, the \$ sign refers to the prompt command line. The dialog of each command is typed in the **Typewriter** and the user inputs in the *Italic* fonts. The phrases in (*Slanted*) are the explanation to what should be done.

\$xcom

Program XCOM, Version 3.1 M.J.Berger and J.H.Hubbell, 23 June 1999

Enter name of substance:

zr

Options for characterization of substance:

1. Elemental substance, specified by atomic number
2. Elemental substance, specified by chemical symbol
3. Compound, specified by chemical formula---*not used*
4. Mixture of elements and/or compounds

Enter choice:

1 (—*the output for one element at a time, Zr*)

Enter atomic number of element:

40

Options for output quantities:

1. Cross sections in barns/atom
2. Cross sections in barns/atom, and attenuation coefficients in cm²/g
3. Partial interaction coefficients and attenuation coefficients in cm²/g

Enter choice:

1

Options for energy list for output data:

1. Standard energy grid only
2. Standard grid plus additional energies
3. Additional energies only

Enter choice:

2

Modes of entering additional energies:

1. Entry from keyboard
2. Entry from prepared input file

Enter choice:

2

Specify file that contains input energy list.

(Specification can include drive and path):

energies.txt

Specify file on which output (cross section table) is to be stored.

(Specification can include drive and path):

ZR

Cross-section table with headings has been stored in file *ZR*

Options for further output:

1. No more output
2. Selected arrays stored on disk

Enter choice:

1

Calculation is finished.

The output is written in *ZR*, which is a text file. The code produces another output file *xcom.short_output*, which is not used.

Appendix E: SPIN ASSIGNMENTS FROM EXCITATION FUNCTIONS

In order to determine a level cross section, the feeding and decaying γ -ray transitions should be known. The following describes the main steps.

- The γ -ray yields need to be corrected for neutron attenuation, multiple scattering, and γ -ray attenuation.
 - Photoabsorption corrections are obtained by **gambit**
 - Neutron attenuation corrections were obtained by plots of σ_{inel} vs. E_n , made by **gle** graphical software.
- The theoretical cross sections for each level, any J^π , are obtained by the computer codes **CINDY** and **cinexf**.
- The experimental and theoretical cross section data, for each level, are plotted together in **gle** for comparisons.

E.1 Gambit and Photoabsorption Corrections

The photoabsorption correction, *photoabs*, for a range of E_γ 's, was obtained from the **gambit** program output, specifically the factors in *fname.log* corresponding to each E_γ . The details of the **gambit** input files, for angular distribution data, are described in [45] and Appendix D. The input file, *gambit.inp*, slightly differs from that of angular distribution data. It should be noted this correction is mostly important for the low-energy γ rays, i.e., $E_\gamma < 1$ MeV.

The *gambit.inp* file, written as a text file, looks like:

```
35Zr.gmb (this file contains the physical and photoabsorption cross section parameters.)
1 (Number of detection angles)
90 (Detection angle)
17 (Numbers of  $\gamma$  rays)
50. (list of  $E_\gamma$  rays in keV)
60.
80.
100.
150.
200.
300.
400.
```

500.
 600.
 800.
 1000.
 1500.
 2000.
 3000.
 4000.
 5000.

For the ^{94}Zr data, the correction factors were obtained from the $E_n = 3.5$ MeV **gambit** output, i.e., *35Zr.log*. The *35Zr.log* file was in this format:

```

1 angles
  90.0
17 energies
  50.0      60.0      80.0      100.0     150.0     200.0
 300.0     400.0     500.0     600.0     800.0    1000.0
1500.0    2000.0    3000.0    4000.0    5000.0

  90.0      50.0      76.06495
  90.0      60.0      45.92745
  90.0      80.0      23.24671
  90.0     100.0     16.01456
  90.0     150.0     11.30605
  90.0     200.0     10.23676
  90.0     300.0      9.87119
  90.0     400.0      9.75504
  90.0     500.0      9.71617

```

90.0	600.0	9.32872
90.0	800.0	9.69282
90.0	1000.0	9.73091
90.0	1500.0	9.78340
90.0	2000.0	9.11636
90.0	3000.0	9.08253
90.0	4000.0	9.06957
90.0	5000.0	9.06141

The last two columns are taken as data points in the *photoabs.dat* file for E_γ vs. *photoabs* plot constructed in **gle**. These data could be normalized to the factor at the highest E_γ in the above table. In ^{94}Zr case data were normalized to the value at $E_\gamma = 1500$ keV; the corrections for higher energies is not crucial. A best-fit line to the data was determined by *photoabs.gle*, and the output plot is an *.eps* file, shown in Figure E.1. The corrections are made by multiplying the γ -ray yields by the correction factor, which is obtained from $F(x) = 8.5 * \exp(-0.024 * x + 0.2) + 1.10$, where x is E_γ . As mentioned, this factor becomes 1 for high-energy γ rays.

The *photoabs.gle* file:

```
size 20 15

!a = 1000; b = -10

begin graph
  xtitle "E_{\gamma} [MeV]" hei 0.75 dist 0.3 font rm
  ytitle "photonabs." hei 0.75 dist 0.3 font rm
  title "F(x) = 8.5*exp(-0.024*x+0.2)+1.10" hei 0.8 dist 0.3 font rm
  xaxis min 0 max 1500 font rm
  xlabel font rm hei 0.75
  yaxis min 0.5 max 7 font rm
  ylabel font rm hei 0.75
  data "diss.dat"
```

```

d1 marker square msize 0.4 color blue
let d2 = 8.5*exp(-0.024*x+0.2)+1.10 from 20 to 1500
d2 line color red
end graph

```

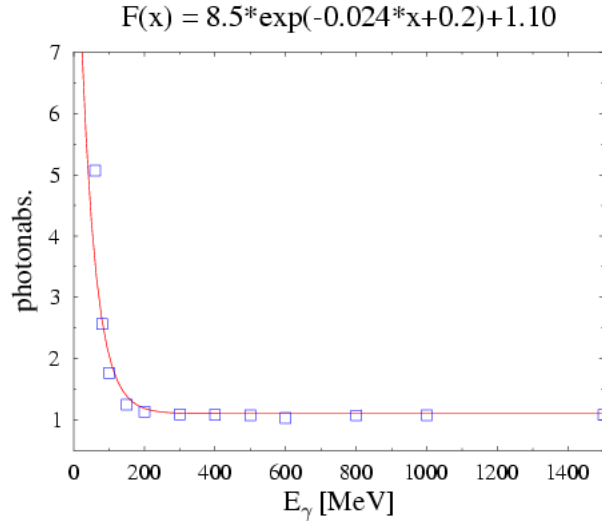


Figure E.1: Photoabsorption plot for ^{94}Zr as plotted in **gle**. The corrections are made to the γ -ray yields in the excitation function data.

E.2 Inelastic Neutron Scattering Corrections

The INS cross sections, σ_{inel} , for $^{94}\text{ZrO}_2$ in this case, were obtained as described in Appendix D. The curve fitted to the data was in the form of $F(E_n) = 1.664 + (0.14643)\log(E_n)$, where E_n should be replaced with E_{level} when it is used as a multiplication factor to the data in the final plot. The σ_{inel} vs. E_n plot was created in **gle**. The data can be modified in the input file, *fname.gle*, as described in the **GLE** manual [85].

E.3 Theoretical Cross Sections

The theoretical cross sections for a level, for different J^π , were obtained from the computer code **CINDY**. The input-file descriptions can be found in [45, 54]. The optical potential parameters used for ^{94}Zr were: the real parts, $V_0=47$ MeV, $V'_0=-0.27$, and the imaginary parts, $W_0 = 9.00$ MeV and $W'_0 = 0$. The second-order parameters, V''_0 and W''_0 , were zero. The radius and diffusion parameters were: $r_0=1.215$, $a = 0.658$, $r'_0 = 1.264$, $a'_0 = 0.524$. V_{so} is a function of incident neutron energy, E_n , through Eqn. E.3.1, with parameters, $v_{so1}=6.2$ MeV, $v_{so2} = 0.004/\text{MeV}$, and $E_f = -7.34$ MeV. The same parameters were

used for **CINDY** angular distribution inputs, Section 3.4.

$$V_{so} = v_{so1} \exp(-v_{so2}(E_n - E_f)) \quad (\text{E.3.1})$$

For excitation function data, the **CINDY** input file is different from those for angular distribution analysis. **CINDY** can be run for several input files, separately, and then the outputs put in one file. It should be noted that a knowledge of level density of any J^π is important. If, for example, the number of $J^\pi = 2^+$ states in a certain energy range, e.g., 3.5 - 4 MeV are not known, the calculated cross sections for any 2^+ level in that energy range will be affected, and this could result in an unreliable comparison between the experimental and theoretical cross sections to assign a spin to a level. This issue could be addressed, either by including a function for the level density, or choosing the spins to the best knowledge, e.g., based on $J \otimes J$ couplings.

A computer code, written in C by B. Crider, **cinexf**, sorts the calculated cross sections, from *fname.cex* file, for each level and J^π into the *fname.dat* files. A list of spins, *spin.list* file, which is a simple text file, where spins in range of $-6.0 < \pi J < +6.0$ are listed in one column. This file should be in the same directory as the **cinexf** code is compiled and would be executed.

```

$ ./cinexf Enter the name of the file you wish to convert (example: 50.cex)
zr.cex

```

```

Enter the energy level (in x.xxx MeV) or enter 0 if you do not wish to continue
0.918 — (the level energy as it exactly appears in the zr. cex file)

```

```

Enter the energy level (in x.xxx MeV) or enter 0 if you do not wish to continue
1.300

```

```

Enter the energy level (in x.xxx MeV) or enter 0 if you do not wish to continue
0

```

The outputs are: 918_0.dat–918_60.dat, and 1300_0.dat–1300_60.dat, for $E_{\gamma-J}$ and $E_{\gamma--J}$, as were listed in the *spin.list* file.

E.4 Spin Assignments

The experimental differential cross section of a level is obtained from $Y_{decaying} - Y_{feeding}$, where Y is the corrected γ -ray yield for each transition at each E_n . The INS corrections are applied as a multiplication factor to the Y_{exp} with a formula shown below in the *fname.gle* file. A final normalization factor for the cross sections was obtained from normalizing the data for a state with a well-known J^π to that of the theoretical cross sections. This factor may be an average of the normalizations of several levels to their theoretical curves. The normalization of the 2508-keV level to the theoretical curve for $J^\pi = 3^+$ was used for normalizing the data in ^{94}Zr .

Figure E.2 shows a plot of experimental cross section for a level at $E_L=2508$ keV obtained from excitation function data along with the theoretical curves for different spins. The *2508.gle* file is shown below. The command **gle 2508.gle** creates the *2508.eps* file.

```

size 40 30

begin translate 0. 0.
begin scale 1. 1.

amove 0.15 7.5
set hei .45
begin rotate 90
begin text
\sethei{0.65}
end text
end rotate

amove 5 17.5
begin text
\sethei{1}
end text

amove 2.5 2
begin graph
  size 22 20
  fullsize
  nobox
  title "E_L=2508 keV"
  xtitle "Neutron Energy [MeV]" hei 1.0 dist 0.5 font rm
  xaxis min 2.4 max 4.1 font rm
  ytitle "mBarn" hei 1.0 dist 0.5 font rm
  yaxis min 0 max 120 font rm
  xlabel font rm hei 1.0
  ylabel font rm hei 1.0
  data 836_jg.exf d1 d2 (! E_g.exf has the un-corrected peak areas)
  data 1589.exf d3 d4
  data 356_jg.exf d20 d21
  let d5 = 0.257*(d1+d3+d20)*(1.664+0.14643*log(2.508))

```

```

let d6 = (d2*d2+d4*d4+d21*d21)
let d7 = 0.257*sqrt(d6)
! let d5 = d1+d3 ---- (!: to comment a line)
d5 marker triangle msize 0.4 err d7 color black
data 2508_30.dat d8
  d8 marker square msize 0.4 color red
  d8 smooth
data 2508_20.dat d9
  d9 marker circle msize 0.4 color blue
  d9 smooth
data 2508_40.dat d10
  d10 marker diamond msize 0.4 color green
  d10 smooth

end graph
end scale
end translate

```

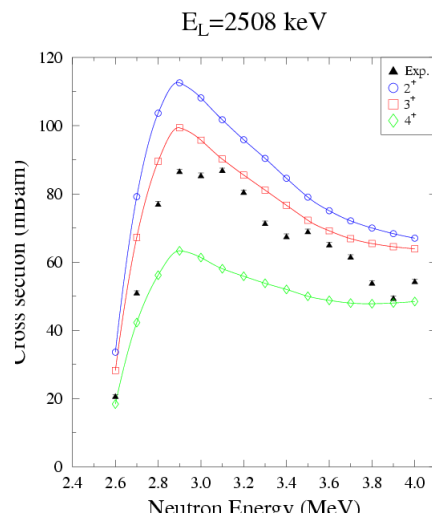


Figure E.2: Excitation function CINDY plot; cross section plot for a level at $E_L=2508$ keV, $J^\pi = 3^+$. The curve with circles is the CINDY output for $J=2$; the squares are for $J=3$ and the diamonds for $J=4$. $J^\pi = 3^+$ can be confirmed.

Appendix F: DETAILS OF TUNL γ - γ COINCIDENCE DATA ANALYSIS

F.1 SpecTcl Software Modifications

The spectra created in `SpecTcl`, e.g., a matrix for coincidence data could be written in NSCL ASCII or BINARY formats. In order to analyze the matrix, translation of these formats to any of the available formats for data analysis at UK was necessary. It was soon realized that this process is very involved and we looked for other options. Dirk Weisshaar from MSU/NSCL had expanded the `SpecTcl` formatter devices to include the `lc`, line compressed format of `Tv`, in the `swrite` command in the `SpecTcl`. In this chapter, the details of the instructions on software and program modifications for building a matrix in `SpecTcl` and writing it in `Tv` format are discussed. This instructions are to include `Tv` format into the `SpecTcl` version used at TUNL at the time of the experiment, March 2006, version 3.1. A newer version of `SpecTcl` has been developed. Ron Fox at MSU is the person in charge of `SpecTcl` development group.

1. `ClcSpectrumFormatter.h` is the additional header file to be included in the `MySpecTclApp.cpp` file. It was placed as the last file in the `include` list. Other standard header files were:

`config.h`, `Globals.h`, `MySpecTclApp.h`, `EventProcessor.h`, `TCLAnalyzer.h`,
`Event.h`, `TreeParameter.h`, `CFitFactory.h`, `CLinearFitCreator.h`,
`CFitCommand.h`, `CCalibratedParameterCommand.h`, `CCalibratedParameterManager.h`,
`MultiTestSource.h`, `CalibrationDistribution.h`, `TCLVariable.h`, `TCLProcessor.h`,
`TCLResult.h`, `SpecTcl.h`, `FilterEventProcessor.h`.

2. The new formatter is included in "`CMySpecTclApp::CMySpecTclApp ()`" object, in the `MySpecTclApp.cpp` file. `#` is used as comment line.

(`# Constructors, destructors, and other replacements for compiler cannonicals:`)

```
static ClcSpectrumFormatter lcSpectrumFormatter;
CMySpecTclApp::CMySpecTclApp ()
{
CSpectrumFormatterFactory::AddFormatter("lc", &lcSpectrumFormatter);
}
(# Destructor: )
CMySpecTclApp:: CMySpecTclApp ( )
{
}
```


3. The *ClcSpectrumFormatter.h* and its additional sources, *mfile.h* and *libmfile.a*, were included in the standard paths for **SpecTcl** installation. Copies of *mfile.h* and *ClcSpectrumFormatter.h* can be found in the proper directories, in the *eelhami* home directory (for UK users).

4. In **SpecTcl Makefile**, linking the *mfile* library was done by **-lmfile** in **USRLDFLAGS = ...**

5. The **SpecTcl** was reinstalled by normal **make clean** and **make** commands to incorporate the **Tv** formatter.

A note for the UK research group: The modified **SpecTcl** software was installed on home directories of the *vdgpc6* and *vdgpc7* desktop computers, by Brian Doyle, our network administrator at the time.

F.2 SpecTcl

The **SpecTcl** code is run in the directory in which it has been compiled. It is executed by typing **./SpecTcl** in the prompt command line. Three windows are displayed: **Xamine**, **SpecTcl (with TUNL logo)** and a **Tk Con 1.6 SpecTcl** console, where the **SpecTcl** commands can be executed. For example, in the *tcl* console, the command **source** is used to upload any *.tcl* script. It should be executed in the directory where the *.tcl* script is written.

The command **source spectecl_uk.tcl** uploads the *.tcl* script, where all histograms and gates were defined. In order to upload the events, i.e., data files with a *.evt* extension, the prompt directory should be the same as where the *event* files reside. For convenience and easier access, all the event names can be written in a *.tcl* file, e.g., *runs.tcl*. The format is specific, one name after another in a horizontal line, such as:

```
attach -pipe cat run1313-4096.evt run1314-4096.evt run1315-4096.evt ...
```

In the *tcl* console the command **source runs.tcl** prints the list of the events, in the *runs.tcl* file. The replay, or incrementation, of the data is done by the command **start**. This process should not be interrupted by any other commands in the console; it will stop! The defined spectra can be displayed on the *Xamine* graphical window. In *Spectrum* choose *Display Spectrum* on the *Xamine toolbar*, and any histograms defined in the *spectecl_uk.tcl* file can be selected. Several spectra can be displayed by changing the number of windows in the *Geometry*, on the **Xamine** window, and loading spectra in any desired window.

A matrix, or any histogram, can be written in *lc* format to be analyzed in **Tv** by: **swrite -format lc fname.mtx sname**,

where *fname* is the name of the file to be written; it can be *fname.spe* for 1-d spectra. *sname* is the name of the histogram, exactly as defined in *spectecl_uk.tcl*; *sname* is case sensitive.

Dirk Weisshaar also provided the *mattools.c* along with its *Makefile* and *mfile.h*. The **matproj** command creates *X* and *Y* projections of a matrix. For example **matproj**

test.mtx creates **test.prx** and **test.pry**. It was a very fast process! If the **SpecTcl** would have been in C++, the incrementation time of the spectra would have been much shorter; using the scripted **SpecTcl** generally took about two hours for the all the event files to be incremented.

F.3 Coincidence Data Analysis Using Tv

The coincidence data were analyzed on **Tv**. A user-defined file, e.g., *getmat*, was used to load a matrix and a calibrated X projection spectrum. The *getmat* file has the necessary commands for creating cuts:

```
cut activate 0
cut attach matrix 0
cut matrix attach-projection 0
cut attach spectrum 1
cut attach directory 1
cut directory open 1 /tmp_mnt/home61/phy/eelhami/94Zr/Coin
/matrecies/shveto
cut matrix open 0 /tmp_mnt/home61/.../shveto/fname.mtx
spectrum read /tmp_mnt/home61/.../shveto/fname.prx 0
calibration position read energy.cal
```

The directory path given in **cut directory open** is where the created cuts will be written. The name and the path for the *matrix* is given in **cut matrix open**. The projection spectrum is defined by its path and name in the **spectrum read** line. A calibration file is given by **calibration position read**, when the projection spectrum is not calibrated. These are the standard **Tv** commands, [51].

A *cut* was defined by choosing a window of a few channels at the photopeak of interest, and a window with an equal number of channels in the background close to the photopeak by using the hotkey *c*. The *cut* is created by the *C* hotkey. A hotkey is a functional letter on the keyboard when the **tv_root** window is active. The hotkeys are replaced by the written commands in the **Tv** console. For example, the *cut* command could be written as **cut write cut** in **Tv** prompt command line [51]. The hotkeys of Nn , displays a new window, or Np , displays the previous window, can be used to toggle between the *projection* and the *cut* spectra. A graphical figure of a spectrum, in **Xfig** format, can be created by **window plot create xfig fname.fig**.

F.4 Spectra Construction .tcl Script, spectcl_uk.tcl

spectcl_uk.tcl is the *tcl* script used to build the matrix for the ^{94}Zr coincidence data in **SpecTcl**. The original script was written by John Kelly at TUNL. I made some modifica-

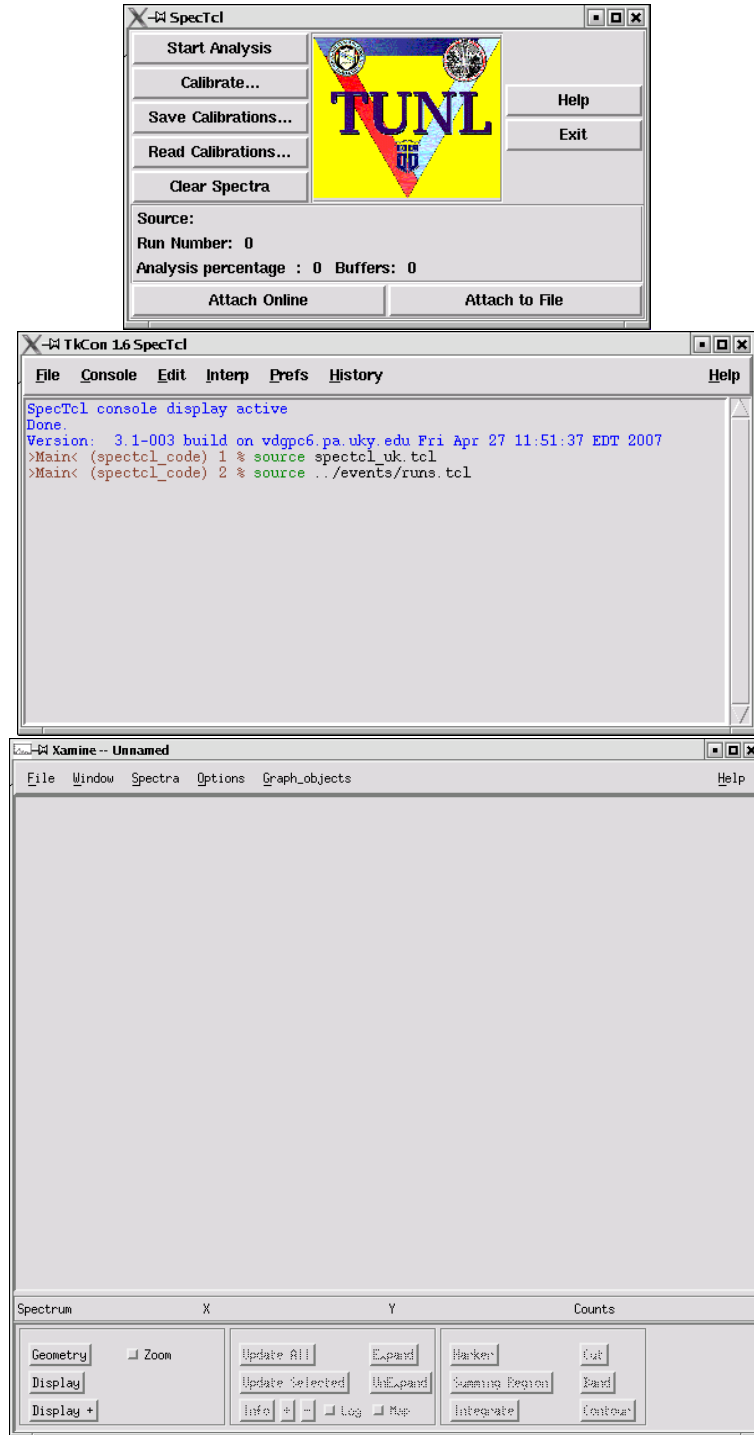


Figure F.1: SpecTcl environment: The top panel is the SpecTcl logo window to monitor the replay of data. The middle panel is the Tk Console, where commands, e.g., **source** can be run. The bottom panel is the Xamine window to display the spectra.

tions and added some gates and spectra definitions. Those sections are marked by —EE.
In the *.tcl* script '#' is used to comment a statement.

```
# The spectcl_uk.tcl script #

# Esmat Elhami, Nov. 2007
# spectcl_uk.tcl file to build the matrix for 94Zr coincidence data.
# The experiment was performed at TUNL, March 2006.
# The original version of this script was written by Jhon Kelly, at TUNL.
# I have made some modiffications and added some gates and
# spectra definitions. Those were marked by EE.
#
# Procedure to fetch the set of non-blank input names
# from a module. This is done by doing a cget on the
# module. This returns a list of the form:
# {keyword value} {keyword value}
# We hunt down the entry where keyword == "parameters"
# In that case, value is a list of parameter names.
# We iterate through those for the non-blanks.
proc GetParameters mod {
    set config [$mod cget]
    set params ""
    foreach configitem $config {
set keyword [lindex $configitem 0]
set value [lindex $configitem 1]
if {$keyword == "parameters"} {
    foreach param $value {
if {$param != ""} {
    lappend params $param
}
}
}
}
return $params
}
# Procedure to define a bunch of parameters.
set paramno 0
```

```

proc DefineParameters {params res} {
    global paramno
    foreach param $params {
parameter $param $paramno $res
incr paramno
    }
}
#
# Define a raw spectrum for each parameter:
#
proc DefineSpectra {names res} {
    foreach name $names {
spectrum $name 1 $name $res
    }
}
# Source in the hardware definitions... this is where the parameter
# definitions come from as well as where the unpackers will be defined.
source /home/eelhami/spectcl_code/hardware94Zr.tcl
# Set up the unpacker order, define the parameters and raw parameter
# spectra.
# Note we also need to turn on packetization in the same way
# as for the readout so that the top level unpacker will
# understand there's a header:
unpack config packetize true id 0x8000

foreach m $ModuleOrder {
    unpack add $m
    set Params [GetParameters $m]
    if {[lindex $m 0] == "sc1"} {
DefineParameters $Params 26
    } else {
DefineParameters $Params 12
    }
    DefineSpectra $Params 12
}

#
# Set up 2-d spectra. If you have additional parameter pairs

```

```

# you want spectra set up for, adjust this list.
# Each entry is x,y,resolution
set pairs {}

foreach pair $pairs {
    set x [lindex $pair 0]
    set y [lindex $pair 1]
    set res [lindex $pair 2]

    spectrum $x-vs-$y 2 "$x $y" "$res $res"
}

# added for g2 histograms----- EE
set ghistos {}

foreach ghisto $ghistos {
    set x [lindex $ghisto 0]
    set y [lindex $ghisto 1]
    set res [lindex $ghisto 2]

    spectrum $x-vs-$y g2 "$x $y" "$res $res"
}

# added for sum histograms, not much use-----EE
set sums {}

foreach sum $sums {
    set x [lindex $sum 0]
    set y [lindex $sum 1]
    set res [lindex $sum 2]

    spectrum $x-vs-$y s "$x $y" "$res"
}

gate QID11 s {1Q1T {783 1483}}
gate QID12 s {1Q2T {780 1640}}
gate QID13 s {1Q3T {1140 1840}}
gate QID14 s {1Q4T {700 1400}}
gate QID21 s {2Q1T {1000 1800}}
gate QID22 s {2Q2T {762 1600}}
gate QID23 s {2Q3T {800 1430}}
gate QID24 s {2Q4T {740 1425}}

```

```

gate QID31 s {3Q1T {771 1629}}
gate QID32 s {3Q2T {627 1610}}
gate QID33 s {3Q3T {550 1500}}
gate QID34 s {3Q4T {550 1500}}
gate IDMON s {5MONT {400 690}}
#
apply QID11 1Q1
apply QID12 1Q2
apply QID13 1Q3
apply QID14 1Q4
apply QID21 2Q1
apply QID22 2Q2
apply QID23 2Q3
apply QID24 2Q4
apply QID31 3Q1
apply QID32 3Q2
apply QID33 3Q3
apply QID34 3Q4
#
apply IDMON 5MON_E
apply IDMON 5MON_PSD
#
spectrum MON_E_VS_PSD 2 {5MON_PSD 5MON_E} {8 8}
#
apply IDMON MON_E_VS_PSD
#
# create fit parameters
fit -create linear 1Q1_CALIB
fit -create linear 1Q2_CALIB
fit -create linear 1Q3_CALIB
fit -create linear 1Q4_CALIB
fit -create linear 2Q1_CALIB
fit -create linear 2Q2_CALIB
fit -create linear 2Q3_CALIB
fit -create linear 2Q4_CALIB
fit -create linear 3Q1_CALIB
fit -create linear 3Q2_CALIB
fit -create linear 3Q3_CALIB

```

```

fit -create linear 3Q4_CALIB
# describe the fit points
# may 8,2007, -----EE
fit -add 1Q1_CALIB {609.25 511} {1344.19 1274.53}
fit -add 1Q2_CALIB {608.29 511} {1307.37 1274.53}
fit -add 1Q3_CALIB {611.38 511} {1308.44 1274.53}
fit -add 1Q4_CALIB {610.72 511} {1327.90 1274.53}
fit -add 2Q1_CALIB {610.67 511} {1321.25 1274.53}
fit -add 2Q2_CALIB {608.07 511} {1315.98 1274.53}
fit -add 2Q3_CALIB {610.25 511} {1297.07 1274.53}
fit -add 2Q4_CALIB {611.30 511} {1343.91 1274.53}
fit -add 3Q1_CALIB {609.41 511} {1327.13 1274.53}
fit -add 3Q2_CALIB {610.81 511} {1273.16 1274.53}
fit -add 3Q3_CALIB {609.65 511} {1328.84 1274.53}
fit -add 3Q4_CALIB {608.97 511} {1342.47 1274.53}
## make the fit
fit -perform 1Q1_CALIB
fit -perform 1Q2_CALIB
fit -perform 1Q3_CALIB
fit -perform 1Q4_CALIB
fit -perform 2Q1_CALIB
fit -perform 2Q2_CALIB
fit -perform 2Q3_CALIB
fit -perform 2Q4_CALIB
fit -perform 3Q1_CALIB
fit -perform 3Q2_CALIB
fit -perform 3Q3_CALIB
fit -perform 3Q4_CALIB
# make the calibrated parameter with the fit applied
calibparam -create 1Q1_cal 101 1Q1 1Q1_CALIB keV
calibparam -create 1Q2_cal 102 1Q2 1Q2_CALIB keV
calibparam -create 1Q3_cal 103 1Q3 1Q3_CALIB keV
calibparam -create 1Q4_cal 104 1Q4 1Q4_CALIB keV
calibparam -create 2Q1_cal 105 2Q1 2Q1_CALIB keV
calibparam -create 2Q2_cal 106 2Q2 2Q2_CALIB keV
calibparam -create 2Q3_cal 107 2Q3 2Q3_CALIB keV
calibparam -create 2Q4_cal 108 2Q4 2Q4_CALIB keV
calibparam -create 3Q1_cal 109 3Q1 3Q1_CALIB keV

```



```

calibparam -create 3Q2_cal 110 3Q2 3Q2_CALIB keV
calibparam -create 3Q3_cal 111 3Q3 3Q3_CALIB keV
calibparam -create 3Q4_cal 112 3Q4 3Q4_CALIB keV
# CREATE HISTOGRAMS FOR calibrated parameters
spectrum 1Q1_cal 1 1Q1_cal 12
spectrum 1Q2_cal 1 1Q2_cal 12
spectrum 1Q3_cal 1 1Q3_cal 12
spectrum 1Q4_cal 1 1Q4_cal 12
spectrum 2Q1_cal 1 2Q1_cal 12
spectrum 2Q2_cal 1 2Q2_cal 12
spectrum 2Q3_cal 1 2Q3_cal 12
spectrum 2Q4_cal 1 2Q4_cal 12
spectrum 3Q1_cal 1 3Q1_cal 12
spectrum 3Q2_cal 1 3Q2_cal 12
spectrum 3Q3_cal 1 3Q3_cal 12
spectrum 3Q4_cal 1 3Q4_cal 12
#ADD gateS FOR QID@# WHERE @=DETECTOR NO, #=QUADRANT NO.
apply QID11 1Q1_cal
apply QID12 1Q2_cal
apply QID13 1Q3_cal
apply QID14 1Q4_cal
apply QID21 2Q1_cal
apply QID22 2Q2_cal
apply QID23 2Q3_cal
apply QID24 2Q4_cal
apply QID31 3Q1_cal
apply QID32 3Q2_cal
apply QID33 3Q3_cal
apply QID34 3Q4_cal
#####
# 3d spectra (E vs E vs Counts; 2d histograms) for coincidence
# of(e.g D1 with D2) with sheild vetoed gates to be applied
# upon. {resx resy}: resx=resy=12 means 2^12=4096(or 4k) channel.
# so {12 12} means a matrix with 4k x 4k x 4
# (long for parameters in g2 spectrum).
# In SpecTclInt.tcl the maximum DisplayMegabytes was 20 MB,
# so 16x4=84 MB, too large. In order to overcome this,
# I have put {{0.000000 8191.000000 2048} {0.000000 8191.000000 2048}},

```

```

# a matrix of x vs y, between 0 and 8191 in resolution of 2048.--EE
#####
# Spectrum definition should be in one line.
# spectrum ALL is uncommented, it will be created.
# other lines are examples.
#spectrum V1_2 g2 {1Q1_cal 2Q1_cal 1Q2_cal 2Q2_cal 1Q3_cal
#2Q3_cal 1Q4_cal 2Q4_cal}{11 11}
#spectrum V1_2 g2 {1Q1_cal 2Q1_cal 1Q2_cal 2Q2_cal 1Q3_cal
#2Q3_cal 1Q4_cal 2Q4_cal}
#{0.000000 4095.000000 2048} {0.000000 4095.000000 2048}} long
spectrum ALL g2 {1Q1_cal 1Q2_cal 1Q3_cal 1Q4_cal
2Q1_cal 2Q2_cal 2Q3_cal 2Q4_cal 3Q1_cal 3Q2_cal 3Q3_cal 3Q4_cal}
#{0.000000 8191.000000 2048}{0.000000 8191.000000 2048}} long
#####
# 1d histograms for each quadrant, #Q#_cal defined parameters in this file.
#These histograms were not used in Coincidence data analysis---EE
#####
spectrum 1Q1_COINSHV_11 1 1Q1_cal 12
spectrum 1Q2_COINSHV_11 1 1Q2_cal 12
spectrum 1Q3_COINSHV_11 1 1Q3_cal 12
spectrum 1Q4_COINSHV_11 1 1Q4_cal 12
#
spectrum 1Q1_COINSHV_12 1 1Q1_cal 12
spectrum 1Q2_COINSHV_12 1 1Q2_cal 12
spectrum 1Q3_COINSHV_12 1 1Q3_cal 12
spectrum 1Q4_COINSHV_12 1 1Q4_cal 12
#
spectrum 1Q1_COINSHV_13 1 1Q1_cal 12
spectrum 1Q2_COINSHV_13 1 1Q2_cal 12
spectrum 1Q3_COINSHV_13 1 1Q3_cal 12
spectrum 1Q4_COINSHV_13 1 1Q4_cal 12
#####
spectrum 2Q1_COINSHV_12 1 2Q1_cal 12
spectrum 2Q2_COINSHV_12 1 2Q2_cal 12
spectrum 2Q3_COINSHV_12 1 2Q3_cal 12
spectrum 2Q4_COINSHV_12 1 2Q4_cal 12
#
spectrum 2Q1_COINSHV_22 1 2Q1_cal 12

```

```

spectrum 2Q2_COINSHV_22 1 2Q2_cal 12
spectrum 2Q3_COINSHV_22 1 2Q3_cal 12
spectrum 2Q4_COINSHV_22 1 2Q4_cal 12
#
spectrum 2Q1_COINSHV_23 1 2Q1_cal 12
spectrum 2Q2_COINSHV_23 1 2Q2_cal 12
spectrum 2Q3_COINSHV_23 1 2Q3_cal 12
spectrum 2Q4_COINSHV_23 1 2Q4_cal 12
#####
spectrum 3Q1_COINSHV_13 1 3Q1_cal 12
spectrum 3Q2_COINSHV_13 1 3Q2_cal 12
spectrum 3Q3_COINSHV_13 1 3Q3_cal 12
spectrum 3Q4_COINSHV_13 1 3Q4_cal 12
#
spectrum 3Q1_COINSHV_23 1 3Q1_cal 12
spectrum 3Q2_COINSHV_23 1 3Q2_cal 12
spectrum 3Q3_COINSHV_23 1 3Q3_cal 12
spectrum 3Q4_COINSHV_23 1 3Q4_cal 12
#
spectrum 3Q1_COINSHV_33 1 3Q1_cal 12
spectrum 3Q2_COINSHV_33 1 3Q2_cal 12
spectrum 3Q3_COINSHV_33 1 3Q3_cal 12
spectrum 3Q4_COINSHV_33 1 3Q4_cal 12
#####
## a. gates for coincidence operations
gate COINID1_1 s {COIN11 {1 4000}}
gate COINID2_2 s {COIN22 {1 4000}}
gate COINID3_3 s {COIN33 {1 4000}}
gate COINID1_2 s {COIN12 {1 4000}}
gate COINID1_3 s {COIN13 {1 4000}}
gate COINID2_3 s {COIN23 {1 4000}}
#
##
gate NOCOIN1_1 - {COINID1_1}
gate NOCOIN2_2 - {COINID2_2}
gate NOCOIN3_3 - {COINID3_3}
gate NOCOIN1_2 - {COINID1_2}
gate NOCOIN1_3 - {COINID1_3}

```

```

gate NOCOIN2_3 - {COINID2_3}
###
# b. definition of gates for shield in coincidence with each quadrant
gate SHIELD11_COIN s {1SHIELDT {1900 2700}}
gate SHIELD12_COIN s {1SHIELDT {1900 2700}}
gate SHIELD13_COIN s {1SHIELDT {1900 2700}}
gate SHIELD14_COIN s {1SHIELDT {1900 2700}}
gate SHIELD21_COIN s {2SHIELDT {1950 2730}}
gate SHIELD22_COIN s {2SHIELDT {1950 2730}}
gate SHIELD23_COIN s {2SHIELDT {1950 2730}}
gate SHIELD24_COIN s {2SHIELDT {1950 2730}}
gate SHIELD31_COIN s {3SHIELDT {1800 2500}}
gate SHIELD32_COIN s {3SHIELDT {1800 2500}}
gate SHIELD33_COIN s {3SHIELDT {1800 2500}}
gate SHIELD34_COIN s {3SHIELDT {1800 2500}}
#
#c. noveto gate, when there is no coincidences btwn a quadrant and its shield
# quadrant and its shield
gate SHIELD11_NOVETO - {SHIELD11_COIN}
gate SHIELD12_NOVETO - {SHIELD12_COIN}
gate SHIELD13_NOVETO - {SHIELD13_COIN}
gate SHIELD14_NOVETO - {SHIELD14_COIN}
gate SHIELD21_NOVETO - {SHIELD21_COIN}
gate SHIELD22_NOVETO - {SHIELD22_COIN}
gate SHIELD23_NOVETO - {SHIELD23_COIN}
gate SHIELD24_NOVETO - {SHIELD24_COIN}
gate SHIELD31_NOVETO - {SHIELD31_COIN}
gate SHIELD32_NOVETO - {SHIELD32_COIN}
gate SHIELD33_NOVETO - {SHIELD33_COIN}
gate SHIELD34_NOVETO - {SHIELD34_COIN}
#
# d. gate of coincidence btwn a quadrant in a clover and
#any other quadrant in another clover
#for clover1
##
gate COINID11_1 * {QID11 COINID1_1}
gate COINID11_2 * {QID11 COINID1_2}
gate COINID11_3 * {QID11 COINID1_3}

```

```

#
gate COINID12_1 * {QID12 COINID1_1}
gate COINID12_2 * {QID12 COINID1_2}
gate COINID12_3 * {QID12 COINID1_3}
#
gate COINID13_1 * {QID13 COINID1_1}
gate COINID13_2 * {QID13 COINID1_2}
gate COINID13_3 * {QID13 COINID1_3}
#
gate COINID14_1 * {QID14 COINID1_1}
gate COINID14_2 * {QID14 COINID1_2}
gate COINID14_3 * {QID14 COINID1_3}
#####
#for clover2
##
gate COINID21_1 * {QID21 COINID1_1}
gate COINID21_2 * {QID21 COINID1_2}
gate COINID21_3 * {QID21 COINID1_3}
#
gate COINID22_1 * {QID22 COINID1_1}
gate COINID22_2 * {QID22 COINID1_2}
gate COINID22_3 * {QID22 COINID1_3}
#
gate COINID23_1 * {QID23 COINID1_1}
gate COINID23_2 * {QID23 COINID1_2}
gate COINID23_3 * {QID23 COINID1_3}
#
gate COINID24_1 * {QID24 COINID1_1}
gate COINID24_2 * {QID24 COINID1_2}
gate COINID24_3 * {QID24 COINID1_3}
#####
#for clover3
##
gate COINID31_1 * {QID31 COINID1_1}
gate COINID31_2 * {QID31 COINID1_2}
gate COINID31_3 * {QID31 COINID1_3}
#
gate COINID32_1 * {QID32 COINID1_1}

```

```

gate COINID32_2 * {QID32 COINID1_2}
gate COINID32_3 * {QID32 COINID1_3}
#
gate COINID33_1 * {QID33 COINID1_1}
gate COINID33_2 * {QID33 COINID1_2}
gate COINID33_3 * {QID33 COINID1_3}
#
gate COINID34_1 * {QID34 COINID1_1}
gate COINID34_2 * {QID34 COINID1_2}
gate COINID34_3 * {QID34 COINID1_3}
#####
# e. coincidence with veto on sheilds-----EE
#for clover1
##
gate VCOINID11_1 * {COINID11_1 SHIELD11_NOVETO}
gate VCOINID11_2 * {COINID11_2 SHIELD11_NOVETO}
gate VCOINID11_3 * {COINID11_3 SHIELD11_NOVETO}
#
gate VCOINID12_1 * {COINID12_1 SHIELD12_NOVETO}
gate VCOINID12_2 * {COINID12_2 SHIELD12_NOVETO}
gate VCOINID12_3 * {COINID12_3 SHIELD12_NOVETO}
#
gate VCOINID13_1 * {COINID13_1 SHIELD13_NOVETO}
gate VCOINID13_2 * {COINID13_2 SHIELD13_NOVETO}
gate VCOINID13_3 * {COINID13_3 SHIELD13_NOVETO}
#
gate VCOINID14_1 * {COINID14_1 SHIELD13_NOVETO}
gate VCOINID14_2 * {COINID14_2 SHIELD13_NOVETO}
gate VCOINID14_3 * {COINID14_3 SHIELD13_NOVETO}
#####
#for clover2
##
gate VCOINID21_1 * {COINID21_1 SHIELD21_NOVETO}
gate VCOINID21_2 * {COINID21_2 SHIELD21_NOVETO}
gate VCOINID21_3 * {COINID21_3 SHIELD21_NOVETO}
#
gate VCOINID22_1 * {COINID22_1 SHIELD22_NOVETO}
gate VCOINID22_2 * {COINID22_2 SHIELD22_NOVETO}

```

```

gate VCOINID22_3 * {COINID22_3 SHIELD22_NOVETO}
#
gate VCOINID23_1 * {COINID23_1 SHIELD23_NOVETO}
gate VCOINID23_2 * {COINID23_2 SHIELD23_NOVETO}
gate VCOINID23_3 * {COINID23_3 SHIELD23_NOVETO}
#
gate VCOINID24_1 * {COINID24_1 SHIELD24_NOVETO}
gate VCOINID24_2 * {COINID24_2 SHIELD24_NOVETO}
gate VCOINID24_3 * {COINID24_3 SHIELD24_NOVETO}
#####
#for clover3
##
gate VCOINID31_1 * {COINID31_1 SHIELD31_NOVETO}
gate VCOINID31_2 * {COINID31_2 SHIELD31_NOVETO}
gate VCOINID31_3 * {COINID31_3 SHIELD31_NOVETO}
#
gate VCOINID32_1 * {COINID32_1 SHIELD32_NOVETO}
gate VCOINID32_2 * {COINID32_2 SHIELD32_NOVETO}
gate VCOINID32_3 * {COINID32_3 SHIELD32_NOVETO}
#
gate VCOINID33_1 * {COINID33_1 SHIELD33_NOVETO}
gate VCOINID33_2 * {COINID33_2 SHIELD33_NOVETO}
gate VCOINID33_3 * {COINID33_3 SHIELD33_NOVETO}
#
gate VCOINID34_1 * {COINID34_1 SHIELD34_NOVETO}
gate VCOINID34_2 * {COINID34_2 SHIELD34_NOVETO}
gate VCOINID34_3 * {COINID34_3 SHIELD34_NOVETO}
#####
#f. final coincidence to combine all quadrants gates to
# get each clover's--EE
##
gate VDET1_1 + {VCOINID11_1 VCOINID12_1 VCOINID13_1 VCOINID14_1}
gate VDET2_1 + {VCOINID21_1 VCOINID22_1 VCOINID23_1 VCOINID24_1}
gate VDET3_1 + {VCOINID31_1 VCOINID32_1 VCOINID33_1 VCOINID34_1}
gate VDET1_2 + {VCOINID11_2 VCOINID12_2 VCOINID13_2 VCOINID14_2}
gate VDET2_2 + {VCOINID21_2 VCOINID22_2 VCOINID23_2 VCOINID24_2}
gate VDET3_2 + {VCOINID31_2 VCOINID32_2 VCOINID33_2 VCOINID34_2}
gate VDET1_3 + {VCOINID11_3 VCOINID12_3 VCOINID13_3 VCOINID14_3}

```

```

gate VDET2_3 + {VCOINID21_3 VCOINID22_3 VCOINID23_3 VCOINID24_3}
gate VDET3_3 + {VCOINID31_3 VCOINID32_3 VCOINID33_3 VCOINID34_3}
#####
# no coincidence---test-----EE
gate V1_1 * {VDET1_1 NOCOIN1_1}
gate V2_2 * {VDET2_2 NOCOIN2_2}
gate V1_2 * {VDET1_2 NOCOIN1_1}
gate V2_1 * {VDET2_1 NOCOIN2_2}
gate F1_2 + {V1_2 V2_1}
#apply F1_2 V1_2
#####
#g. final coincidences to combine clovers(e.g.1_2 and 2_1)-----EE
##
gate VCF1_2 + {VDET1_2 VDET2_1}
gate VCF1_3 + {VDET1_3 VDET3_1}
gate VCF2_3 + {VDET2_3 VDET3_2}
gate VALL + {VCF1_2 VCF1_3 VCF2_3}
#####
# h. The spectra should be called one at a time. ----EE
#####
apply VCF1_2 V1_2
#apply VCF1_3 V1_3
#apply VCF2_3 V2_3
#apply VALL ALL
#####
#application of single gates on 1d histograms, this could be left out--EE
#####
#clover1
##
apply VCOINID11_1 1Q1_COINSHV_11
apply VCOINID12_1 1Q2_COINSHV_11
apply VCOINID13_1 1Q3_COINSHV_11
apply VCOINID14_1 1Q4_COINSHV_11
#
apply VCOINID11_2 1Q1_COINSHV_12
apply VCOINID12_2 1Q2_COINSHV_12
apply VCOINID13_2 1Q3_COINSHV_12
apply VCOINID14_2 1Q4_COINSHV_12

```



```

#
apply VCOINID11_3 1Q1_COINSHV_13
apply VCOINID12_3 1Q2_COINSHV_13
apply VCOINID13_3 1Q3_COINSHV_13
apply VCOINID14_3 1Q4_COINSHV_13
#####
#clover2
##
apply VCOINID21_1 2Q1_COINSHV_12
apply VCOINID22_1 2Q2_COINSHV_12
apply VCOINID23_1 2Q3_COINSHV_12
apply VCOINID24_1 2Q4_COINSHV_12
#
apply VCOINID21_2 2Q1_COINSHV_22
apply VCOINID22_2 2Q2_COINSHV_22
apply VCOINID23_2 2Q3_COINSHV_22
apply VCOINID24_2 2Q4_COINSHV_22
#
apply VCOINID21_3 2Q1_COINSHV_23
apply VCOINID22_3 2Q2_COINSHV_23
apply VCOINID23_3 2Q3_COINSHV_23
apply VCOINID24_3 2Q4_COINSHV_23
#####
#clover3
##
apply VCOINID31_1 3Q1_COINSHV_13
apply VCOINID32_1 3Q2_COINSHV_13
apply VCOINID33_1 3Q3_COINSHV_13
apply VCOINID34_1 3Q4_COINSHV_13
#
apply VCOINID31_2 3Q1_COINSHV_23
apply VCOINID32_2 3Q2_COINSHV_23
apply VCOINID33_2 3Q3_COINSHV_23
apply VCOINID34_2 3Q4_COINSHV_23
#
apply VCOINID31_3 3Q1_COINSHV_33
apply VCOINID32_3 3Q2_COINSHV_33
apply VCOINID33_3 3Q3_COINSHV_33

```

```

apply VCOINID34_3 3Q4_COINSHV_33
#####
#####
#
sbind -all

spectrum -delete t1p16
spectrum -delete t1p18
spectrum -delete t1p20
spectrum -delete t1p27
spectrum -delete t1p28
spectrum -delete t1p29
spectrum -delete t1p30
spectrum -delete t1p31
spectrum -delete t1p32
spectrum -delete a1p18
spectrum -delete a1p19
spectrum -delete a1p20
spectrum -delete a1p21
spectrum -delete a1p22
spectrum -delete a1p23
spectrum -delete a1p24
spectrum -delete a1p25
spectrum -delete a1p26
spectrum -delete a1p27
spectrum -delete a1p28
spectrum -delete a1p29
spectrum -delete a1p30
spectrum -delete a1p31
spectrum -delete a1p32

# The end of the spectcl.uk.tcl script.##

```

F.5 Hardware Setup .tcl Script, hardware94Zr.tcl

The *hardware94Zr.tcl* is a *.tcl* script used for data acquisition for the ^{94}Zr $\gamma\gamma$ coincidence experiment at TUNL, using SpecTcl. The script defines the hardware setup parameters, time and energy. This *.tcl* script was sourced in the *spectcl.uk.tcl* script to readout the

recorded parameters.

```
# hardware94Zr.tcl script #

# Setup the readout software.

# 32 channel modules will have all channels turned on
# for now:
#
# Common thresholds for now:

set thresholds 15
for {set i 0} {$i < 32} {incr i} {
    lappend thrlist $thresholds
}

# The first 785 is configured for base addressing at e5000000
# thresholds set as per thrlist single vent mode all channels
# enabled with channel names of the form a1pnn
#
for {set i 0} {$i < 18} {incr i} {
    lappend enables 1; # This becomes 16 1's.
}

for {set i 18} {$i < 32} {incr i} {
    lappend enables 0; # This becomes 16 0's.
}

module adc1 caenv785 slot 5 geo false base [expr 0xe6000000]
adc1 config threshold $thrlist multievent false enable $enables
catch "adc1 config waitloops 10"
adc1 config parameters {1Q1 1Q2 1Q3 1Q4 2Q1 2Q2 2Q3 2Q4 \
                        3Q1 3Q2 3Q3 3Q4 \
5MON_PSD 5MON_E SHIELD2 SHIELD3 \
SHIELD1 a1p18 a1p19 a1p20 a1p21 a1p22 a1p23 a1p24\
a1p25 a1p26 a1p27 a1p28 a1p29 a1p30 a1p31 a1p32}
# the second adc, the same thing but base is 0xe6000000
# and the parameter are cleverly enough named a2pnn
```

```

#
# The TDC will be named similarly... for now common start
# with parameters t1pnn
#

for {set i 0} {$i < 17} {incr i} {
  lappend ttables 1; # This becomes 4 1's.
}

for {set i 17} {$i < 18} {incr i} {
  lappend ttables 0; # This becomes 16 0's.
}

for {set i 18} {$i < 26} {incr i} {
  lappend ttables 1; # This becomes 16 0's.
}

for {set i 26} {$i < 32} {incr i} {
  lappend ttables 0; # This becomes 16 0's.
}

module tdc caenv775 slot 9 geo false base [expr 0xe3000000]
tdc config threshold $thrlst multievent false enable $ttables
catch "tdc config waitloops 10"
catch "tdc config commonstart true keepoverflow false range 630"
tdc config parameters {1Q1T 1Q2T 1Q3T 1Q4T \
  2Q1T 2Q2T 2Q3T 2Q4T \
  3Q1T 3Q2T 3Q3T 3Q4T \
  1SHIELDT 2SHIELDT 3SHIELDT t1p16 \
RFT t1p18 5MONT t1p20 COIN11 COIN22 COIN33 COIN12 \
COIN13 COIN23 t1p27 t1p28 t1p29 t1p30 t1p31 t1p32}

scaler counters caenv830 base [expr 0xee000000] geo
false header false trigger 1
counters config slot 11 packetize false autoreset false manualclear true
counters config fpclearmeb false id 0x101 vmetrigger true wide true
counters config header false

counters config parameters {1_Q1 1_Q2 1_Q3 1_Q4 \
2_Q1 2_Q2 2_Q3 2_Q4 \
  3_Q1 3_Q2 3_Q3 3_Q4 \

```

```
5MON 1SHIELD 2SHIELD 3SHIELD\  
ORAW OMG OMGLIVE 10HZ \  
  
1DRAW 2DRAW 3DRAW OBCI \  
  
O11MG O22MG O33MG 5MON_S \  
OC12MG OC13MG OC23MG 5MGLIVE}  
  
#set ModuleOrder {adc1 adc2 tdc}           ;# Readout/unpack order.  
set ModuleOrder {tdc adc1}                 ;# Readout/unpack order.  
set ScalerOrder {counters}; # scaler readout order.  
  
# The end of the script #
```

Appendix G: UK COINCIDENCE DATA ANALYSIS

The following steps should be taken for the UK coincidence data analysis:

1. Create the energy and time raw spectra for each detector, from each run: e1-e4 and t1-t4 by the **cmt5** code, in *projection* mode, Section G.1.

These spectra are used for energy calibrations of the energy signals and defining the coincident time windows in each detector, respectively. Details can be found in [50].

2. Build a matrix using **cmt5**, Section G.2.
3. Create X, Y, and background (bg) projections of the matrix by **slice**, Section G.3.
4. Create a *levelschem.gls* file in **xmgls**.
5. Create the compressed form of the built matrix in **xmesc**, Section G.5.

6. Use **xmesc** to analyze the coincidence spectrum by gating on gamma-ray energies.

Windows and slices can be also created in **gf3**, another way to analyze the coincidence data, not discussed here.

G.1 Creating Time and Energy Spectra

1) To create projections or simple spectra of each detector's parameters, i.e., energy and time, **cmt5** is run with an input file of *fname_cmt.inp*. A detailed description of the input file entries and the output spectra formats can be found in [50]. Part of the input file for ^{106}Pd data was:

```
number 4
emr e1 e2 e3 e4 t1 t2 t3 t4
mode project
multi 1
TCshift 4096
gain 1 1
```

```
zero_projections
treat 106pd.1.emr.gz
proj_file002_write 106pd01
```

```
zero_projections
treat 106pd.2.emr.gz
proj_file002_write 106pd02
```

...

The last three lines were repeated for each raw data file. The raw data can be either in

rname.emr or *rnmae.emr.gz*. If the latter is used, the code **cmt5** unzips the files.

2) Run **cmt5** code by: **cmt5 < fname_cmt.inp .**

NOTE: Some error-like lines would run across the screen. Do not abort the run. It takes a while. The output files are *rname_ti.spe* and *rname_ei.spe* spectra, corresponding to each run number, readable in **CNE**. The detail of using these spectra for building a matrix is discussed in the next section.

G.2 Building a Matrix

The following files are needed to build a matrix:

- 1) The *fname.cmt* files for any number of runs with which you would like to build the matrix,
- 2) The *rname.emr* raw data files, which are embedded in *rname.cmt*,
- 3) A *fname_mat.inp* file for input to **cmt5** to be run in *matrix* mode [50].

Part of the *fname_mat.inp* file for ^{106}Pd data is given below; for description of each line see Ref. [50].

```
number 4
emr e1 e2 e3 e4 t1 t2 t3 t4
mode symmetric
multi 2
gain 1.5 1.5
create_matrix fname.matd
open fname.matd
run 106pd01.cmt
run 106pd02.cmt
run 106pd03.cmt
...
```

```
close
compact fname.matd FALSE
```

For this input file, the *rname.cmt* files are written using the output spectra, described in Section G.1. The time limits for more stringent coincidence requirements, in 'limit T1 ...' were determined from each Ti spectrum, as explained in Section 3.8.1. The limits were only determined for each detector. The coincidence time between any two detectors is not determined here. It has been done electronically in the experiment setup. Energy

calibrations of the E_i parameters provide a calibrated matrix, which is very crucial. The energy calibration coefficients were obtained from the calibrations of each E_i spectrum using CNE; details can be found in Ref. [50].

Again, the raw data can be either in *rname.emr* or *rnmae.emr.gz*, if the latter is used the code **cmt5** unzips the files.

For example, the *106pd01.cmt* file is given below. For descriptions of the entries, see Ref. [50]

```
reset_limits
limit T1 748-821
limit T2 775-848
limit T3 754-827
limit T4 630-703
show_limits
calibrate E1 0.94042 0.17824 7.41890e-09
calibrate E2 1.52569 0.17804 5.90484e-09
calibrate E3 1.79947 0.17913 9.94645e-09
calibrate E4 1.83830 0.17955 1.70079e-08
show_calibrations
treat 106pd1.emr.gz
```

The command **cmt5** < **fname_mat.inp** > **fname_mat.log** creates the outputs of *fname.mtd* matrix in RadWare format and the *fname_mat.log* file. The *fname.mtd* file should be renamed to *fname.mat* for further analysis in **xmesc**; this code only takes *fname.mat* as an input file.

G.3 Creating X and Y Projections Using the Code slice

The computer programs used in this section and the following sections are part of RadWare software package developed by D. C. Radford in the Physics Division of the Oak Ridge National Laboratory. More information and details of programs used in this section can be found in Ref. [61].

The code **slice** was used to create the X or Y projection spectra from the matrix, *fname.mat*, which was built using **cmt5**, Section G.2. The output files are *fnameX.spe* and *fnameY.spe*, which can be displayed in Tv or CNE.

Note: In the following the \$ sign refers to the prompt command line. The dialog of each command is typed in the Typewriter and the user inputs in the *Italic* fonts. The phrases in (*Slanted*) are the explanation to what should be done, or general comments.

```
$ slice
```

```
SLICE - a program to slice and/or project 4k by 4k gamma-gamma matrices.
```


This program now accepts matrices in both .mat (2 Bytes/ch)
and .spn or .m4b (4 Bytes/ch) formats.
Specify .ext = .spn or .m4b for 4 Bytes/ch.
The default extension for all spectrum files is .spe
D. C. Radford May 2000
Matrix file name = ? (return for mat1.mat,E to end,default .ext = .mat)*fname*
Take slices ? (Y/N) *n*
Take projections? (Y/N) *y*
Working...
X-Projection spectrum file name = ? *fnameX.spe*
Y-Projection spectrum file name = ? *fnameY.spe*
Matrix file name = ? (return for fname.mat, E to end, default .ext = .mat) *e*

G.4 Creating Background Spectra

A background spectrum for either *fnameX.spe* or *fnameY.spe* spectra, can be created in the **gf3** environment, using the **bg** command.

For example, to create a background spectrum from an *fnameX.spe*, the following commands are executed.

```
$ gf3 fnameX.spe ,
(use Return key until the prompt sign, ? appears).
? Sp. fnameX 4096 chs read.
? bg
This auto-background procedure uses a multiple of the
'starting width' at each channel as a length scale for finding the background.
If the results are unsatisfactory, check the width parameters
with the 'SW' command. You can also vary the length scale factor to
fine-tune the background to your taste.
Background length factor = ? (Return for 1.0)
Lower limit for background = ? (A to abort)... (click on a channel at the be-
ginning of the spectrum)
Upper limit for background = ? (A to abort)... (click on a channel at the end
of the spectrum)
...Change length scale factor? (Y/N) n
? ws
Name of output file = ? fnameXbg.spe
Spectrum name = ? (rtn for same as file name)
?
```

? *stp*

Are you sure you want to exit? (Y/N) *y*

The created background spectrum, which is a simple curve line, can be displayed using the **gf3 fnameXbg.spe** command.

G.5 Creating a Matrix in a Compressed Format for Analysis in **xmesc**

Usually the coincidence data are analyzed using **xmesc**, which uses a matrix in a compressed format. The **xmesc** code was used to create the compressed matrix, *fname.esc* from the original matrix, i.e., *fname.mat*. A preliminary level scheme, *levname.gls*, can be either created in **xmgls**, or in **xmesc** while creating the *fname.esc* matrix. The code gives either option. To create a matrix in a compressed format, **xmesc** is used as follow:

```
$ xmesc
```

```
Trying to create pixmap of size 600 by 500
```

```
ESCL8R.GLS Version 2.0 D. C. Radford Oct 1999
```

```
Welcome....
```

```
GLS level scheme file = ? (default .ext = .glg)(rtn to create new file) lev-  
name
```

```
Compressed matrix data file = ? (default .ext = .esc)  
(rtn to create new file)
```

```
Compressed matrix data file preparation routine...
```

```
...
```

```
Matrix file = ? (default .ext = .mat) fname
```

```
Name for new escl8r data file = ? (rtn for fname.esc)
```

```
(specify .ext = .e4k to keep full 4kx4k chs)
```

```
(default .ext = .esc) (the output will be fname.esc)
```

```
The matrix will be reduced to 2048 x 2048 channels.
```

```
You have a choice of compressing by a factor of two or just taking the first  
2048 channels.
```

```
...Compress matrix by factor of two? (Y/N) y
```

```
Compressing matrix to new file fname.esc_log
```

```
Energy calibration file for original matrix = ?
```

```
(default .ext = .aca, .cal) eu152
```

```
eu152.sto eu152.sou
```

```
Efficiency parameter file = ? (default .ext = .aef, .eff) eff
```

```
...
```

```

Total projection spectrum file name = ? fnameX
Total background spectrum file name = ? fnameXbg
ESCL8R now adds systematic errors for the background subtraction.
Default value is 5.0%.
Percentage error on background = ? (rtn for default)
2D Scaling factor = 1.171e+01 (could be some other number)
Mean square error on calculation = 341.62
Mean square error on calculation = 341.62

```

The last two numbers give an indication of whether or not *fname.esc* has been created. The calibration files, *eu152.aca* for energy, and *eff.aef* for efficiency, were obtained using the **en cal** and **effit** codes, respectively [61].

G.6 Creating Gated Spectra in **xmesc**

By executing **xmesc** in the prompt command line, two other windows are opened: the graphical window, **XmEscl8r**, and **Spectrum Window**. A *gate* can be selected by choosing the numbers of gates from the *Spectrum* in the **XmEscl8r** menu. The energy is entered in the command line of the **XmEscl8r** window and the gated spectrum is displayed in the **Spectrum Window**. To create gated spectra, **xmesc** is used as follow:

```

$ xmesc
Trying to create pixmap of size 600 by 500
ESCL8R.GLS Version 2.0 D. C. Radford Oct 1999
Welcome....
GLS level scheme file = ? (default .ext = .gls)
(rtn to create new file) levname
Compressed matrix data file = ? (default .ext = .esc)
(rtn to create new file) fname
Mean square error on calculation = 341.62
Mean square error on calculation = 341.62

```

A gated spectrum from ^{106}Pd coincidence data, created by **xmesc**, is shown in Figure 3.15.

Detailed analysis on the γ - γ matrix, to create gated spectra, can be done by exploring the features of the **XmEscl8r** menu. It is a very powerful tool and many useful information can be obtained; see Ref. [61].

BIBLIOGRAPHY

- [1] M. G. Mayer and J. Hans D. Jensen, *Elementary Theory of Nuclear Shell Structure*, John Wiley & Sons, New York (1995).
- [2] W. D. Ehmann and D. E. Vance, *Radiochemistry and Nuclear Methods of Analysis*, John Wiley & Sons, New York (1991).
- [3] <http://www.vanderbilt.edu/AnS/physics/volker/research>.
- [4] K. Heyde, *The Nuclear Shell Model*, 2nd Edition, Springer-Verlag (1994).
- [5] K. S. Krane, *Introductory Nuclear Physics*, John Wiley & Sons, New York (1987).
- [6] R. F. Casten, *Nuclear Structure from a Simple Perspective*, 2nd Edition, Oxford University Press, New York (2000).
- [7] A. Bohr and B. R. Mottelson, *Nuclear Structure*, vol I, W.A. Benjamin Inc., Reading (1969).
- [8] <http://www.nndc.bnl.gov> *National Nuclear Data Center (NNDC)*.
- [9] A. Arima and F. Iachello, *Ann. Rev. Nucl. Part. Sci.* **31**:pp. 75-105 (1981).
- [10] F. Iachello and A. Arima, *The Interacting Boson Model*, Cambridge University Press, Cambridge (1987).
- [11] R. F. Casten, P. O. Lipas, T. Otsuka, K. Heyde, and J. P. Draayer, *Algebraic Approach to Nuclear Structure - Interacting Boson and Fermion Models*, Hardwood Academic Publishers, Switzerland (1993).
- [12] W. D. Kulp, J. L. Wood, P. E. Garrett, J. M. Allmond, D. Cline, A. B. Hayes, H. Hua, K. S. Krane, R.-M. Larimer, J. Loats, E. B. Norman, P. Schmelzenbach, C. J. Staples, R. Teng, and C. Y. Wu, *Phys. Rev. C* **71**, 041303(R) (2005).
- [13] F. Iachello, *Phys. Rev. Lett.* **53**, 1427 (1984).
- [14] D. Bohle, A. Richter, W. Steffen, A. E. L. Dieperink, N. Lo Iudice, F. Palumbo and O. Scholten, *Phys. Lett.* **B137**, 27 (1984).
- [15] N. Pietralla, P. von brentano, and A. F. Lisetskiy, *Prog. Part. Nucl. Phys.* **60**, 225 (2008).
- [16] A. Faessler, *Nucl. Phys.* **A85**, 653 (1986).
- [17] G. Siems, U. Neuneyer, I. Wiedenhöver, S. Albers, M. Eschenauer, R. Wirowski, A. Gelberg, P. von Brentano and T. Otsuka, *Phys. Lett.* **B320**, 1 (1994).
- [18] F. Schussler, J. A. Pinston, E. Monnard, A. Moussa, G. Jung, E. Koglin, B. Pfeiffer, R. V. F. Janssens, and V. van Klinken, *Nucl. Phys.* **A339**, 415 (1980).
- [19] P. E. Garrett, W. Younes, J. A. Becker, and L. A. Bernstein, E. M. Baum, D. P. DiPrete, R. A. Gatenby, E. L. Johnson, C. A. McGrath, S. W. Yates, M. Devlin, N. Fotiades, and R. O. Nelson, and B. A. Brown, *Phys. Rev. C* **68**, 024312 (2003).

- [20] G. Molnár, T. Belgya, B. Fazekas, Á. Veres, S. W. Yates, E. L. Kleppinger, R. A. Gatenby, R. Julin, J. Kumpulainen, A. Passoja, and E. Verho, Nucl. Phys. **A500**, 43 (1989).
- [21] H. Mach, M. Moszynski, R. L. Gill, F. K. Wohn, J. A. Winger, John C. Hill, G. Molnár and K. Sistemich, Phys. Lett. **B230**, 21 (1989).
- [22] G. Lhersonnaeu, B. Pfeiffer, K.-L. Kratz, T. Enqvist, P. P. Jauho, A. Jokinen, J. Kantele, M. Leino, J. M. Parmonen, H. Penttilä, and J. Äystö, Phys. Rev. **C 49**, 1379 (1994).
- [23] N. Pietralla, C. Fransen, D. Belic, P. von Brentano, C. Frißner, U. Kneissl, A. Linnemann, A. Nord, H. H. Pitz, T. Otsuka, I. Schneider, V. Werner, and I. Wiedenhöver, Phys. Rev. Lett. **83**, 1303 (1999).
- [24] C. Fransen, N. Pietralla, Z. Ammar, D. Bandyopadhyay, N. Boukharouba, P. von Brentano, A. Dewald, J. Gableske, A. Gade, J. Jolie, U. Kneissl, S. R. Leshner, A. F. Lisetskiy, M. T. McEllistrem, M. Merrick, H. H. Pitz, N. Warr, V. Werner, and S. W. Yates, Phys. Rev. C **67**, 024307 (2003).
- [25] C. Fransen, V. Werner, D. Bandyopadhyay, N. Boukharouba, S. R. Leshner, M. T. McEllistrem, J. Jolie, N. Pietralla, P. von Brentano, and S. W. Yates, Phys. Rev. C **71**, 054304 (2005).
- [26] N. Pietralla, C. J. Barton, R. Krcken, C. W. Beausang, M. A. Caprio, R. F. Casten, J. R. Cooper, A. A. Hecht, H. Newman, J. R. Novak, and N. V. Zamfir, Phys. Rev. C **64**, 031301 (2001).
- [27] H. Klein, A. F. Lisetskiy, N. Pietralla, C. Fransen, A. Gade, and P. von Brentano, Phys. Rev. C **65**, 044315 (2002).
- [28] J. N. Orce, J. D. Holt, A. Linnemann, C. J. McKay, S. R. Leshner, C. Fransen, J. W. Holt, A. Kumar, N. Warr, V. Werner, J. Jolie, T. T. S. Kuo, M. T. McEllistrem, N. Pietralla, and S. W. Yates, Phys. Rev. Lett. **97**, 062504 (2006).
- [29] A. F. Lisetskiy, N. Pietralla, C. Fransen, R. V. Jolos, and P. von Brentano, Nucl. Phys. **A677**, 100 (2000).
- [30] N. Lo Iudice and Ch. Stoyanov, Phys. Rev. **C65**, 064304 (2002).
- [31] V. Werner, D. Belic, P. von Brentano, C. Fransen, A. Gade, H. von Garrel, J. Jolie, U. Kneissl, C. Kohstall, A. Linnemann, A. F. Lisetskiy, N. Pietralla, H. H. Pitz, M. Scheck, K. H. Speidel, F. Stedile, and S. W. Yates, Phys. Lett. **B550**, 140 (2002).
- [32] N. Lo Iudice and C. Stoyanov, Phys. Rev. C **73**, 037305 (2006).
- [33] S. L. Leshner, C. J. McKay, M. Mynk, D. Bandyopadhyay, N. Boukharouba, C. Fransen, J. N. Orce, M. T. McEllistrem, and S. W. Yates, Phys. Rev. C **75**, 034318 (2007).
- [34] D. Abriola, A. A. Sonzogni, Nuclear Data Sheets **107**, 2423-2578 (2006), (p. 2450), (*NDS data for ^{94}Zr*).
- [35] G. P. Glasgow, F. D. McDaniel, J. L. Weil, J. D. Brandenberger, and M. T. McEllistrem, Phys. Rev. C **18**, 2520 (1978).

- [36] E. Elhami, J. N. Orce, S. Mukhopadhyay, S. N. Choudry, M. Scheck, M. T. McEllistrem, and S. W. Yates, Phys. Rev. C **75**, 011301(R) (2007).
- [37] E. Elhami, et *al.*, in preparation.
- [38] P. E. Garrett, N. Warr and S. W. Yates, J. Res. Natl. Inst. Stand. Technol. **105**,141 (2000).
- [39] Minfang Yeh, P. E. Garrett, C. A. McGrath, S. W. Yates, and T. Belgya, Phys. Rev. Lett. **76**, 1208 (1996).
- [40] R. M. Diamond, E. Matthias, J. O. Newton, and F. S. Stephens, Phys. Rev. Lett. **16**, 1205 (1966).
- [41] C. A. McGrath, P. E. Garrett, M. F. Villani, and S. W. Yates, Nucl. Instrum. Methods **A421**, 458 (1999).
- [42] M. T. McEllistrem, *Nuclear Research with Low Energy Accelerators*, Academic Press, New York (1967).
- [43] G. F. Knoll, *Radiation Detection and Measurement*, 2nd Edition, John Wiley & Sons, 1989 .
- [44] N. Warr, UK Experiments Manual, *Unpublished* (2000). (*For UK users: this manual can be found in warr directory in the cluster, under the 'doc' subdirectory*).
- [45] S. R. Leshner, Ph.D. Dissertation, University of Kentucky (2004).
- [46] A. Hutcheson, C. T. Angell, J. A. Becker, M. Boswell, A. S. Crowell, D. Dashdorj, B. Fallin, N. Fotiades, C. R. Howell, H. J. Karwowski, J. H. Kelley, M. Kiser, R. A. Marci, R. O. Nelson, R. S. Pedroni, A. P. Tonchev, W. Tornow, D. J. Vieira, G. J. Weisel, and J. B. Wilhelmy, Nucl. Instrum. and Methods in Phys. Res. **B261**, 369 (2007).
- [47] <http://docs.nsl.msu.edu/daq/spectcl> (*SpecTcl*).
- [48] <http://www.tcl.tk> (*Tcl language*).
- [49] Y. A. Akovali, Nuclear Data Sheets **77**, 433 (1996).
- [50] N. Warr, UK Data Analysis Manual,*Unpublished*, (2000).
- [51] <http://www.ikp.uni-koeln.de/doc/Tvuser-manual/archive/Tvuser-manual.pdf>. (*This website is no longer accessible. A copy of the manual is in the lab*).
- [52] W. E. Burcham, *Nuclear Physics, An Introduction*, McGraw-Hill, New York-San Francisco (1963).
- [53] E. Sheldon and D. M. Van Patter, Rev. Mod. Phys. **38**, 143 (1966).
- [54] E. Sheldon and V. C. Rogers, Comput. Phys. Commun. **6**, 99 (1973); P. A. Moldaur, Phys. Rev. C **14**, 764 (1976).
- [55] T. Belgya, G. Molnár, and S. W. Yates, Nucl. Phys. **A607**, 43 (1996).
- [56] A. E. Blaugrund, Nucl. Phys. **88**, 501 (1996).

- [57] K. B. Winterbon, Nucl. Phys. **A246**, 239 (1975).
- [58] V. G. Soloviev, *Theory of Complex Nuclei*, Pergomon Press, New York (1975).
- [59] M. Mynk, M.S. Thesis, University of Kentucky (2006).
- [60] <http://www.nndc.bnl.gov/briccc/>, (*Conversion coefficients, α_e*).
- [61] <http://radware.phy.ornl.gov/faq.html>. (*RadWare website*).
- [62] H. Mach, E. K. Warburton, W. Krips, R. L. Gill, and M. Moszynski, Phys. Rev. C **42**, 568 (1990).
- [63] G. Jakob, N. Benczer-Koller, J. Holden, G. Kumbartzki, T. J. Mertzimekis, K.-H. Speidel, C. W. Beausang and R. Krücken, Phys. Lett. **B468**, 13 (1999).
- [64] V. Werner, Ph.D. Inagural-Dissertation, Universität zu Köln (2004).
- [65] C. Fransen, private communication.
- [66] E. Frota-Pessoa and S. Joffily, Nuovo Cim. **96A**, 347 (1986).
- [67] D. Pantelica, I. Gh. Stefan, N. Nica, M.-G. Porquet, G. Duchne, A. Astier, S. Courtin, I. Deloncle, F. Hoellinger, A. Bauchet, N. Buforn, L. Donadille, O. Dorvaux, J. Duprat, B. J. P. Gall, C. Gautherin, T. Kutsarova, S. Lalkovski, R. Lucas, M. Meyer, A. Minkova, A. Prvost, N. Redon, N. Schulz, H. Sergolle, O. Stzowski, Ts. Venkova, and A. Wilson, Phys. Rev. C **72**, 024304 (2005).
- [68] B. Erjun and H. Junde, Nuclear Data Sheets **92**, 147 (2001), (*NNDC data for ^{63}Cu*).
- [69] E. R. Flynn, J. G. Beery, and A. G. Blair, Nucl. Phys. **A218**, 285 (1974).
- [70] W. Andrejtscheff, C. Kohstall, P. von Brentano, C. Fransen, U. Kneissl, N. Pietralla, H. H. Pitz, Phys. Lett. **B506**, 239 (2001).
- [71] A. Holt, T. Engeland, M. Hjorth-Jensen, and E. Osnes, Phys. Rev. C **61**, 064318 (2000).
- [72] I. Talmi, Phys. Rev. **126**, 2116 (1962).
- [73] H. Mach, E. K. Warburton, W. Krips, R. L. Gill, and M. Moszynski, Phys. Rev. C **42**, 568 (1990).
- [74] V. Werner *et al.*, to be published.
- [75] J. B. Ball, R. L. Auble, and P. G. Roos, Phys. Rev. C **4**, 196 (1971).
- [76] P. F. Mantica, A. E. Stuchbery, D. E. Groh, J. I. Prisciandaro, and M. P. Robinson, Phys. Rev. C **63**, 034312 (2001).
- [77] C. Zhang, S. Wang, and J. Gu, Phys. Rev. C **60**, 054316 (1999).
- [78] B. A. Brown, A. Etchegoyen, N. S. Godwin, W. D. M. Rae, W. A. Richter, W. E. Ormand, E. K. Warburton, J. S. Winfield, L. Zhao, and C. H. Zimmerman, MSU-NSCL report number 128

- [79] J. D. Holt, N. Pietralla, J. W. Holt, T. T. S. Kuo, and G. Rainovski, *Phys. Rev. C* **76**, 034325 (2007).
- [80] A. Bohr, B. R. Mottelson, *Nuclear Structure*, vol II, W.A. Benjamin, INC. (1969), pp.44-45.
- [81] S. K. Bogner, T. T. S. Kuo, and A. Schwenk, *Phys. Rep.* **386**, 1 (2003).
A. Bohr and B. R. Mottelson, *Nuclear Structure*, vol II, W.A. Benjamin, INC. pp.44-45 (1969).
- [82] P. van Isacker, K. Heyde, J. Jolie, and A. Sevrin, *Ann. Phys. (N.Y.)* **171**, 253 (1986).
- [83] W. D. Hamilton, A. Irbäck, and J. P. Elliott, *Phys. Rev. Lett.* **53**, 2469 (1984).
- [84] <http://www.nndc.bnl.gov/exfor/endl00.htm>. (ENDF website)
- [85] C. Pugmire, St. M. Mundt, V. P. LaBella and J. Struyf, *GLE Professional Graphics Language User Manual (v. 4.0.12)*, (2006), <http://www.gle-graphics.org>.

VITA

Esmat Elhami

- **Date and place of Birth**

June 2, 1975, Birjand, Iran.

- **Education**

- **Ph. D.** Nuclear Physics, University of Kentucky, Lexington, KY, USA, August 2008(expected)

- * **Dissertation:** Studies of low-lying states in ^{94}Zr excited with the inelastic neutron scattering reaction

- * **Director:** Prof. Steven W. Yates

- **M. S.** Condensed Matter Physics, University of Kentucky, Lexington, KY, USA, December 2005

- **M. A.** Physics, Ball State University, Muncie, IN, USA, July 2002

- **B. Sc.** Applied Physics, Ferdowsi University, Mashhad, Iran, February 1998

- **Professional Positions**

- Teaching Assistant, General Physics, Ball State University, Muncie, IN, August 2000-July 2002

- Teaching Assistant, General Physics, University of Kentucky, Lexington, KY, August 2002-May 2006

- Research Assistant, Nuclear Physics, University of Kentucky, Lexington, KY, May 2006-June 2008

- **Professional Honors**

- Dissertation Year Graduate School Fellowship, University of Kentucky, 2007-2008

- Best woman student presentation, Indiana Academy of Science, 2001, *Technology of electron beam in cancer treatments*

- **Research Experiences**

- Experimental Nuclear Physics
- Experimental Condensed Matter Physics
- Clinical Medical Physics

• **Professional Publications**

- *Anomalous behavior of the 2^+ mixed-symmetry state in ^{94}Zr*
E. Elhami, J. N. Orce, S. Mukhopadhyay, S. N. Choudry, M. Scheck, M. T. McEllistrem, and S. W. Yates, Phys. Rev. C **75**, 011301(R) (2007).
- $2_1^+ \rightarrow 0_1^+$ transition strengths in Sn nuclei
J. N. Orce, S. N. Choudry, B. Crider, **E. Elhami**, S. Mukhopadhyay, M. T. McEllistrem, M. Scheck, and S. W. Yates, Phys. Rev. C **76**, 021302(R) (2007).
- *Determination of the $2_1^+ \rightarrow 0_1^+$ transition strength in ^{58}Ni and physics implications*
J. N. Orce, B. Crider, **E. Elhami**, S. Mukhopadhyay, E. Peters, M. Scheck, M. T. McEllistrem, and S. W. Yates, submitted to Phys. Rev. C (2008).
- *Study of low-lying states in ^{94}Zr with the $(n, n'\gamma)$ reaction*
E. Elhami, S. N. Choudry, S. Mukhopadhyay, J. N. Orce, M. Scheck, M. T. McEllistrem, S. W. Yates, C. Angell, M. Boswell, F. Fallin, C. Howell A. Hutcherson, H. J. Karwowski, J. H. Kelly, Y. Parpottas, A.P. Tonchev, and W. Tornow, to be submitted to Phys. Rev. C (2008).
- *Evidence for Pauli blocking in the $(2^+ \otimes \text{particle})$ multiplets of ^{141}Pr*
M. Scheck, S. N. Choudry, **E. Elhami**, M. T. McEllistrem, S. Mukhopadhyay, J. N. Orce, and S. W. Yates, submitted to Phys. Rev. C (2008).
- *Study of low-lying states in ^{127}I with the $(n, n'\gamma)$ reaction*
S. Mukhopadhyay, M. Scheck, B. Crider, S. N. Choudry, **E. Elhami**, J. N. Orce, M. T. McEllistrem, and S. W. Yates, to be submitted to Phys. Rev. C (2008).
- *Itinerant ferromagnetism to insulating antiferromagnetism: A magnetic and transport study of single crystal $\text{SrRu}_{(1-x)}\text{Mn}_x\text{O}_3$ ($0 \leq x \leq 0.60$)*
G. Cao, S. Chikara, X. N. Lin, **E. Elhami**, V. Durairaj, and P. Schlottmann, Phys. Rev. B **71**, 035104 (2005).

– *Destruction of an orbitally ordered and spin polarized state: Colossal magnetoresistance in $Ca_3Ru_2O_7$*

G. Cao, L. Balicas, X. N. Lin, S. Chikara, **E. Elhami**, V. Durairaj, J. W. Brill, R. C. Rai, and J. E. Crow, *J. of Electronic Materials* **33**, 11 (2004).

– *High temperature weak ferromagnetism on the verge of a metallic state: Impact of dilute Sr doping on $BaIrO_3$*

G. Cao, X. N. Lin, S. Chikara, V. Durairaj, and **E. Elhami**, *Phys. Rev. B* **69**, 174418 (2004).

– *Field tuned collapse of an orbitally ordered and spin polarized state: Colossal magnetoresistance in the bilayered ruthenate $Ca_3Ru_2O_7$*

G. Cao, L. Balicas, X. N. Lin, S. Chikara, **E. Elhami**, V. Durairaj, J. W. Brill, R. C. Rai, and J. E. Crow, *Phys. Rev. B* **69** 014404 (2004).